Dissertation zur Erlangung des Doktorgrades
der Fakultät für Chemie
der Ludwig-Maximilians-Universität München

Antenna-enhanced Optoelectronic Probing of Carbon Nanotube Devices

von

Nina Mauser geb. Rauhut

aus

Fürstenfeldbruck

2014

Erklärung

Diese Dissertation wurde im Sinne von § 7 der Promotionsordnung
vom 28. November 2011 von Herrn Prof. Dr. Achim Hartschuh betreut.

Eidesstattliche Versicherung

Diese Dissertation wurde eigenständig und ohne unerlaubte Hilfe erarbeitet.

München, den 04.09.2014

.....
(Unterschrift des Autors)

Dissertation eingereicht am 04.09.2014
1. Gutachter: Prof. Dr. Achim Hartschuh
2. Gutachter: Prof. Dr. Ralph Krupke
Mündliche Prüfung am 30.10.2014

Abstract

A variety of electronic and optoelectronic devices based on carbon nanotubes (CNTs) has been implemented during the last two decades. For their optoelectronic characterization, diffraction-limited techniques such as photocurrent (PC) and electroluminescence (EL) microscopy were employed. However, for the full characterization of these nano-devices, novel techniques providing nanoscale spatial resolution are desired. This work presents antenna-enhanced optoelectronic probing as a new scanning probe technique for the investigation of nanoelectronic devices. Based on tip-enhanced near-field optical microscopy, sub-diffraction spatial resolution is achieved by employing an optical antenna for the focusing of light. It is applied to study PC and EL signals with a spatial resolution better than 40 nm for the first time. Complemented with antenna-enhanced Raman and topography images, new insights into the optoelectronic properties of CNT based devices are gained.
In the first part of this thesis, an antenna-enhanced photocurrent microscopy study is demonstrated. The signal enhancement mechanism of PC signals is investigated and compared with expectations based on theory. While in spectroscopic applications both the excitation AND the emission rate is enhanced, in optoelectronic applications either the excitation OR the emission rate is affected by the antenna. Theory predicts therefore a weaker total signal enhancement and a lower spatial resolution of optoelectronic signals compared to Raman scattering by a factor of $\sqrt{2}$, which is experimentally confirmed. Then, two applications are presented. First, CNT-metal interfaces are studied and an exponential decay of the band bending at the contacts with a decay length of about 500 nm is revealed. Second, sub-diffraction potential modulations along the CNT channel of another device are probed that remain undetected using confocal microscopy. Combined with high-resolution spectroscopic images of the Raman signal, defects can be excluded as the cause for these modulations. Correlating the PC with the topographic profile reveals charges associated with a particle on the sample substrate as the possible origin.
In the second part, antenna-enhanced electroluminescence microscopy is introduced. The EL emitted by a heterogeneous CNT network is studied with a resolution better than 40 nm. For the first time, pinning of the EL emission to a point-like region of smaller than 20 nm is observed. This strong localization occurs at a junction of at least one metallic and one semiconducting CNT. By probing the PC signal at this junction, the presence of a strong local electric field is revealed, probably caused by a Schottky contact. This allows to identify impact excitation as the most likely origin of the EL emission. A second device, based on a single CNT, was investigated and, in contrast to the network device, the size of the EL source is extended over a length of more than 100 nm.

Contents

1. Introduction

Modern life is strongly affected by a large variety of electronic devices, such as smart phones and laptops. From year to year, these devices become faster, more powerful but at the same time their constituent components shrink in size. This continuous progress can only be achieved with the help of the miniaturization of the most important semiconductor device, the silicon-based metal-oxide-semiconductor field-effect transistor (MOSFET). Scaling down the MOSFET enables an increased number of transistors on a chip as predicted by Moore's law, stating that the number of transistors on a chip doubles every two years. Despite of the difficulties related to the down scaling of the MOSFET, such as high power densities, heat distribution and the device pattern [1], the current generation of MOSFETs employed in the Intel's Core i3 and i5 processors reached nanoscale dimensions (32 nm or 22 nm) [2, 3]. However, a trend for looking for alternative materials replacing silicon in micro- or nanoelectronic applications has developed. A promising candidate for the replacement of silicon is carbon, another group IV element. Although it can be found abundantly on earth it is a very unique and fascinating material: carbon can exist in many modifications with completely different physical properties and dimensionalities caused by the different types of bonds between the carbon atoms. Especially the low-dimensional sp^2-hybridized allotropes, graphene and single-walled carbon nanotubes (SWCNTs), have attracted great interest for nanoelectronic applications during the last two decades. One reason is their inherent tininess: there is no need for scaling them down to nanoscale dimensions. In addition, they exhibit outstanding mechanical and thermal, as well as electronic and optical properties.

SWCNTs feature a broad spectrum of promising applications. Metallic SWCNTs exhibit large current carrying capabilities and could be employed as tiny wires replacing conventional copper wires. Semiconducting SWCNTs are used as a channel in field-effect transistors. The first single carbon nanotube based field-effect transistor (CNTFET) has been realized in 1998 independently by two groups [4, 5]. Fifteen years later, the first carbon nanotube computer entirely using CNTFETs has been realized in 2013 [6], demonstrating the high potential of this material for future electronic applications. In optoelectronics, SWCNTs can function as light detector and light emitter. The first light detector based on the photovoltaic effect was introduced in 2003 [7]. The broad range of bandgaps matching the solar spectrum and a strong absorption from the UV to the IR spectral range, make carbon nanotubes interesting for solar cell applications. Besides single SWCNTs, focus is placed here on thin films, and networks [8]. The first light-emitting device based on single SWCNTs was demonstrated in 2005 [9,10] and the emission wavelength can be tuned over

a broad range by using SWCNTs with different bandgaps. SWCNTs find also application in organic light-emitting diodes (OLEDs) and displays [11–13]. Here, films made of SWCNTs can be used as flexible transparent electrodes replacing the commonly used indium tin oxide (ITO) .

The common tools for the characterization of electronic and optoelectronic carbon nanotube (CNT) devices are electric transport and optical measurements, or a combination of both. However, conventional optical techniques are limited in terms of spatial resolution due to the diffraction of light. Typically, a spatial resolution of about $250 - 500\,\mathrm{nm}$ is achieved depending on the microscope setup and the wavelength used. However, SWCNT based devices are often not longer than few hundreds of nanometers and require therefore characterization techniques with a spatial resolution of few nanometers only. This resolution can in principle be provided by non-optical scanning probe techniques. In fact, a variety of such techniques such as scanning gate microscopy (SGM) and Kelvin probe force microscopy (KPFM) were applied to CNT devices studying e. g. the surface potential along the CNT channel [14–19]. However, they do not allow for the probing of optoelectronic signals. Therefore, the full potential of carbon nanotubes in optoelectronic devices could not be exploited so far. Many questions concerning their optoelectronic properties on the nanoscale, especially in the contact region close to the bulk electrodes, are still open. Investigating and understanding these nanoscale phenomena is needed in order to improve the overall device performance. Therefore, novel techniques must be developed and applied.

In optical microscopy, the diffraction limit has been overcome for more than a decade by various high-resolution approaches, among them tip-enhanced near-field optical microscopy (TENOM). By exploiting locally enhanced electric fields at the apex of a sharp metallic tip in close proximity of the sample material, spatial resolutions as high as 10 nm could be realized [20]. So far, TENOM was only applied in spectroscopic, purely optical applications to a variety of nanomaterials including SWCNTs [21–23], graphene [24, 25], single molecules [26,27], inorganic semiconducting wires [28–30], ferroelectric materials [31] and biological materials such as RNA [32], peptide nanotapes [33] and hemoglobin [34]. In particular, SWCNTs are very suited for TENOM studies due to their photochemical stability and their 1D nature, yielding a strong image contrast both for photoluminescence and Raman scattering [35–39].

In the scope of this work, TENOM was for the first time applied to study optoelectronic signals in SWCNT devices. More specifically, photocurrent and electroluminescence signals could be recorded with sub-diffraction spatial resolution below 40 nm. Combined with tip-enhanced Raman scattering (TERS) measurements, this technique, that is referred to as tip- or antenna-enhanced optoelectronic probing, turned out to be a powerful tool for the non-destructive investigation of nanoscale optoelectronic devices.

The experimental results obtained by applying antenna-enhanced optoelectronic probing to CNT devices in the scope of this work are presented in Chap. 5 and Chap. 6.

In Chap. 5, the first antenna-enhanced photocurrent measurements on CNT devices are presented yielding a spatial resolution of better than 30 nm. First, by comparing antenna-enhanced photocurrent and Raman measurements, the theoretically predicted signal enhancement mechanism could be experimentally confirmed. To demonstrate the powerfulness of antenna-enhanced optoelectronic probing, two applications are presented. First, the extension and shape of the band bending at the CNT-metal interface of a metallic CNT device was studied. It was found that the electric potential decayed exponentially with a decay length of more than 500 nm. For the first time, thanks to the high spatial resolution, the band bending could be imaged separately from the thermoelectric contribution. This confirmed the existence of an energy barrier, that was not expected for a metal-metal contact and can be explained by the low dimensionality of SWCNTs.
Second, for another device, sub-diffraction potential modulations along the channel were probed that could not be observed with confocal SPCM due to spatial averaging of the photocurrent signal. This measurements showed, that the energy bands were not flat on the nanoscale and conclusions on the origin of these modulations could be drawn. Antenna-enhanced spectroscopic images revealed, that the modulations were not caused by structural defects. Instead, the spatial correlation of the modulations and features in the topography profile indicated, that the potential modulations were likely to be caused by particles associated with charges.
In Chap. 6 the first antenna-enhanced electroluminescence measurements are presented with a spatial resolution better than 40 nm, at least one order of magnitude higher than in all other reported electroluminescence measurements. It was thus possible to determine the size of the electroluminescence source, i. e. the length of the emitting CNT segment. For one device, it was found to be point-like, located at a CNT-CNT junction. For a second device, EL emission appeared from a more extended region, with a length of more than 100 nm. By combining antenna-enhanced electroluminescence and photocurrent measurements, the EL emission was found to occur at the position of highest local electric field. This shed light on the mechanism behind the EL emission, identifying impact excitation as the most likely cause.
For one thing, these results complement the state of the art of carbon nanotube based optoelectronic devices by sheding light on photocurrent and electroluminescence phenomena at the contact region or along the channel. For another thing, the high potential of a novel probing technique is pointed out and it is expected, that this technique, applied to other nanoelectronic devices, will deliver valuable, scientific results in the future.

The thesis is structured as follows: at first, Chap. 2 summarizes the basic physics of SWCNTs and the state of the art of carbon based optoelectronics. Chap. 3 focuses on the principle of TENOM and discusses the signal enhancement of purely optical as well as optoelectronic signals. In Chap. 4 an overview of the experimental methods used within the scope of this work is given, including sample fabrication techniques and the description

of the setup for antenna-enhanced optoelectronic probing. In the last three chapters the experimental results are presented and summarized.

2. Theory and state of the art

As discussed in the introduction, carbon is considered to have the potential to replace silicon in the semiconductor industry. It can exist in several modifications of different dimensionalities as illustrated in Fig. 2.1. Four valence electrons are available to form covalent bonds and, depending on the type of bond, different allotropes can form. In three dimensions carbon is the basis for diamond or graphite. In diamond the carbon atoms are bonded to each other by four single sp^3 hybridized bonds in a tetrahedral lattice. In this configuration, the $2s$ orbital mixes with the $2p_x$, $2p_y$ and $2p_z$ orbital forming four equivalent bonds. Graphite consists of many layers of the famous two-dimensional graphene, that are held together by van der Waals forces. Graphene is made of carbon atoms arranged in a hexagonal lattice with three sp^2 hybridized bonds per carbon atom. The $2p_z$ orbitals of the remaining electrons are unaffected by the hybridization and form a delocalized π-electron system perpendicular to the planar lattice. A rolled-up graphene sheet is known as a single-walled carbon nanotube (SWCNT) that is considered as a 1D structure. Finally, in zero dimensions carbon allotropes known as fullerenes exists in a football-like cage structure, among them the famous Buckminsterfullerene consisting of 60 carbon atoms (C_{60}).

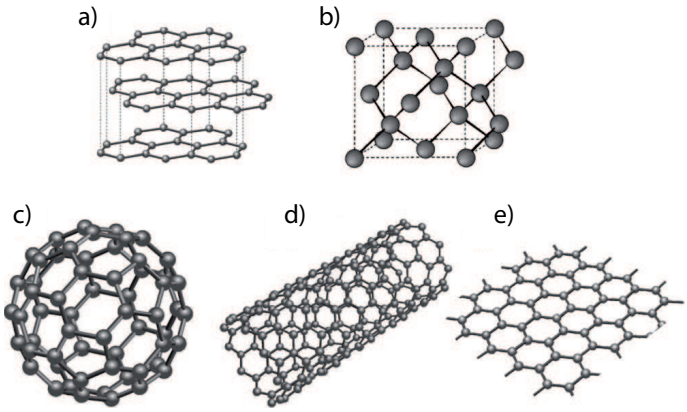

Fig. 2.1. Carbon allotropes in four dimensions (a) **3D** graphite, consisting of many layers of graphene, (b) **3D** diamond in a tetrahedral structure, (c) **0D** fullerene (C_{60}), (d) **1D** single-walled carbon nanotube (e) **2D** graphene. Figure taken from [40].

Especially the one- and two-dimensional forms of carbon, i. e. SWCNTs and graphene, have been subject of great scientific interest for more than 20 years. While theorists worked on graphene for decades, it has been experimentally realized only in 2004 by Novoselov and Geim [41]. For this achievement they were awarded with the Nobel prize in 2005. Carbon nanotubes in multi-wall form have been discovered in 1991 by Iijima [42] and in single-wall form in 1993 [43].

This chapter provides the theoretical basics of single-walled carbon nanotubes and state of the art knowledge on carbon nanotube based optoelectronic devices. The first part sum-

marizes briefly their electronic and optical properties. The lattice and band structure of SWCNTs can be both derived from its parental material graphene. A detailed derivation of the electronic band structure can be found in [44–47]. Related optical phenomena such as photoluminescence and Raman scattering are discussed. The second part gives an overview on the state of the art on carbon based optoelectronics. After briefly summarizing the transport properties of carbon nanotubes, the most important carbon-based nanoelectronic device, the field-effect transistor, and the role of the metal contacts is addressed. Finally, the progress in optoelectronic investigations achieved during the last decade is revised. Emphasis is placed on photocurrent and electroluminescence phenomena in single carbon nanotube devices, and the most important theoretical and experimental published studies is presented.

2.1. Single-walled carbon nanotubes

2.1.1. Structural and electronic properties

A SWCNT is described by a seamless, hollow cylinder obtained by wrapping a single graphene sheet. Different wrapping directions with respect to the graphene lattice vectors lead to SWCNTs with very different electronic properties. The structural and electronic properties of each SWCNT are determined by its *chiral vector* $\mathbf{C}_h = n\mathbf{a}_1 + m\mathbf{a}_2$, defining the circumference of a SWCNT, and is a linear combination of the graphene lattice vectors $\mathbf{a}_1$ and $\mathbf{a}_2$ as illustrated in Fig. 2.2.

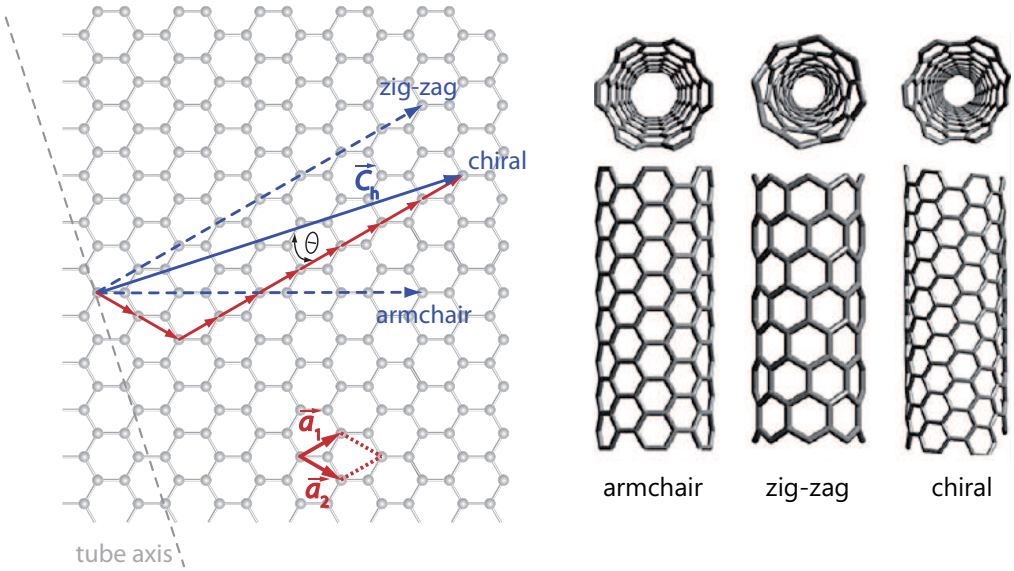

Fig. 2.2. Graphene hexagonal network with lattice vectors $\mathbf{a}_1$ and $\mathbf{a}_2$. The chiral vector $\mathbf{C}_h = n\mathbf{a}_1 + m\mathbf{a}_2$ defines the circumference of the SWCNT obtained by rolling up the two-dimensional graphene sheet. The chiral angle θ is the angle enclosed by $\mathbf{C}_h$ and $\mathbf{a}_1$. The tube axis is defined by the direction perpendicular to $\mathbf{C}_h$. Different chiral vectors lead to different SWCNT structures, that can be classified in armchair, zig-zag or chiral SWCNTs.

n and m are referred to as its *chiral indices*. The angle θ enclosed by the chiral vector and the lattice vector $\mathbf{a}_1$ is called *chiral angle*. A SWCNT can be uniquely defined by its chiral indices (n, m) or its diameter in combination with the chiral angle θ. SWCNTs with indices $n = m$ ($\theta = 30°$) are known as *armchair*, those with $n = 0$ as *zig-zag* ($\theta = 0°$) and the rest as *chiral* tubes (see Fig. 2.2).

To first order, the electronic properties of SWCNTs can be derived from those of graphene [46, 47]. However, quantum confinement due to the 1D nature of SWCNTs must be taken into account. The electronic band structure of graphene calculated by the tight-binding approach is shown in Fig. 2.3 a). At the K-points of the Brillouin zone K and K', the valence and conduction band touch resulting in a zero band gap. Therefore, graphene is referred to as semi-metal. The unique properties of graphene are caused by the linear energy dispersion at the K-points close to the Fermi level E_F described by $E = v_F|\mathbf{k}|$, where v_F is the Fermi velocity and $\mathbf{k}$ is the wavevector of the electron wave function.
In a 1D cylinder the electron wavefunctions are confined around its circumference, leading to quantized values of their wavevector perpendicular to the tube axis $k_\perp = \frac{2\pi n}{|\mathbf{C_h}|}$, where n is a non-zero integer. The component parallel to the tube axis $k_\parallel$ is considered continuous for a SWCNT neglecting its finite length. Therefore, the band structure of a SWCNT does not cover all points of the graphene band structure surface shown in Fig. 2.3 a). Instead, close to the K-points, it consists of slices of allowed wave vectors as illustrated in Fig. 2.3 b) and c). If an allowed k-value crosses the K-point, the SWCNT is classified as metallic and has a linear dispersion relation (Fig. 2.3 b)). All other SWCNTs are semiconducting and exhibit an energy gap E_g between the highest conduction and the lowest valence band (Fig. 2.3 c)). In general, the electronic band structure of a SWCNT consists of a series of one dimensional subbands determined by the cutting-lines through the surface of the graphene band structure. The position of the cutting lines is determined by the chiral indices. More specifically, SWCNTs with $\mathrm{mod}(n - m, 3) = 0$ are metallic, those with $\mathrm{mod}(n - m, 3) \neq 0$ are semiconducting [46, 47].
The approximation described is known as *zone folding*. It can give reliable results for SWCNTs with a large enough diameter ($\geq 1.5\,\mathrm{nm}$), since it ignores the curvature of the SWCNT wall. Taking the curvature into account, only armchair (n=m) SWCNTs are truly metallic. Otherwise metallic SWCNTs with $\mathrm{mod}(n - m, 3) = 0$ exhibit a small bandgap of tens of meV caused by the curvature of the wall.
The one-dimensional subbands of the band structure give rise to sharp peaks, so called van Hove singularities (vHS) in the density of states (DOS) as shown in Fig. 2.3 d). The peaks are located at the lower edge of the electronic subbands. The DOS at the Fermi level is finite for metallic (armchair) and zero for semiconducting SWCNTs. The DOS predominantly determines the optical transitions that occur in SWCNTs. Transitions that connect two vHSs are more likely due to the large DOS of the initial and final state.

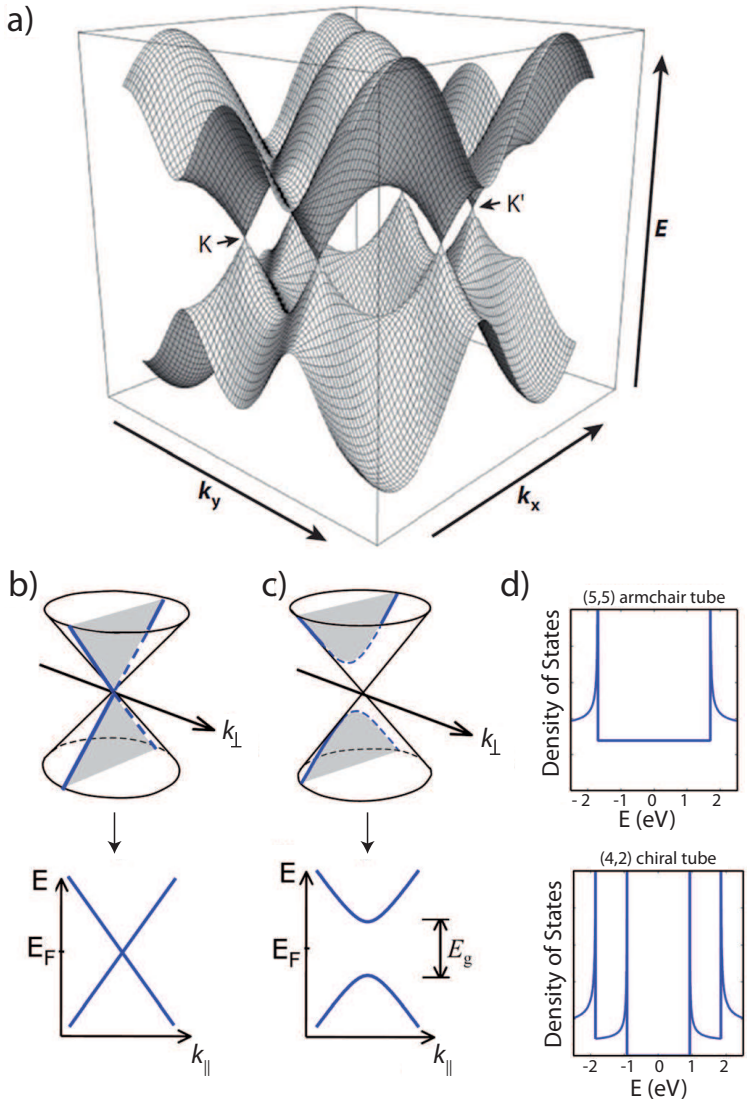

Fig. 2.3. a) Electronic dispersion relation of graphene. The conduction and valence band touch at the K-points K and K' leading to a zero band gap. b) The cone-shaped linear dispersion near the K-point with a slice through the band representing allowed wave vectors $k_\perp$ that pass through the K-point. This gives the linear band structure of a metallic SWCNT. c) Slice of allowed $k_\perp$ not passing through the K-point. This gives the parabolic bands of a semiconducting SWCNT with a band gap in between them. d) Density of states (DOS) for an armchair, metallic SWCNT with a finite DOS at the Fermi energy. For a semiconducting SWCNT the DOS around the Fermi energy is zero. Figure taken from [48].

2.1.2. Optical properties

The optical processes that can occur in SWCNTs are summarized in Fig. 2.4. Photoluminescence can be observed only for semiconducting SWCNTs, whereas Rayleigh and Raman scattering occur in both semiconducting and metallic SWCNTs. Due to the strong Coulomb interaction in one-dimensional materials, an excitonic picture has been established to describe SWCNT photoluminescence (see Fig. 2.4 a)) [49, 50]. The reduced average distance between the charge carriers and the reduced dielectric screening caused by the

one-dimensionality of a SWCNT leads to strongly bound electron-hole pairs even at room temperature. Although an excitonic picture is also appropriate for the description of Raman scattering, excitonic effects are usually neglected when calculating Raman scattering intensities [45]. Instead, a free carrier model is used as illustrated in Fig. 2.4 b).

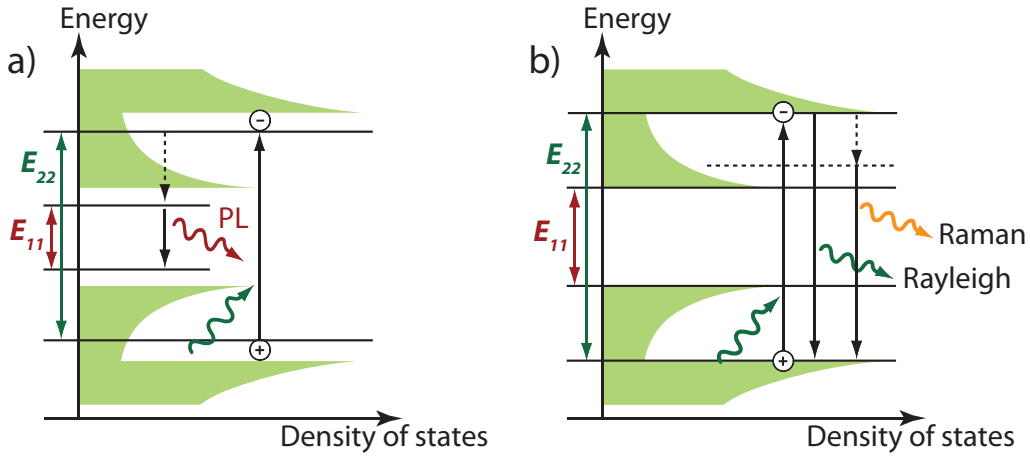

Fig. 2.4. Optical processes in SWCNTs. a) Photoluminescence. The excitonic states are shifted down in energy with respect to the free carrier states. A photon with an energy equal to the transition E_{22} is absorbed, creating a strongly bound electron-hole pair (exciton). After fast relaxation to the first excitonic state, photoluminescence with an energy corresponding to the E_{11} transition is emitted. b) Raman scattering. The free carrier states are determined by the vHSs in the DOS. An photon absorbed by the E_{22} transition can be scattered elastically (Rayleigh scattering) or inelastically (Raman scattering).

Photoluminescence

In the currently accepted picture of SWCNT photoluminescence, electron-hole pairs are combined into an exciton upon photoexcitation. The excitons in SWCNTs are strongly bound due to the 1D nature of SWCNTs with a binding energy of few hundreds of meVs, much larger than the thermal energy at room temperature. As indicated in Fig. 2.4 a), these strongly bound states are shifted with respect to the free carrier states that are given by the singularities in the density of states. This shift comes from both repulsive electron-electron interactions and attractive electron-hole interactions. Both contributions compensate each other to a large extent such that the excitonic states are close to the free carrier states. The optical transitions, dominated by the excitonic states, are denoted as E_{ii}, where i denotes the corresponding subband. Since the energy of the E_{11} exciton is typically below 1 eV, light is absorbed by a transition with $i > 1$ (e.g. the E_{22} transition as shown in Fig. 2.4 a)), whereas emission occurs from the E_{11} transition after some fast (tens of femtoseconds [51]) relaxation process. The photoluminescence spectrum of a SWCNT can be used for chirality assignment, since the emission energy is uniquely defined by the nanotube chiral indices [52]. Optical transitions occur mainly between bands of same indices such as E_{11} and E_{22}. They are allowed for light polarized along the nanotube axis. Transverse transitions (E_{ij} with $j = i + 1$) involving polarization perpendicular to the

tube axis are strongly suppressed by a depolarization effect, i. e. the incident excitation field is screened by charges on the SWCNT wall [53]. As a consequence, emitted SWCNT photoluminescence is almost completely polarized in the direction of the tube axis.

Raman scattering

Raman scattering is inelastic scattering of light by a phonon, i. e. the incident and scattered photon are different in energy and this energy difference is carried by the involved phonon. Usually the energy of the emitted photon is smaller than the one of the incident photon, and the scatterer is left in a vibrationally excited state, i. e. a phonon is emitted. This process is known as Stokes scattering. The absorption of a phonon is called anti-Stokes scattering. In a Raman process, both energy and momentum are conserved

$$\hbar\omega_1 = \hbar\omega_2 \pm \hbar\omega_{ph}. \tag{2.1}$$

$$\mathbf{k_1} = \mathbf{k_2} \pm \mathbf{q} \tag{2.2}$$

where ω_1 ($\mathbf{k_1}$) is the frequency (momentum) of the absorbed, ω_2 ($\mathbf{k_2}$) of the emitted photon, and ω_{ph} ($\mathbf{q}$) of the phonon. The $\pm$ indicates Stokes and anti-Stokes scattering. As for photoluminescence, Raman scattering is strongest for light polarization parallel to the tube axis due to a vanishing polarizability in perpendicular direction caused by efficient screening of the excitation field [54].

By measuring the frequency of the emitted photon, one can determine the phonon frequencies of a SWCNT. These are determined by its phonon dispersion relations. Similar to the electronic band dispersion, the phonon dispersion relations of a SWCNT can be theoretically derived from graphene by the zone folding approach [47]. Since graphene has 2 atoms in a unit cell, it exhibits 6 phonon branches (3 acoustic, 3 optical). For a SWCNT with $2N$ atoms in a unit cell there are $6N$ phonon dispersion relations (e.g. $6N = 120$ for a $(10, 10)$ nanotube), 4 of them belonging to acoustic phonons. However, many of the optical phonon dispersion relations are degenerated and only few modes are Raman active, depending on their symmetry.

Due to inherently small Raman scattering cross sections, only resonance Raman spectra of single SWCNTs can be observed experimentally. In resonance Raman scattering (RRS) the energy of the absorbed or emitted photon coincides with a real transition, i. e. it connects two van Hove singularities as indicated in Fig. 2.4 b). The signal intensity is then increased by orders of magnitude compared to the non-resonant case. The resonance can occur with the incoming or the scattered photon or both. The observed Raman modes can be classified according to their order, that is the number of scattering events. Fig. 2.5 summarizes first and second order Raman processes of a metallic SWCNT for resonance with the absorbed or scattered photon.

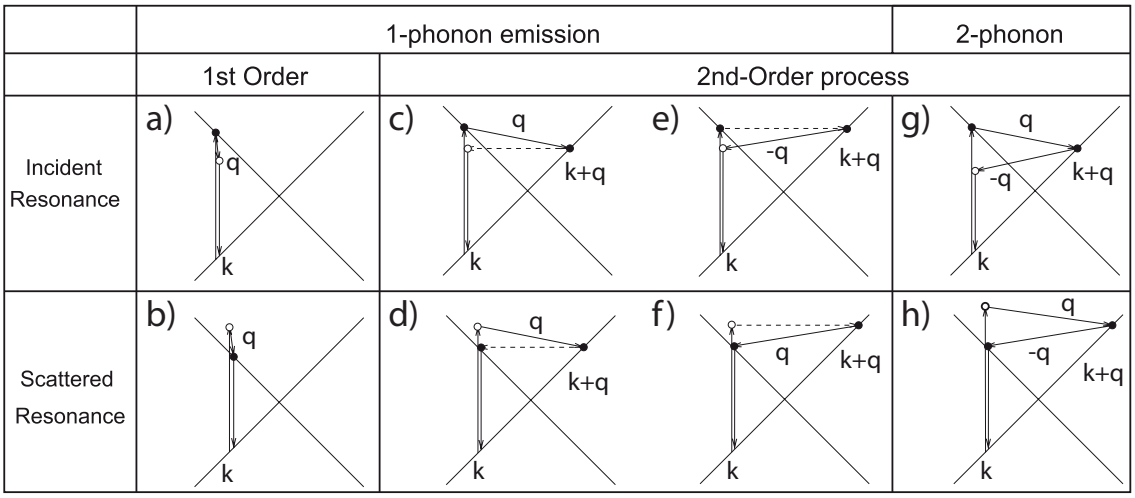

Fig. 2.5. a) and b) First order Raman processes, c) - h) second order Raman processes of SWCNTs for resonance with the incident photon (upper row) and scattered photon (lower row). In a first order process an electron is scattered by one phonon with momentum $\mathbf{q} \approx 0$ to conserve momentum. In a second order process, either c)-f) one phonon and an elastic scattering event, or g) and h) two phonons are involved. $\mathbf{k}$ denotes the electron, and $\mathbf{q}$ the phonon momentum. Elastic scattering is depicted with a dashed line, resonance points with solid circles. Figure taken from [45].

In a first order process, only one phonon is involved. Due to momentum conservation (Eqn. 2.2), only phonons with $\mathbf{q} \approx 0$ are observed, corresponding to perpendicular transitions in the band dispersion (see Fig. 2.5 a) and b)). The most prominent first order peaks are the high-energy *G band* appearing at about $1580\,\mathrm{cm}^{-1}$ and the low-energy *radial-breathing mode (RBM)* at about 70-$350\,\mathrm{cm}^{-1}$.

G band The G band is common to all sp^2-carbons and is related to the in-plane C=C stretching mode. Whereas it is a single, Lorentzian peak for graphite, it splits into two main features for SWCNTs due to the curvature of the SWCNT wall. One component peaks around $1590\,\mathrm{cm}^{-1}$, the other around $1570\,\mathrm{cm}^{-1}$. For semiconducting SWCNTs, the higher frequency component is related to vibrations along the tube axis (longitudinal optical, LO, phonon mode, denoted with G^+). The lower frequency component (G^-) is associated with carbon atom vibrations along the circumferential direction (transverse optical, TO, phonon mode) and therefore, in contrast to the G^+ component, depends on the SWCNT diameter. The assignment is opposite for metallic SWCNTs, in case of which the LO phonon mode is downshifted up to $100\,\mathrm{cm}^{-1}$ to lower frequencies. This mode softening can be explained by an increased electron-phonon coupling for the LO mode in metallic SWCNTs [47]. In addition, the line shape of the softened peak can be very different compared to semiconducting SWCNTs. Whereas both G^+ and G^- have a Lorentzian shape for semiconducting SWCNTs, the softened component can have a non-Lorentzian, broadened shape for metallic SWCNTs in case of resonant excitation. The spectra of metallic SWCNTs can therefore appear both metallic- and semiconducting-like,

depending on the excitation wavelength. A metallic-like spectrum can be used to identify the respective SWCNT as metallic, whereas a semiconducting-like spectrum cannot be used for a reliable assignment.

Radial breathing mode

The radial breathing mode is a mode unique for SWCNTs that does not appear in any other nanocarbon. It is a breathing like motion of all carbon atoms, that move in phase in radial direction. It can be used for determining the diameter of a SWCNT, since the RBM frequency is directly related to the tube diameter and follows the relation [55]

$$\omega_{RBM} = \frac{227.0}{d}\sqrt{1 + C \cdot d^2}, \tag{2.3}$$

where d is the nanotube diameter and C is a parameter that accounts for interaction with the environment. Due to its small energy, the RBM appears only in resonance condition with a narrow resonance window (width of few meV). It can therefore be used to determine the transition energies E_{ii} of a specific SWCNT using a *Kataura plot*. A Kataura plot is routinely used for the interpretation of Raman spectra of carbon based materials. It maps the calculated E_{ii} of SWCNTs of different chiralities as a function of d, ω_{RBM}, respectively. An example is presented in Fig. 2.6 a). Groups of SWCNTs are formed according to their transition energies denoted by E_{ii}^M for metallic, and E_{ii}^S for semiconducting SWCNTs. Assuming that $E_{ii} \approx E_{ex}$, where E_{ex} is the excitation energy, one can thus deduce the transition energies E_{ii} of a SWCNT for a given RBM frequency ω_{RBM}.

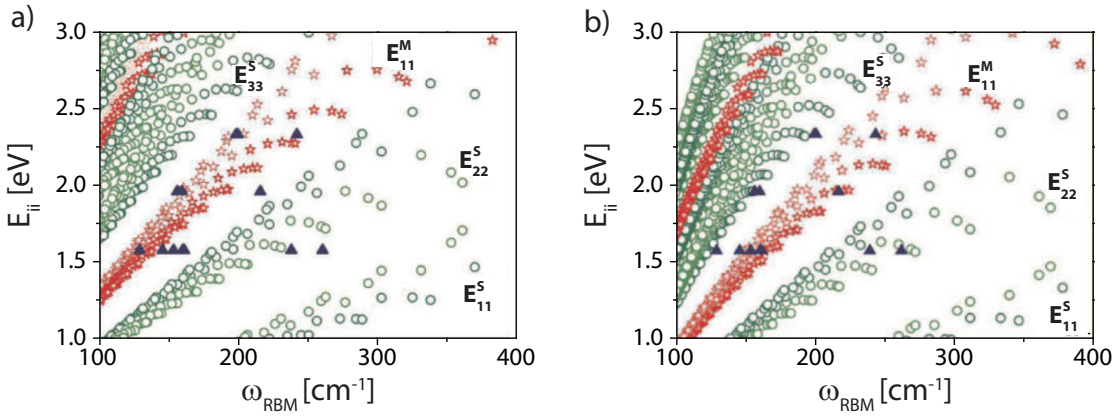

Fig. 2.6. Kataura plots of two different SWCNT samples. A Kataura plot is obtained by plotting the optical transition energies (E_{ii}) of each (n, m) SWCNT against the respective RBM frequencies. a) Kataura plot for pristine SWCNTs showing no environmental interactions. b) Kataura plot for SWCNTs on crystalline quartz. Circles denote semiconducting SWCNTs, stars metallic, respectively. Up triangles represent experimentally obtained values. Figure adapted from [56].

The transition energies are influenced by environmental effects, such as bundling, surfactants or coupling to the substrate [55, 56]. Fig. 2.6 demonstrates the shift of the transition energies caused by a different environmental surrounding: Fig. 2.6 a) shows the Kataura

plot of the so-called *supergrowth SWCNTs*, grown vertically on silicon by water-assisted chemical vapor deposition. This growth method yields long, isolated high-purity SWCNTs [55]. They show the fundamental relation $\omega_{RBM} = 227.0/d$ with negligible environmental effects ($C = 0$ in Eqn. 2.3). Fig. 2.6 b) shows slightly shifted transition energies for CVD grown SWCNTs on a crystalline quartz substrate. The different transition energies are caused by the coupling to the quartz substrate that leads to a value for $C = 0.082\,\mathrm{nm}^{-2}$ [56].

In higher order scattering processes, the phonon vector $\mathbf{q}$ is not restricted to zero as in a first-order process. A second order process can either involve a two phonon process, or a one-phonon process combined with an elastic scattering event as illustrated in Fig. 2.5 c) to h)). The most prominent mode for the latter case is the *D band* scattering. Here, the elastic scattering is mediated by a defect in the lattice structure such as amorphous carbon, missing atoms, the finite length of the SWCNT or any other irregularity. The overtone of the D band, the so-called *G′ band*, appearing at a frequency of twice the D band frequency is an example for a two phonon process.

D band

The D band occurs at about $1350\,\mathrm{cm}^{-1}$ and is dispersive ($\approx 50\,\mathrm{cm}^{-1}/\mathrm{eV}$). In D band scattering, an electron at a $\mathbf{k}$-state absorbs a photon, scatters to $\mathbf{k}+\mathbf{q}$ by emitting a phonon with momentum $\mathbf{q}$, scatters elastically back to $\mathbf{k}$ by a defect and emits a photon by recombining with a hole at $\mathbf{k}$ (see Fig. 2.5 c)-f)). The dispersive behavior can be explained by a double-resonance scattering model in which both the initial or final $\mathbf{k}$-state and the intermediate $\mathbf{k}+\mathbf{q}$-state are real electronic states. With increasing laser energy the resonant $\mathbf{k}$-state moves away from the K-point, leading to an increased $\mathbf{q}$-vector that fulfills the resonance condition. Therefore, for each excitation energy a different phonon vector is selected leading to a dispersive behavior.

G′ band

The G′ band is caused by scattering by two phonons with the same energy but opposite momentum $\mathbf{q}$ and $-\mathbf{q}$ (see Fig. 2.5 g) and h)). It is thus the overtone of the D band appearing at about $2700\,\mathrm{cm}^{-1}$ with a dispersion of about $100\,\mathrm{cm}^{-1}/\mathrm{eV}$.

Besides the described four Raman bands there are several other low-intensity Raman modes in SWCNTs, such as the intermediate frequency modes (IFM), the M band or other overtone and combination modes [45].

2.2. Carbon nanotube based optoelectronics

Due to their excellent optical and transport properties, carbon nanotubes have a great potential for optoelectronic applications. A variety of electronic and optoelectronic devices based on single SWCNTs has been realized during the last decade. But not only single SWCNTs, but also other carbon materials, such as graphene, multi-walled CNTs and CNT bundles, networks or arrays have been investigated as key component of nanoelectronic devices. This section provides an overview on the development and state of the art of carbon based optoelectronics as outlined in many reviews [1, 40, 48, 57–62].

Transport properties

Transport in SWCNTs can be ballistic or diffusive, depending on the bias voltage and the length of an electrically contacted SWCNT. Ballistic transport in metallic SWCNTs is possible due to the absence of elastic or inelastic scattering. Compared to bulk material, elastic scattering of an electron caused by defects or other electrons is strongly reduced in SWCNTs leading to very long elastic mean free paths for metallic SWCNTs on the order of micrometers. This can be explained by their one-dimensionality: first, in 1D materials, only back- or forwardscattering can occur in contrast to 3D materials, where scattering in all directions is possible. Second, backscattering in metallic SWCNTs is forbidden due to the symmetry of the band structure [47, 63]. Third, the electronic states are smeared out around the nanotube's circumference, reducing the influence of a defect [47, 64]. Therefore, for channel lengths smaller than the mean free path and low bias voltages, transport in metallic SWCNTs is ballistic. Assuming perfect, ohmic contacts the conductance in metallic SWCNTs is predicted to be $2G_0 = 4e^2/h$, with G_0 being the quantum of conductance, because two conducting channels with each two electrons with opposite spin contribute to the current close to the Fermi level. Although this value has been confirmed experimentally by several groups, a much lower conductance usually is measured due to imperfect CNT-metal contacts (see Sec. 2.2).
In semiconducting SWCNTs, backscattering is present, reducing the mean free path as compared to metallic SWCNTs by about one order of magnitude [65]. In very short semiconducting SWCNTs, the ballistic regime can be reached, but usually the transport in semiconducting CNTs is described by a diffusive model.
For larger bias voltages, the transport in both metallic and semiconducting SWCNTs is dominated by inelastic scattering. Depending on the bias, the carriers can interact either with low-energy acoustic phonons or high-energy optical phonons of the lattice. In case of interaction with acoustic phonons only, the resistivity increases linearly with temperature due to backscattering by thermally populated acoustic phonons [57]. At high bias voltages, the electrons are accelerated to energies large enough (typically around 200 meV) to be scattered by optical phonons. This leads to a reduced mean free path of about 10-20 nm. The emission of optical phonons leads to a saturation current of about 25 µA in metallic

SWCNTs on substrates [66]. In suspended SWCNTs without any substrate cooling, the current even decreases with increasing bias voltage indicating a substantial heating of the SWCNT.

Electronic devices and the role of the metal contacts

Due to their unique transport properties, metallic SWCNTs, especially multi-walled CNTs, are suggested to be employed as tiny wires or high-performance interconnects [67]. According to bulk semiconductors, semiconducting SWCNTs can be used as p-n junction diodes [68, 69] or as channel of field-effect transistors (FET), where the transport in the channel can be switched on and off by means of an electric field. The first carbon nanotube based field-effect transistors (CNTFET) were independently fabricated by Tans et *al.* [4] and Martel et *al.* [5] in 1998. The basic structure is similar to conventional silicon based FETs (MOSFETs) and depicted in Fig. 2.7: a semiconducting channel (SWCNT or silicon) is contacted by two electrodes (source and drain). A third electrode called the gate is separated from the channel by a thin insulating layer (e.g. SiO_2). By changing the voltage between the gate and the source electrode, the current through the semiconducting channel can be modulated by orders of magnitude.

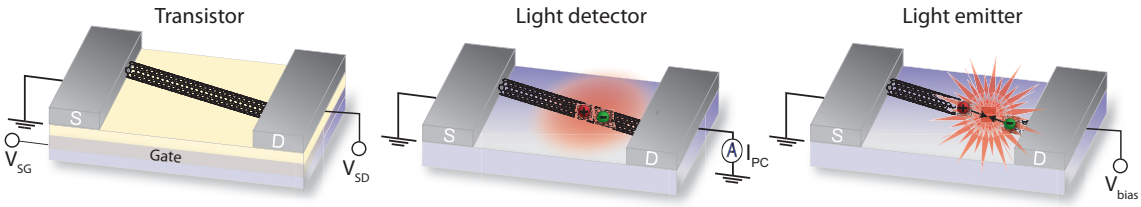

Fig. 2.7. Carbon nanotube based devices. Depending on the source-drain (V_{SD}) and gate voltage (V_{GS}) a CNT device can operate as transistor, light detector or light emitter. While the transistor is a purely electronic device, the light detector and light emitter are optoelectronic devices acting as optical-to-electrical, electrical-to-optical transducers, respectively [59, 60].

Although the basic structure is the same, there are several superior features of a CNTFET compared to a MOSFET. First, the outstanding electrical properties of the CNT channel, i. e. the low scattering and the high carrier mobility. Second, the small diameter of the CNT allows optimum coupling between the channel and the gate. Third, the smooth surface of the SWCNT that reduces surface scattering [60].
At first glance, the basic principle of a MOSFET and a CNTFET seems to be the same. However, there is a large difference in the performance of a CNTFET and a conventional MOSFET: In a MOSFET, by changing the gate voltage, the charge density in the channel and therefore the current is modulated. The source, drain and gate electrodes are made of highly-doped silicon leading to ohmic contacts and therefore play a minor role for the device operation. This is very different for CNTFETs, whose performance is strongly influenced by the metal contacts. The electrodes are usually made of metals such as

titanium, gold, palladium or aluminum that have a similar work function as a SWCNT. The difference in work function of the metal and the SWCNT leads to charge transfer between the two materials when getting in contact. As a consequence, electric fields build up at the contacts, leading to the formation of a Schottky barrier as in bulk metal-semiconductor interfaces. Whereas the first CNTFETs [4, 5] were believed to operate in a similar way as MOSFETs, the importance of the Schottky barrier formation at the contacts for the device operation was soon investigated by several studies [70–74]. Nowadays, it is generally accepted, that the device operation is based on changing the width and height of the contact barrier leading to reduced or increased carrier injection through the barrier. As a consequence, CNTFETs are ambipolar, i. e. both electrons and holes can be injected into the channel. Depending on the gate and source-drain voltage, a CNTFET can be operated in the ambipolar region, or in the p (n)-region, where only holes (electrons) are transported. A conventional MOSFET is an unipolar device, transporting only one type of carrier.

However, the device operation is not determined by the Schottky barrier only. Besides the Schottky barrier, a contact barrier, created by an imperfect interface between the SWCNT and the metal, may form in series. This can lead to large contact resistances, exceeding the resistance of the SWCNT itself and therefore limiting the current. The contact resistance depends on the material properties of the metal, such as the work function and the wettability [75–77], but also on the fabrication methods and conditions. The carriers are injected into the SWCNT channel either by thermal activation over or by tunneling through the barrier. Therefore, both the Schottky barrier height and width are of importance for the conductive behavior. The width of the Schottky barrier can be influenced by the thickness of the gate oxide. A stronger coupling to the gate results in more efficient screening. The height of the energy barrier depends on the difference in the work functions of the SWCNT and the metal, the diameter of the SWCNT and the adhesion between the metal and the SWCNT [60]. Palladium is reported to give reliable ohmic contacts to metallic SWCNTs, whereas titanium and platinum give non-ohmic contacts despite excellent wetting of the SWCNT sidewalls by titanium [75–77]. Palladium was also found out to be the best material for semiconducting SWCNTs. It has the highest work function compared to the other metals and therefore forms the lowest Schottky barrier to the valence band of the SWCNT [78]. Chen et *al.* investigated more than 100 CNTFETs consisting of electrodes made of three different metals titanium, palladium, aluminum with the goal of finding out the CNT-metal combination for best CNTFET performance. Since the Schottky barrier does not only depend on the work function and the wetting properties of the metal, but also on the band gap of the SWCNT, they used SWCNTs of different diameters. According to their findings, the best p-CNFET on-state performance can be achieved by combining SWCNTs with diameters above 1.4 nm with palladium contacts [78]. Low work function materials such as aluminum yield better n-type contacts since the Schottky barrier is low for electrons in the conduction band. However, in general, it is difficult to predict the Schottky barrier height and width for

a given CNT-metal contact. First, the conduction behavior can be influenced by the environmental conditions. For example, in ambient conditions, oxygen doping of the metal or the SWCNT itself leads to p-type conduction behavior in contrast to n-type behavior under vacuum [73, 79]. Furthermore, metal-induced gap states (MIGS) with energies in between the band gap of the SWCNT may exist and lead to Fermi level pinning. As a result, the dependence of the Schottky barrier height on the work function of the metal disappears [48].

Optoelectronic devices

Besides purely electrical devices, such as the CNTFET, SWCNTs are employed in optoelectronic devices that can either detect or emit light as illustrated in Fig. 2.7. In principle, the same device can operate as a transistor, a light detector or a light emitter, depending on the applied gate, source and drain voltages. There are many reviews summarizing the potential of SWCNTs for optoelectronic applications such as photovoltaic devices and electrically induced light emitters [1, 40, 59–62].

Light detectors

As any other semiconductor, carbon nanotubes can be used as optical-to-electrical transducers. The first light detector was realized by Freitag et *al.* [7]. They demonstrated a photocurrent upon optical excitation of a single SWCNT in a FET configuration under an applied source-drain voltage. The photocurrent showed a resonance for an excitation energy that matches the E_{22} excitonic state of the SWCNT and was maximum for a polarization along the tube axis. With their experiment they showed that the photocurrent comes from the decay of optically created excitons into an electron-hole pair that can be separated by the applied bias voltage - the principle of many photovoltaic devices.

This experiment was followed by numerous optoelectronic studies on SWCNT based devices. A popular tool used for these investigations is scanning photocurrent microscopy (SPCM). In SPCM a focused laser beam is raster scanned across the device and the photocurrent is recorded as a function of laser position. This technique was for the first time applied to SWCNT optoelectronic devices by Balasubramanian et *al.* in order to image the Schottky barrier formation at a CNT-metal interface [80]. The same group observed also an energy barrier formation for metallic SWCNTs by recording photocurrent maps at zero bias voltage [81]. In zero-bias imaging the local built-in electric fields at the contacts or along the SWCNT are directly mapped without the need of applying an external field for charge separation. Therefore, the position and intensity of the photocurrent signal provides information on the local electric potential. The principle of photocurrent signal generation for a device at zero bias is presented in Fig. 2.8. As can be seen from the schematic, illuminating the contact regions at the source or drain voltage generates photocurrent signals of opposite sign.

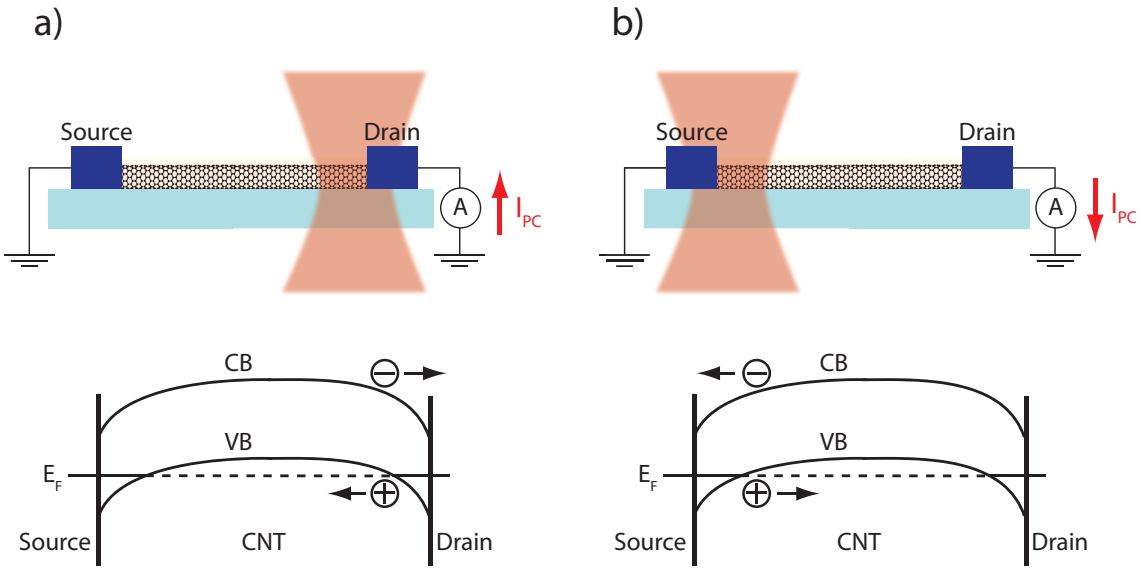

Fig. 2.8. Principle of photocurrent generation for a semiconducting SWCNT at zero bias. Light absorption leads to the creation of electron-hole pairs that are separated by the local electric field at the contacts. a) Illumination of the source and b) illumination of the drain electrode leads to a different sign of the generated photocurrent as can be understodd considering the energy band diagram. VB (CB) denotes the valence (conduction) band and $E_F$the Fermi energy. In the region of band bending, the optically excited electron-hole pair is separated by the local electric field leading to a photocurrent signal that has a different sign for each contact.

They observed photocurrent signals at the contacts and along metallic SWCNTs. The signal along the channel was attributed to an energy barrier formation due to structural defects. More specifically, the defect was assumed to be a semiconducting segment leading to a barrier formation at each segment end. The existence of the contact barrier was explained by a charge transfer caused by the difference in work functions.
However, the barrier observed at a metal-metal contact was rather surprising. Metal-metal contacts are known to be of ohmic nature with a barrier width of zero due to screening of the electric field by the free electrons. In fact, energy barriers between metallic SWCNTs and a copper wire were predicted theoretically by Kong et *al.* [82] and experimental indications for such a barrier were found by low temperature measurements [83]. In both studies, the authors explained the energy barrier formation by a difference between a 3D-3D and a 3D-1D contact. In [82], the authors argument that the π-bonding state of the conduction electrons in a SWCNT is different from the free-electron state in a 3D metal. In [83], the barrier formation is assumed to come from a less efficient electrical screening in 1D materials compared to 3D materials.

The photovoltaic effect, i. e. charge separation upon optically excitation, was exploited in single carbon nanotube photodiodes [69,84–86]. A p-n junction in a single SWCNT can be fabricated by using two gate electrodes and corresponding gate voltages of opposite signs. This leads to the formation of an electric field at the junction that can be used for charge carrier separation. Freitag et *al.* also observed photovoltage signals along the channel that

they attribute to local electric fields caused by structural defects as in [81]. Furthermore, they could correlate the photovoltage signals with maxima in the defect-induced band obtained by Raman measurements, showing that both techniques are sensitive to the same defects [87].
They also exploited the direct proportionality between the photocurrent and the magnitude of the electric field, i. e. the band energy gradient, a common procedure in SPCM experiments. The band energy profile can then be obtained by spatial integration over the photocurrent along the SWCNT, illustrating that photocurrents are associated with modulations in the band energy profile. The same group demonstrated how SPCM can be used to image the depletion region at the contacts [88]. They showed that the depletion width can be as large as 1.5 µm for electrons. A lower limit of 400 nm for holes was determined by the optical resolution of the system. They also considered two other effects, besides the photovoltaic effect, that contribute to the photocurrent signal at the contacts caused by absorption of photons by the electrode metal: internal photoemission of optically excited electrons and thermally assisted tunneling through the barrier caused by laser heating. Besides the determination of the depletion width, SPCM can also be used to access the Schottky barrier height as demonstrated in [89]. The authors determined a Schottky barrier height of about 180 meV of a semiconducting SWCNT contacted to AuPd electrodes.
SPCM can be used to investigate any local electric field at the contacts or caused by defects. Ahn et *al.* demonstrated the existence of an internal p-n junction, another source for a local electric field, in a CNTFET by means of SPCM [90]. Local electric fields also exist at CNT-CNT crossjunctions and lead to photocurrent signals as investigated in [91]. SPCM has also successfully been applied to other materials than SWCNTs, such as silicon or cadmium sulfide nanowires [92, 93]. It was also used to investigate nanotube networks and graphene [94] and SWCNT arrays [95, 96].

As in purely optical measurements, either the excitonic or the interband transitions could be involved in photocurrent experiments. Photocurrent spectroscopy experiments, which map the photocurrent as a function of wavelength, reveal resonances that cannot be explained with an interband interpretation. Besides the observed main excitonic resonances, side bands, corresponding to the simultaneous excitation of an exciton and a phonon appear [9, 97].
However, excitons can only contribute to the photocurrent, if they are dissociated into unbound electron-hole pairs. Their high binding energy of few hundred of meV (see Sec. 2.1.2) requires high electric fields on the order of 100 V/µm [98], that exceed the bias fields of standard photoconductivity measurements. Kato et *al.* presented a dissociation mechanism supported by simultaneous photoluminescence and photocurrent measurements on single suspended SWCNTs [99]. They excluded field-induced dissociation and suggested phonon-assisted, spontaneous dissociation of E_{22} excitons into a free electron-hole pair. At

high excitation powers, Auger recombination leading to free carriers could play a role [100].

In all the mentioned studies, the photocurrent signal has mainly been attributed to the classical photovoltaic effect, i. e. the charge carrier separation due to an intrinsic or external electric field. First indications for the existence of other, non-photovoltaic, processes for the photocurrent generation were already given in [88]. Studies on suspended SWCNT films [101] and suspended single SWCNTs [86,102] reveal the existence of a thermoelectric effect that contributes to non-negligible degree to the photocurrent signal and can even overshadow it. The photothermal contribution is expected to increase in suspended devices compared to devices on a substrate due to a less efficient cooling. There are also several studies on non-suspended graphene p-n junctions that identify the thermoelectric effect as main cause for the observed photocurrents [103–106]. However, Freitag et *al.* assigned the photocurrents in homogeneous biased graphene to the photovoltaic effect, and show that the thermoelectric effect is one order of magnitude lower [107]. They also discuss a bolometric effect, where the resistance of the device is changed upon local laser heating of the device. This effect, however, plays a role in devices under dc bias. These studies clearly show, that the photocurrent generation in a certain device cannot be attributed solely to one mechanism. Depending on the device configuration, the photovoltaic, thermoelectric or bolometric effects can contribute to a varying degree.

Light emitters

Besides a light detector a CNTFET can also act as a light emitter. By applying a suitable gate and source-drain voltage to the SWCNT channel, electrically induced light emission can be observed. The first light emitter based on a single SWCNT was realized in 2003 by Misewich et *al* [108]. By operating a CNTFET in the ambipolar regime, holes and electrons could be simultaneously injected into the SWCNT creating a p-n junction. Both charge carrier types then combined radiatively leading to the observed polarized emission in the IR that reflects the E_{11} transition. By using SWCNTs of different diameters the wavelength of the light emission can be tuned. This study was followed by a spectral investigation of the electroluminescence emitted by SWCNT devices with different channel lengths [109]. The authors observed that long-channel devices show narrow peaks (half width $\approx 25\,\mathrm{meV}$), whereas short-channel devices show broad peaks (half width $\approx 150\,\mathrm{meV}$). The authors explained the different spectral widths by hot-carrier relaxation in short SWCNTs and thermalized carrier relaxation in long SWCNTs. The same group demonstrated spatially resolved electroluminescence measurements showing a moving electroluminescence spot along the channel by changing the gate and source-drain voltage [110]. With this method they could image the position of the ambipolar segment, where electrons and holes meet and determine the recombination length, i. e. the size of

the light source, to be about few microns, depending on the applied bias.

Similar to photocurrent signals, several mechanisms causing electroluminescence emission may exist in a given device. One is the recombination of electrons and holes due to ambipolar transport as described above. This mechanism is the basis of light-emitting devices (LEDs) using SWCNTs [111, 112]. In [110], besides the mobile electroluminescence spot, the authors also observed, stationary, non-moving spots, that they explained by impact excitation instead of ambipolar recombination. For impact excitation, electrons are accelerated by a local electric field to kinetic energies, large enough to create excitons via collisions with other charge carriers [113]. These excitons can then decay radiatively. Electroluminescence caused by this mechanism was observed by several groups [9, 10, 114, 115]. In contrast to ambipolar recombination, impact excitation requires a local electric field in a unipolar device, that can be caused by a heterogeneous SWCNT-substrate coupling [9], defects [114], the band bending at the contacts [10] or by a sufficiently large bias voltage. These two, commonly accepted, mechanisms to explain electroluminescence emission from semiconducting SWCNTs under ambipolar and unipolar transport are consistent with the observed electroluminescence spectra reflecting the excitonic states of semiconducting SWCNTs. However, there is no uniform picture that explains electroluminescence emission from biased metallic SWCNTs. Electroluminescence from metallic SWCNTs was first observed by Mann et *al.* [116]. The authors reported on electroluminescence emission from metallic SWCNTs, that is strong for suspended and weak for non-suspended SWCNTs. The proposed explanation is based on efficient Joule heating of the suspended SWCNTs due to the lack of substrate cooling. Joule heating can lead to a thermal population of the first and second state close to the van Hove singularities. The excited carriers then can relax radiatively via interband transitions, leading to a diameter dependent emission energy. Weak emission from on-substrate SWCNTs was explained by the same process, being much weaker due to efficient cooling by the substrate. They also observed Joule heating for semiconducting SWCNTs, indicating that the thermal effect may play a role in any suspended SWCNT device. A similar low-temperature study of the same group confirmed their model [117]. In [118] a systematic study of suspended metallic and semiconducting SWCNT in a broad spectral range, from the visible to the IR, is presented. Metallic SWCNTs exhibit an electroluminescence peak in the visible range corresponding to their E_{11}^M transition, semiconducting in the infrared (E_{11}^S-transition). In addition to the sharp peaks they observe a non-polarized background that they attribute to black-body radiation.

Essig et *al.* suggested another mechanism to explain their observed electroluminescence emission in metallic, on-substrate SWCNTs and few layer graphene [119]. They ruled out thermal heating due to efficient substrate cooling. In contrast to [116], they observed two electroluminescence emission peaks at 1.4 eV and 1.8 eV that do not depend on the SWCNT diameter. Therefore, the emission could not be assigned to interband transitions at the K-point as done in [116]. Instead, they propose relaxation from the M-point, where

electronic states exist that do not depend on the nanotube diameter. This requires the emission or absorption of an optical phonon leading to the observed double feature in the spectrum. They observe the same spectral signature for few-layer graphene supporting their assumption.

To summarize, four different mechanisms explaining electroluminescence are described in the literature that in principle can contribute to the emission in a given device to a varying degree. The impact of each mechanism is determined by the particular device configuration. Despite the large number of reported electroluminescence studies, only limited information on the size of the electroluminescence source, i. e. the length of the emitting CNT segment, is available.

3. Principles of tip-enhanced near-field optical microscopy

Since the development of the first microscope in the late 16th and early 17th century, optical microscopy has undergone continuous advancements in terms of imaging quality, magnification and spatial resolution. In the early days, the microscopes suffered mainly from the poor quality of the lenses available. Nowadays, high-quality objectives providing highest numerical apertures and reduced abberations are employed in optical investigations in all natural sciences. A large pool of different microscopic techniques exist and can be used to study objects as small as cells and tissues in life science, for example. However, despite of the high quality of the available objectives, for the investigation of even smaller objects, such as single molecules or nanostructures, the spatial resolution of the best microscope is not sufficient. There is a physical, non-technical limitation of the spatial resolution of a microscope that is caused by the wave nature of light known as the *diffraction limit*.
In a confocal scanning laser microscope, a standard tool for optical investigations of nanostructures, the diffraction limit is determined by the laser wavelength and the the numerical aperture of the objective used. The lateral and axial resolution can be improved by using shorter wavelengths or by increasing the numerical aperture of the objective. However, in order to achieve substantial improvements, a super-resolution approach is required. Super-resolution techniques are either based on a far-field or near-field concept. Far-field concepts such as photoactivated localization microscopy (PALM), stochastic optical reconstruction microscopy (STORM) and stimulated emission depletion microscopy (STED) are limited to date to fluorescent samples. Near-field concepts such as scanning near-field optical microscopy (SNOM) or tip-enhanced near-field optical microscopy (TENOM) are more versatile and applicable to a large variety of sample materials [120]. However, because SNOM and TENOM exploit the short-ranged electromagnetic fields in the vicinity of a probe in close proximity to the sample surface, these techniques are limited to surface or sub-surface studies.

This chapter focuses on tip-enhanced near-field optical microscopy, introducing the basic principle. The first part deals with the diffraction limit using the angular spectrum representation of optical fields as a mathematical tool. In the second part, the key element of a tip-enhanced near-field optical microscope, the optical antenna, and its role for the signal enhancement is introduced. In TENOM, the optical antenna is usually a sharp metal tip

and the electric field enhancement for this special antenna is discussed in the next section. So far, TENOM was mostly applied to perform spectroscopy, but could also be used in optoelectronic applications. Different antenna-enhanced applications are outlined in the last section introducing three different antenna schemes: the spectroscopy, photovoltaic and electroluminescence scheme. At the end, the respective signal enhancement mechanism for each scheme is discussed.

3.1. The diffraction limit

Heisenberg's uncertainty relation, applied to photons, states that a large uncertainty in the momentum Δp_x of a photon in a certain spatial direction x is accompanied by a small position uncertainty Δx in the same direction:

$$\Delta p_x \cdot \Delta x \approx h, \tag{3.1}$$

where h is Planck's constant. Several forms of the uncertainty relation exist, exhibiting different factors on the right hand side of the equation. Eqn. 3.1 is the original form used by Heisenberg [121] and the $\approx$-sign accounts for the different definitions of the uncertainties that exist.
The momentum and the wavevector component are connected via $p_x = \hbar k_x$. Eqn. 3.1 then turns to

$$\Delta k_x \cdot \Delta x \approx 2\pi, \tag{3.2}$$

The same relation is valid for the other two spatial directions y and z. In other words, a large spread in wavevector components, or spatial frequencies, leads to a strong confinement in the respective spatial direction, i. e. a high spatial resolution.
Following this principle, the resolution limit of an optical microscope can be ascribed to limited spatial frequencies being carried from the sample to the detector. Treating light as electromagnetic waves, this loss of spatial frequencies is caused by the diffraction of light occuring in two steps: at very small distances from the sample $r \ll \lambda$, in the near-field of the emitter, high spatial frequencies are lost upon propagation due to Fresnel diffraction. At larger distances $r \gg \lambda$, or in the far-field, Frauenhofer diffraction at collecting and focusing lenses leads to a further reduction of the spread of spatial frequencies. In the following, these issues will be mathematically described using the *angular spectrum representation*, a mathematical tool to describe the propagation of light, expressing optical fields as a superposition of plane waves and evansescent waves with different propagation directions and amplitudes.
The angular spectrum representation can be applied to investigate how the electric field emanating from any kind of scatterer evolves along a certain spatial direction. The exact problem is depicted in Fig. 3.1: let $\mathbf{E}(x, y, z) = \mathbf{E}_{inc} + \mathbf{E}_{scat}$ be the electric field emanating from a scatterer located at $z = 0$. The propagation direction is z. Assuming that the

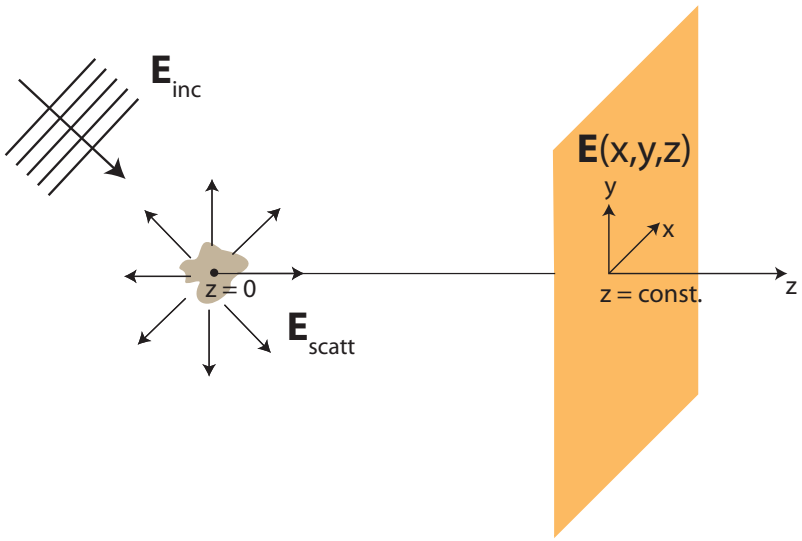

Fig. 3.1. Schematic of an optical scattering problem. The emanating electric field $\mathbf{E}(\mathbf{x},\mathbf{y},\mathbf{z}) = \mathbf{E}_{inc} + \mathbf{E}_{scat}$ from a scatterer at position $z = 0$ can be evaluated in planes perpendicular to an arbitrary chosen direction of propagation z using the angular spectrum representation.

electric field at the position of the scattering source $\mathbf{E}(x, y, z = 0)$ is known, the angular spectrum representation can be used to calculate the electric field in planes at any other position z perpendicular to the propagation direction. This is straightforward in reciprocal space. The Fourier transformation of the field $\mathbf{E}$ at any position z is given by

$$\hat{\mathbf{E}}(k_x, k_y; z) = \frac{1}{4\pi^2} \iint_{-\infty}^{+\infty} \mathbf{E}(x, y, z) e^{-i[k_x x + k_y y]} \mathrm{d}x\mathrm{d}y, \tag{3.3}$$

where x, y, z are the real space coordinates and k_x, k_y, k_z the coordinates of the reciprocal space. In reciprocal space the propagation in z-direction can be mathematically described by multiplying the electric field with a *propagator*. Assuming a source-free, linear, isotropic homogeneous medium, the propagator is determined by solving the Helmholtz equation and is given by $e^{\pm ik_z z}$, with $\pm$ indicating the direction of propagation [122]. The Fourier spectrum $\hat{\mathbf{E}}$ therefore evolves along z as

$$\hat{\mathbf{E}}(k_x, k_y; z) = \hat{\mathbf{E}}(k_x, k_y; 0) \cdot e^{\pm ik_z z} \tag{3.4}$$

The electric field in real space can then be obtained by taking the inverse Fourier transform of Eqn. 3.4 yielding

$$\mathbf{E}(x, y, z) = \iint_{-\infty}^{+\infty} \hat{\mathbf{E}}(k_x, k_y; 0) \cdot e^{i[k_x x + k_y y + k_z z]} \mathrm{d}k_x \mathrm{d}k_y, \tag{3.5}$$

assuming a propagation direction towards positive z, yielding a propagator $e^{+ik_z z}$. The propagation along z is determined by the respective wave vector component k_z appearing in the propagator. k_z can be expressed as

$$k_z = \sqrt{k^2 - k_x^2 - k_y^2}. \tag{3.6}$$

Here, k is the magnitude of the wavevector given by

$$k = \frac{2\pi n}{\lambda}, \tag{3.7}$$

with λ being the wavelength and n the refractive index that is a real, positive quantity for a purley dielectric medium with no losses.

One can distinguish two cases:

1. $k_x^2 + k_y^2 \leq k^2$
   k_z is real and the propagator is an oscillating function $e^{i|k_z|z}$. The waves described by Eqn. 3.5 are therefore propagating plane waves. These propagating waves belong to the far-field of the emitter and are able to carry information to the detector.

2. $k_x^2 + k_y^2 > k^2$
   k_z is imaginary and the propagator turns to an exponentially decaying function $e^{-|k_z|z}$. The assocciated waves decay therefore exponentially along z with a decay length of $\frac{1}{|k_z|} \ll \lambda$ associated with the near-field of the emitter that does not reach the detector in conventional optics.

Considering the near- and the far-field of an emitter, the angular spectrum representation is a superposition of plane and evanescent waves and can be divided into two parts

$$\mathbf{E}(x,y,z) = \iint\limits_{k_x^2+k_y^2 \leq k^2} \hat{\mathbf{E}}(k_x,k_y;0) \cdot e^{i[k_x x + k_y y]} e^{i|k_z|z} \mathrm{d}k_x \mathrm{d}k_y \tag{3.8}$$

$$+ \iint\limits_{k_x^2+k_y^2 > k^2} \hat{\mathbf{E}}(k_x,k_y;0) \cdot e^{i[k_x x + k_y y]} e^{-|k_z|z} \mathrm{d}k_x \mathrm{d}k_y \tag{3.9}$$

The first part is the superposition of plane waves, the second of evanescent waves, respectively. With increasing distance to the source, the evanescent waves connected to large spatial frequencies decay rapidly. This loss of spatial frequencies, that takes place in the near-field of the emitter, is known as *Fresnel diffraction*. This is connected to a loss of spatial information and therefore entails a reduction of the spatial resolution. Considering the spatial direction x, the maximum spread of k_x is then given by the interval [-k...k], i. e. twice of the length of the wave vector k. Following Heisenbergs's principle (Eqn. 3.1), the resulting, theoretically achievable, spatial resolution in x is then given by

$$\Delta x_{min} \approx \frac{\lambda}{2n}. \tag{3.10}$$

However, not all these plane waves can reach the detector due to the limited collection angle of the objective or other focusing elements used in the beam path. This loss of spatial frequencies takes place in the far-field of the emitter and is known as *Fraunhofer diffraction*. The collection efficiency of a lens or an objective is determined by the *numerical aperture* NA defined as

$$NA = n \cdot \sin \alpha, \tag{3.11}$$

where n is the refractive index of the medium between the lens and the focus, and α is half of the opening angle as shown in Fig. 3.2. Waves emitted at angles exceeding α (indicated in yellow in Fig. 3.2), cannot be collected by the objective.

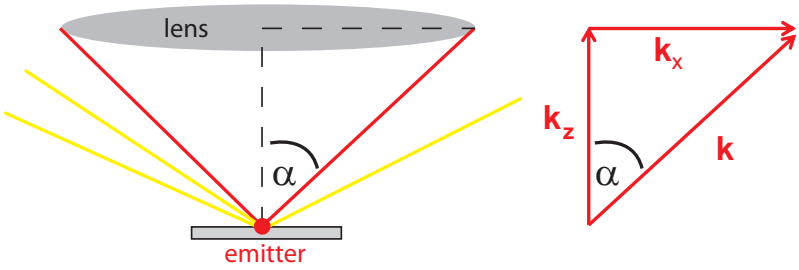

Fig. 3.2. Collection efficiency of a lens. Waves emitted at an angle smaller than the angle α can be collected by the lens, whereas waves at an angle larger than α depicted in yellow are lost. The maximum wavevector component collected by the lens is given by $k_{x,max} = k \cdot \sin \alpha$.

The maximum spatial frequency of waves that can be collected by the objective with numerical aperture NA (see Fig. 3.2) is given by

$$k_{x,max} = k \cdot \sin \alpha = \frac{2\pi}{\lambda} \cdot NA \tag{3.12}$$

The resolution limit formulated in Eqn. 3.10 therefore turns to

$$\Delta x_{min} \approx \frac{\lambda}{2NA}. \tag{3.13}$$

Many formulations of the resolution limit based on different criteria exist. The most common among them was given by Erns Abbe in 1873. He derived his expression for two parallel, dipolar emitters with axes perpendicular to the optical axis. The image of a point source at the detector is known as *point-spread function (PSF)* and is given by an Airy pattern [122]. He stated that the two point-dipoles are still resolvable if the maximum of the PSF of one emitter coincides with the first minimum of the PSF of the second emitter. Considering the functional form of the PSF, that is known as Airy function, this yields the following expression [122]

$$\Delta x_{min} = 0.61 \frac{\lambda}{NA}. \tag{3.14}$$

3.2. Principle of near-field optical microscopy

According to the resolution limit formulated by Abbe (Eqn. 3.14), the spatial resolution of a microscope can be improved by decreasing the excitation wavelength or increasing the numerical aperture (see Eqn. 3.14). However, in order to achieve a substantial improvement, one must increase the bandwidth of spatial frequencies by retaining the spatial frequencies associated with the evanescent waves of both the excitation source and the emitter. Therefore, one cannot use a standard lens for focusing, but a nanoscale object, a probe, that can be brought very close to the sample in order to provide efficient coupling between the probe's near-field and the emitter, and the emitter's near-field and the probe. This probe, often denoted as *optical antenna*, can focus the light to a sub-diffraction volume and excites the sample via the evanescent waves of its near-field. Equivalently, the emitted light from the sample is radiated via the antenna, retaining therefore the evanescent waves by coupling them to the far-field [122]. As a consequence, a much larger range of spatial frequencies reaches the detector, leading to an improvement of spatial resolution by more than one order of magnitude. In principle, the spatial resolution is limited only by the degree of light confinement determined by the antenna dimensions.

3.3. Optical antennas

The key element that provides efficient coupling between the near-field to the far-field is an optical antenna [27, 123–125].

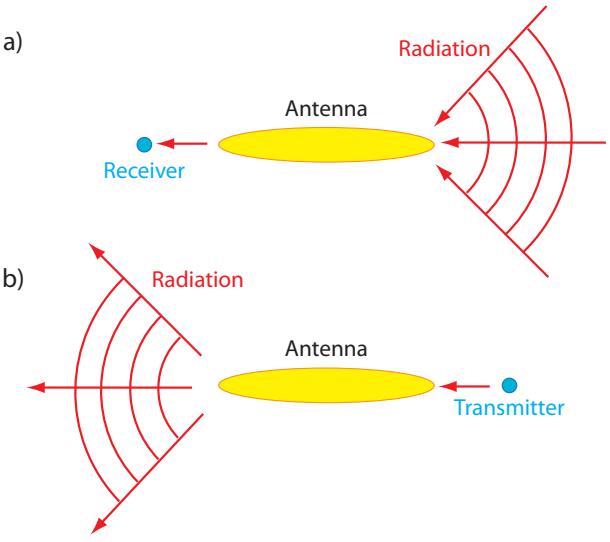

Fig. 3.3. Coupling of an antenna to an emitter. The antenna can operate as a) receiver or b) transmitter. The arrows indicate the direction of energy flow. Depending on its function as receiver or emitter, the antenna enhances the excitation and/or emission rates.

Similar to radio- and microwave antennas, the purpose of an optical antenna is to convert the energy of free propagating radiation into localized energy, and *vice versa* [124]. This localized energy can be used to optically excite a receiving object that is in the near-field of the antenna's feed point, leading to enhanced absorption of radiation (see Fig. 3.3) in a nanoscale volume [120]. Conversely, energy released by a transmitting object can be radiated more efficiently.

In general, the size of an antenna always scales with the wavelength of the radiation it is supposed to interact with. Therefore, optical antennas have dimensions on the order of the wavelength of visible light or even smaller, and require

high fabrication accuracies in the range of few nanometers. Thanks to the progress in the development of nanofabrication techniques, the precise and controlled fabrication of optical antennas became possible at all.

Due to the increase of the bandwidth of spatial frequencies, an optical antenna enhances both absorption and emission rates leading to increased spatial resolution and detection sensitivity. The following discussion of the signal enhancement by an optical antenna is based on [120, 124, 125].

The absorption enhancement is given by the ratio of the absorption cross section with and without antenna $\frac{\sigma}{\sigma_0}$. The absorption cross section in presence of an antenna is also called *antenna aperture* and formally defined as

$$A(\Theta, \Phi, \mathbf{n}_{pol}) = \frac{P_{exc}}{I(\Theta, \Phi)}. \tag{3.15}$$

The antenna aperture A corresponds to the absorption cross section σ and describes, how efficiently an antenna captures the radiation of intensity I and polarization $\mathbf{n}_{pol}$ from a certain direction (Θ, Φ) to excite the receiver with power P_{exc}. Assuming a dipolar receiver oriented along $\mathbf{n}_p$, P_{exc} is proportional to $|\mathbf{n_p} \cdot \mathbf{E}|^2$, where $\mathbf{E}$ is the local electric field at the position of the receiver in the presence of the antenna. Therefore,

$$\frac{\sigma(\Theta, \Phi, \mathbf{n}_{pol})}{\sigma_0(\Theta, \Phi, \mathbf{n}_{pol})} = \frac{|\mathbf{n_p} \cdot \mathbf{E}|^2}{|\mathbf{n_p} \cdot \mathbf{E_0}|^2}, \tag{3.16}$$

This expression emphasizes that the antenna aperture or the absorption cross section in general depends on the direction of incidence and the polarization. Neglecting this issue, Eqn. 3.16 simplifies to

$$f = \frac{E}{E_0}. \tag{3.17}$$

Here, the field enhancement factor f was introduced. Enhanced emission can be discussed in terms of the *antenna radiation efficiency* ϵ_{rad} and *gain* G. The antenna efficiency is defined as

$$\epsilon_{rad} = \frac{P_{rad}}{P}, \tag{3.18}$$

where P is the total dissipated power that also includes losses in both the antenna and the receiver, and P_{rad} is the radiated power. The antenna gain describes the radiated power in a certain direction (Θ, Φ) normalized with the total dissipated power P:

$$G(\Theta, \Phi) = \epsilon_{rad} D(\Theta, \Phi), \tag{3.19}$$

with D being the *antenna directivity*, a measure of the antenna's capability to concentrate the radiation in a certain direction (Θ, Φ). It is defined as

$$D(\Theta, \Phi) = \frac{4\pi}{P_{rad}} p(\Theta, \Phi), \tag{3.20}$$

where $p(\Theta, \Phi)$ is the angular power density.
Using the reciprocity theorem, the following relationship between the excitation and the radiation rate of the emitter can be obtained [124]:

$$\frac{k_{ex,\Theta}(\Theta,\Phi)}{k^0_{ex,\Theta}(\Theta,\Phi)} = \frac{k_{rad}}{k^0_{rad}} \frac{D_\Theta(\Theta,\Phi)}{D^0_\Theta(\Theta,\Phi)}, \tag{3.21}$$

where the subscript 0 indicates the absence of the antenna and Θ the polarization direction. A similar expression can be derived for polarization in the Φ direction. This equation states that the radiative rate enhancement is proportional to the excitation rate enhancement. Interestingly, excitation in a direction of high directivity allows the excitation rate to be enhanced more strongly than the radiative rate [124, 125]. Neglecting this, by assuming the same directivity for enhanced and non-enhanced fields, the radiative rate enhancement is again proportional to the square of the field-enhancement factor

$$\frac{k_{rad}}{k^0_{rad}} = \frac{E}{E_0} = f^2. \tag{3.22}$$

3.4. Electric field enhancement at a metal tip

There is a large variety of optical antenna designs that include different materials and shapes often mimicking their counterpart in the radio frequency regime. The progress in nanoscale fabrication technologies enables more and more sophisticated and complex antenna designs. Any optical antenna consists of a plasmonic nanostructure fabricated either with a top-down technique, such as electrochemical etching and focused ion-beam milling or with a bottom-up technique, as in colloidal chemistry. An overview over different realizations of optical antennas is given in [120].
Probably the most common optical antennas used in TENOM experiments are sharp, solid silver or gold tips. Due to their sharply pointed geometry, enhanced electric fields can form at the tip apex upon illumination. When irradiated with light polarized along the tip axis, a high suface charge density associated with a strong electric field is created at the tip apex. This is not the case for light polarized perpendicular to the tip axis, because the foremost part of the tip remains uncharged. Simulations of the electric field distribution of a metal tip and a metal sphere with the same diameter reveal a much stronger field enhancement for a tip than for a sphere upon excitation with a polarization along the tip axis (see Fig. 3.4 c) and d)). In case of polarization perpendicular to the tip axis (Fig. 3.4 a) and b)), the electric field at the tip apex is much weaker than for the sphere.
Polarization along the tip axis using a standard Gaussian HG_{00} mode can be achieved by a side illumination scheme. For an inverted microscope, where the illumination occurs from below the sample, a HG_{10} laser mode, that has a strong field component in the direction of propagation, must be used (see also Sec. 4.2.1).
In principle, this lightning rod effect is expected to occur for any sharp metal tip. However, in practice, mostly gold or silver tips are used as antennas in optical near-field experiments,

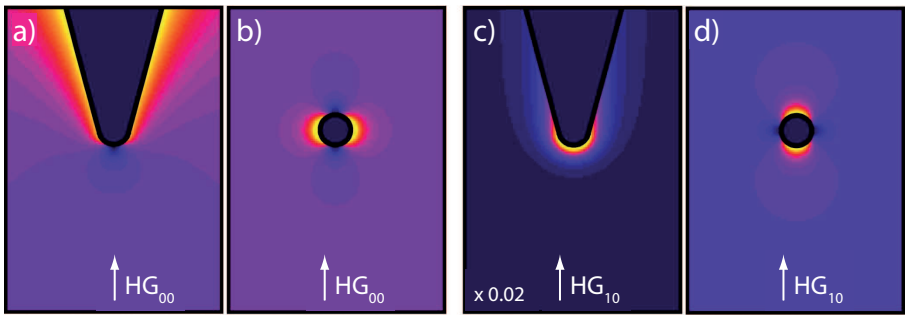

Fig. 3.4. Electric field distribution for a metal tip and a metal sphere for two different excitation polarizations. (a, b) Excitation with a Hermite-Gaussian HG_{00} beam. (c, d) Excitation with a focused HG_{10} beam with a strong electric field component along the tip axis. The simulations show that the electric field distribution near the tip apex is similar to the dipole fields of a metal sphere, but much stronger in case of longitudinal excitation. Figure taken from [122].

.

because these metals can exhibit plasmon resonances in the visible wavelength region leading to even stronger enhanced fields.

In general, as illustrated in Fig. 3.4, the field in the vicinity of the tip can be approximated by the field generated by an electric dipole μ located at the center of the tip with magnitude [122]

$$\boldsymbol{\mu} = \begin{bmatrix} \alpha_\perp & 0 & 0 \\ 0 & \alpha_\perp & 0 \\ 0 & 0 & \alpha_\parallel \end{bmatrix} \mathbf{E}_0. \tag{3.23}$$

Here, $\alpha_\perp$ and $\alpha_\parallel$ denote the transverse and longitudinal polarizabilities, with the tip axis coinciding with the z-direction. $\mathbf{E}_0$ is the exciting field in absence of the tip. $\alpha_\perp$ is given by the polarizability of a metal sphere and $\alpha_\parallel$ is dependent on the field enhancement factor. In general, $\alpha_\parallel$ is much larger than $\alpha_\perp$.

The excitation field at the sample position is then the sum of the incident field $\mathbf{E}_0$ and the enhanced field emanating from the tip dipole $\boldsymbol{\mu}$, leading to a far-field and a locally enhanced near-field contribution of the signal. Therefore, in a typical TENOM experiment, the detected intensity consists of a diffraction limited, far-field background and a sub-diffraction, enhanced near-field contribution. The near-field to far-field intensity ratio determines the image contrast. In order to determine the local signal enhancement factor, the respective intensities must be normalized by the corresponding far-field and near-field interaction volume. The far-field volume is determined by the confocal excitation volume and the dimensionality of the sample material. In case of a 1D material such as carbon nanotubes, with a typical focus diameter of about 300 nm and a tip diameter of 20 nm, this ratio is given by $\frac{V_{FF}}{V_{NF}} = \frac{300}{20} = 15$. With increasing dimensionality of the sample material, the confocal background intensity gets larger. In order to maintain a reasonable image contrast also for larger confocal volumes in case of 2D or 3D materials, two different approaches exist: increasing the near-field intensity or decreasing the far-field

background. The former can be achieved by optimizing the enhancement using a different antenna design. The latter can be realized by avoiding direct exposure of the sample to the laser beam using particular antenna types, or by separating the far-field background from the near-field signal [120].

3.5. Antenna-enhanced applications

Due to the locally enhanced electric fields provided by optical antennas, these structures, in particular sharp gold tips, could be used to enhance multiple optical responses such as Raman scattering, fluorescence and photoluminescence, but also optolelectronic signals such as photocurrent and electroluminescence [120].
A schematic overview on the possible antenna-enhanced interactions is given in Fig. 3.5, and the signal enhancement for each scheme is discussed in the following.

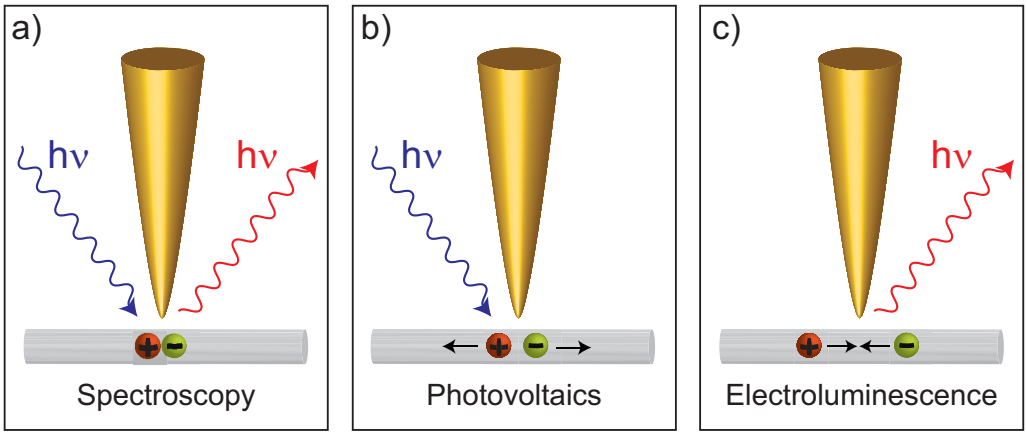

Fig. 3.5. Proposed applications of antenna-enhancement. a) Spectroscopy b) Photovoltaics c) Electroluminescence. In the spectroscopy scheme, both excitation and radiation are enhanced, whereas in the photovoltaic or electroluminescence scheme only the excitation or radiation is enhanced. Figure adapted from [124].

3.5.1. Spectroscopy

In the spectroscopy scheme, both the excitation and the radiation rates are enhanced by the antenna as discussed in the previous section. Neglecting the polarization and angular dependence, both the excitation and radiative rate enhancement scales with the square of the electric field enhancement factor f. This can be exploited to record optical signals such as Raman scattering and photoluminescence with sub-diffraction spatial resolution and enhanced detection sensitivity. The enhancement factor f is in general wavelength dependent and therefore different for the excitation and the emission.
In the case of **Raman scattering**, where the shift between the wavelength of the incident and scattered light is small, this can be neglected and the total Raman signal therefore scales with the fourth power of the enhancement factor:

$$M_{Raman} \approx \frac{k_{ex}}{k_{ex}^0}\frac{k_{rad}}{k_{rad}^0} \approx f^4, \tag{3.24}$$

where M_{Raman} denotes the total signal enhancement.
The fluorescence or photoluminescence intensity depends in general on the excitation rate k_{ex} and the quantum yield q, that is defined as the ratio between the radiative decay rate and the total decay rate $q = \frac{k_{rad}}{k_{rad}+k_{nonrad}}$. As in case of Raman scattering, the excitation rate enhancement scales with the square of the enhancement factor. The radiative rate enhancement is given by the ratio of the quantum yields with and without antenna. The presence of an antenna can enhance the radiative rate, but also the non-radiative rate of the fluorescent state by metal-induced quenching at very small antenna-sample distances. The total signal enhancement M_{Fluo} can therefore be approximated by

$$M_{Fluo} \approx \frac{k_{ex}}{k_{ex}^0}\frac{q}{q^0} \approx f^2\frac{q}{q^0}. \tag{3.25}$$

From this equation it gets clear, that the radiative rate enhancement is very efficient for emitters with a low intrinsic quantum yield q^0 such as carbon nanotubes. Assuming also a negligible influence of the antenna on the non-radiative decay rate, as given for sufficient large antenna-sample distances, Eqn. 3.25 simplifies to

$$M_{Fluo} \approx f^2\frac{k_{rad}}{k_{rad}^0} \approx f^4 \tag{3.26}$$

for emitters with a low quantum yield. In this case, the total signal enhancement scales with the fourth power of the enhancement factor as for Raman scattering.
For emitters with a high intrinsic quantum yield $q^0 \approx 1$ such as distinct fluorescent molecules, the quantum yield cannot be further enhanced and the total signal enhancement is given by the excitation rate enhancement

$$M_{Fluo} \leq f^2. \tag{3.27}$$

The <-sign accounts for metal-induced quenching.
It needs to be emphasized that both Eqn. 3.24 and Eqn. 3.25 are only approximations, neglecting the angular and polarization dependence of the directivity. In addition, the signal enhancement depends on the wavelength due to the wavelength dependence of the antenna gain and therefore can be very different for the incident and emitted radiation. This wavelength dependence becomes in particular relevant for fluorescence and photoluminescence exhibiting large Stokes shifts and broad emission spectra. Therefore, the spectral intensity distribution can be very different for an emitter in presence or absence of the antenna.

3.5.2. Photocurrent and electroluminescence

Optoelectronic signals in general are expected to exhibit a smaller enhancement than purley optical signals. Compared to the spectroscopy scheme discussed above, where both excitation and emission are enhanced, photocurrent and electroluminescence can only benefit from either excitation or emission rate enhancement as illustrated in Fig. 3.5 b) and c). Following the photovoltaic scheme, only the excitation can be enhanced, leading to an increased photocurrent. In case of electrically-induced electroluminescence, the reverse of the photovoltaic scheme, only the emission is enhanced. Therefore, both optoelectronic signals are expected to scale with the square of the enhancement factor f:

$$M_{PC} \approx f^2 \tag{3.28}$$

$$M_{EL} \approx f^2 \tag{3.29}$$

The enhancement of optoelectronic signals is only comparable to the fluorescence enhancement for emitters with a very high quantum yield (see Eqn. 3.27), but in general it is expected to be weaker. In case of electroluminescence, metal-induced quenching can further decrease the enhancement as in case of fluorescence. This leads to a reduced detection sensitivity for optoelectronic signals. In addition, a smaller enhancement is related to a lower spatial resolution. This is derived in the following, by comparing the spatial resolution for Raman scattering and photocurrents.
The field enhancement factor f is in fact a function of position with respect to the tip apex. Assuming a radially symmetric tip, it can be described by a three dimensional Gaussian function with its maximum at the tip apex. Its spatial width w is determined by the tip geometry and determines the spatial resolution of the measurement. In a given spatial direction, f can be expressed as

$$f(r) = f_0 \cdot e^{-\frac{r^2}{2w^2}}. \tag{3.30}$$

Here, f_0 denotes the maximum enhancement factor given at the tip apex.
In case of photocurrent, the signal enhancement M_{PC} is proportional to f^2 (Eqn. 3.29), i. e.

$$M_{PC} \propto f^2(r) \propto e^{-\frac{r^2}{w^2}} = e^{-\frac{r^2}{2w_{PC}^2}}. \tag{3.31}$$

For Raman scattering the signal enhancement is proportional to the fourth power of f (Eqn. 3.29), i. e.

$$M_{Raman} \propto f^4(r) \propto e^{-\frac{2r^2}{w^2}} = e^{-\frac{r^2}{2w_R^2}}. \tag{3.32}$$

w_{PC} and w_R denote the spatial width of the photocurrent, Raman signal respectively. For a carbon nanotube or any other 1D structure, it can be experimentally determined by extracting the cross section perpendicular to the carbon nanotube. From Eqn. 3.31 it is

clear, that the square of the enhancement factor with spatial width w is again a Gaussian function, but with a smaller spatial width w_{PC}. Squaring it one more time to obtain the signal enhancement for Raman scattering, yields again a Gaussian function with an even smaller width w_R. From Eqn. 3.31 and Eqn. 3.32 it follows that

$$\frac{w_{PC}}{w_R} = \frac{1}{\sqrt{2}}. \tag{3.33}$$

Hence, for photocurrents a spatial resolution, that is lower by a factor of $\sqrt{2}$ than for Raman scattering, is expected.

4. Experimental approach

This chapter reports on the experimental methods used within the scope of this work. In the first part, details on the sample fabrication are given including different carbon nanotube sample materials and the electrode patterning with electron beam and optical lithography. Both types of lithography were performed using the clean room facilities of the group of Prof. Kotthaus at the Department of Physics at the LMU Munich. In the second part, the optical microscope setup for Raman and optoelectronic measurements is presented. Information on both the confocal configuration based on an inverted oil-immersion microscope and the tip-enhanced near-field optical microscope are provided. At the end, the fabrication process of the optical antenna, one of the main elements of TENOM, is described.

4.1. Sample fabrication

The starting point for the fabrication of SWCNT based optoelectronic devices is a clean, bare glass substrate covered with single SWCNTs. The SWCNTs should be homogeneously distributed over the sample surface and their density should not be too high to avoid the formation of networks, but also not too low such that the resulting number of contacted SWCNTs is sufficient. Using longer SWCNTs increases the durability of the devices during electrical measurements compared to short SWCNTs and are therefore more favorable. Therefore, different SWCNT sample materials were tested and used as described in the following.

4.1.1. Carbon nanotube sample preparation

Commercial metallic SWCNTs in solution

The first optoelectronic measurements were performed using a commercial SWCNT solution purchased from the company *Nanointegris* (IsoNanotubes-M^{TM}, 98 %). It contains SWCNTs fabricated by arc discharge and dispersed in an aqueous solution containing ionic surfactants to prevent bundling. It contains 98 % metallic SWCNTs (sorted by gradient ultracentrifugation) with a diameter range of 1.2-1.7 nm (mean diameter 1.4 nm). The length of the SWCNTs is specified to 300 nm to 5 µm. In practice, only few SWCNTs turned out to be longer than 1 µm. The diameter range was chosen because the M_{11} transition of these SWCNTs is close to the excitation energy of 1.96 eV corresponding to 632.8 nm (see Fig. 2.6) enabling resonance Raman measurements. For the sample pre-

paration a small volume of the solution (30-50 µl) was spin coated onto a standard glass cover slip purchased form *Marienfeld Superior* (borosilicate, thickness 0.13-0.16 mm, 24 × 24 mm^2, refractive index ≈ 1.52). At the end, the substrate was rinsed with distilled water to remove the surfactant.

Commercial semiconducting and metallic SWCNTs in powder form

Since the IsoNanotubes-M^{TM}- solution contained only metallic and rather short SWCNTs, another sample material containing metallic and semiconducting SWCNTs fabricated by chemical vapor deposition (CVD), purchased from the company *CheapTubes*, was used. The diameter was specified to 1-2 nm and the length to 3-30 µm. The supplied form of the material was a dry powder with a purity of larger than 99 %. The powder was then dispersed with a concentration of 1 g/l in an acqueous solution of sodium cholate hydrate (1 % wt%) followed by a sonication step of 2-3 min (*Bandelin electronic*, Sonopuls HD 2200). SWCNT samples were again prepared by spin coating the solution (30-50 µl) onto a standard glass cover slip with a rinsing step at the end. Using this procedure, the actual length of the SWCNTs turned out to be larger (up to several µm) compared to the IsoNanotubes-M^{TM}.

CVD grown metallic and semiconducting SWCNTs on quartz

Another type of sample was prepared by Matthias Hofmann from the group of Prof. Högele at the Department of Physics of the LMU Munich. SWCNTs were grown onto a quartz substrate by chemical vapor deposition using an iron-ruthenium catalyst with a hydrogen/methane gas mixture at a temperature of 850 °C [126]. The high temperature needed for the growth process required the use of fused quartz substrates instead of standard glass substrate due to a higher melting point (*SPI Supplies*, thickness 0.15-0.18 mm, diameter 25 mm, refractive index of 1.48-1.46 in the visible range). Chemical vapor deposition yields pure, very long SWCNTs up to 20-30 µm of both metallic and semiconducting character with a non-specified diameter distribution.

Fig. 4.1 shows confocal Raman measurements of all three carbon nanotube sample materials following the preparation procedure described above to demonstrate the respective length distributions and SWCNT densities. While the IsoNanotubes-M^{TM} appear rather spot like and are therefore quite short, around 500 nm or even below the spatial resolution of the system. The CheapTubes can be up to few microns long. The longest SWCNTs are achieved by the CVD growth on quartz substrates shown in Fig. 4.1 c) and can be as long as 30µm. All samples are rather densly covered with single or small bundles of SWCNTs which is favorable for the further sample preparation.

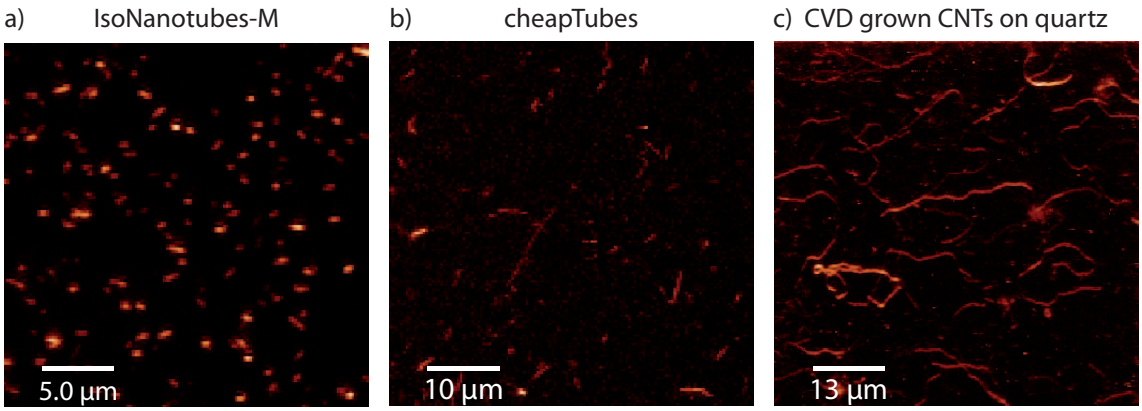

Fig. 4.1. Confocal Raman G band images of the different carbon nanotube sample materials. a) IsoNanotubes-M^{TM} b) CheapTubes c) CVD grown SWCNTs on quartz. All three measurements demonstrate a rather homogeneous distribution of presumably single SWCNTs with different length distributions. While the IsoNanotubes-M^{TM} are only few hundreds of nanometers long, CheapTubes can have lengths up to few microns and the CVD grown SWCNTs up to few tens of microns.

4.1.2. Device fabrication

SWCNTs were contacted randomly by adding metal electrodes onto the glass substrate covered with SWCNTs. The metal contacts were fabricated either using electron beam lithography (EBL) or optical lithography. EBL has the advantage of providing a higher spatial resolution due to the small de Broglie wavelength of electrons compared to photons in the UV. Therefore, EBL was used for contacting short SWCNTs with a length below 1 µm due to the required small electrode distances. However, EBL is more complex and time consuming due to long writing times of several hours caused by the serial nature of the writing process with an electron beam. Optical lithography is a parallel process involving a photomask resulting in exposure times of few seconds only. Because of the lower spatial resolution, determined by the wavelength of the light source used, optical lithography could be only applied to the CVD grown nanotube samples containing a high number of long SWCNTs.

Electron beam lithography

Electron beam lithography is a standard nanofabrication technique using a scanning beam of focused electrons to write nanometer-sized structures on a substrate covered with an electron-sensitive film, the so-called resist. The most important steps involved are illustrated in Fig. 4.2.

The first step is to prepare a clean sample covered with single SWCNTs as described in Sec. 4.1.1. For EBL, substrates with short SWCNTs (either IsoNanotubes-M^{TM} or CheapTubes) were prepared (Fig. 4.2 a)). A standard negative resist used for EBL is polymethylmethacrylate (PMMA). The resist (PMMA 500k) was spin coated onto the SWCNT substrate (Fig. 4.2 b)). A soft bake on a hot plate (step not shown) was required to drive off water and the solvent. In order to prevent charging of the substrate during the e-beam

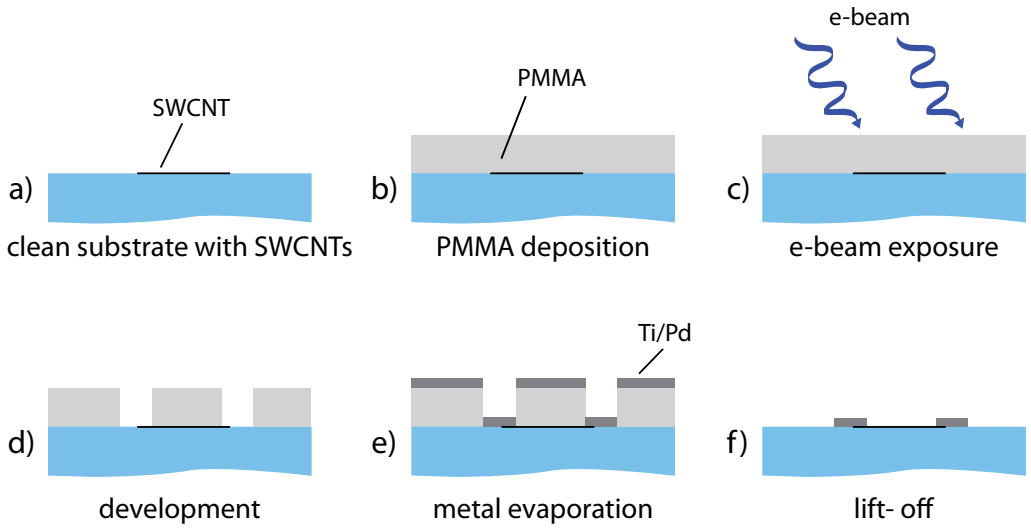

Fig. 4.2. Schematic of the involved steps to fabricate SWCNT devices using electron beam lithography. a) A clean glass substrate covered with single SWCNTs was prepared. The SWCNTs could be as short as 500 nm. b) An electron-sensitive resist (PMMA 500k) was spin coated onto the substrate. c) During the writing process the geometry of the electrode pattern according to the design shown in Fig. 4.3 was written with the electron beam. d) The exposed regions of the PMMA layer were removed during the developer process in MIBK. e) A thin metallic film (Ti/Pd) was evaporated onto the substrate with electron beam evaporation. f) The rest of the PMMA layer covered with metal was removed in a warm acetone bath (lift-off) resulting in patterned metal structures.

exposure, a thin (2 nm) discharge layer made of chromium was added by thermal evaporation (step not shown). The electron beam writing was done with an *e-LiNE Plus* system from the company *Raith* following the design shown in Fig. 4.3. The energy deposited by the electron beam changes the solubility properties of the resist (Fig. 4.2 c)). Exposed areas could then be removed from the substrate in the developer process (Fig. 4.2 d)). As a developer methyl isobutyl ketone (MIBK) was used. After stripping the discharging layer with chromium etchant (step not shown), a thin metal film (0.5 nm Ti/30 nm Pd) was deposited in a UHV deposition system (*BESTEC GmbH*) by electron beam evaporation (Fig. 4.2 e)). Here, the thin titanium film took the function of an adhesion layer. Finally, during the lift-off (Fig. 4.2 f)) the residual resist and unnecessary metal was removed in a warm acetone bath supported by weak pipette bubbling and ultrasound to prevent damaging the metal structures.

Optical lithography

For contacting the CVD grown SWCNTs on quartz optical lithography was employed. Due to their larger length, the spatial resolution offered by optical lithography was sufficient. A photomask was fabricated by Claudia Paulus at the Walter Schottky Institute in Garching. A photomask typically is a chrome covered plate showing a transparent pattern defined by the design shown in Fig. 4.4.

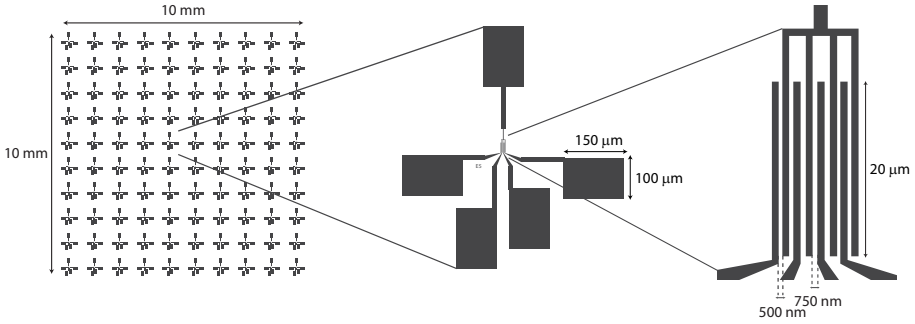

Fig. 4.3. Geometric design with dimensions used for the electron beam writing. The design was a 10 × 10-array (10 × 10 mm^2) labeled with coordinates. One array element consisted of eight bar-shaped electrodes with a separation of 750 nm, 500 nm respectively. Four electrodes were connected to one common large contact pad, the other four to four individual contact pads.

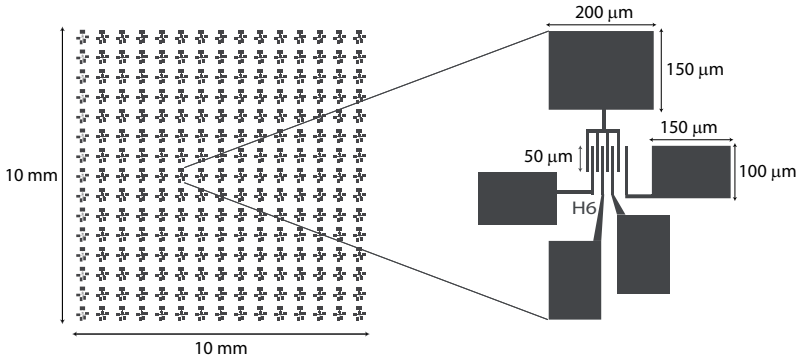

Fig. 4.4. Geometric pattern and dimensions of the photomask used. The design was a 15 × 15-array labeled with coordinates. One array element consisted of eight bar-shaped electrodes. Four of them were connected to one large contact pad, four of them to individual contact pads, respectively.

The distances between the eight bar-shaped electrodes varied between 3 and 10 µm. The electrodes were connected to large contact pads that could be contacted with a macroscopic metal needle.

Optical lithography involves similar steps as electron beam lithography. A schematic is shown in Fig. 4.5. Instead of PMMA the positive photoresist Microposit S1813 was spin coated onto the quartz substrate (Fig. 4.5 b)) followed by a soft bake on a hot plate (step not shown). The substrate was then exposed to UV light through the transparent regions of the photomask (Fig. 4.5 c)) using a mask aligner from *Suss/Microtec* (model MJB3 with a 200 W mercury vapor lamp). Due to the exposure to UV light the photoresist became soluble in the developer solution (Microposit 351) and was therefore able to be removed (Fig. 4.5 d)). As an electrode material titanium (30 nm) or gold (30 nm) using titanium as an adhesion layer (0.5 nm) was evaporated (Fig. 4.5 e)). The lift-off in a warm acetone bath with ultrasound removed the residual photoresist (Fig. 4.5 f)) resulting in the desired metal structures.

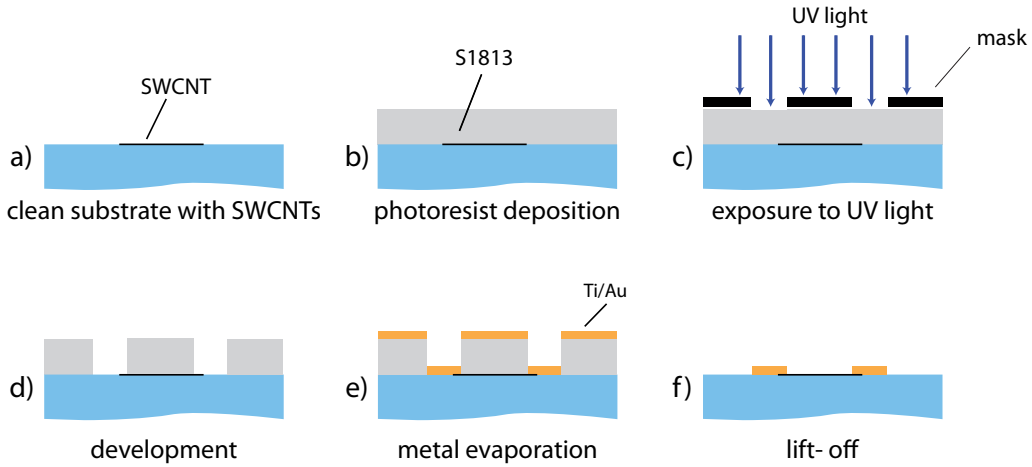

Fig. 4.5. Schematic of the involved steps to fabricate SWCNT devices on a quartz substrate using optical lithography. a) Preparation of a clean quartz substrate with long, single CVD grown SWCNTs. b) The substrate was covered with a photoresist (Microposit S1813). c) The substrate was exposed through a photomask to UV light. d) The photoresist was removed at the exposed areas using the developer Microposit 351. e) Evaporation of a thin metallic film (Ti or Ti/Au). f) The photoresist and the metal covering the non-exposed areas was removed in a warm acetone bath (lift-off).

4.2. Experimental setup for Raman and optoelectronic measurements

4.2.1. Confocal microscope setup

A schematic of the confocal laser setup used for diffraction limited measurements is presented in Fig. 4.6. According to the type of measurement - Raman, electroluminescence or photocurrent - the setup needed a few modifications.

For **Raman measurements** two different continuous wave lasers were used. Standard Raman measurements were performed with a helium-neon laser emitting at 632.8 nm (*Thorlabs*, output power 21 mW). Alternatively an argon-krypton laser (*Spectra Physics*, Stabilite 2018) can be fiber coupled in offering several laser lines in the visible range. For Raman measurements two lines at 514.5 nm and 568.2 nm were used. Few Raman measurements were performed using a Ti:Sapphire laser tuned to 834 nm (*Coherent* Mira), integrated into a similar confocal setup. For each wavelength a different set of filters, including a laser line filter (LF) in the excitation path and a sharp Raman edge (RE) filter plus a band pass filter (BP) in the detection path, was needed. Since the radial breathing mode of SWCNTs has a very small Raman shift close to the laser line (100 to 300 cm^{-1}), RE filters with a very small transition width of smaller 100 cm^{-1} were required (*Semrock*, RazorEdge®).

The excitation path consisted of two pairs of lenses expanding the beam to a diameter of about 1 cm such that it filled the back aperture of the objective to benefit from its high numerical aperture. In the focus between the second pair of lenses a pinhole (PH) was used for spatial filtering.

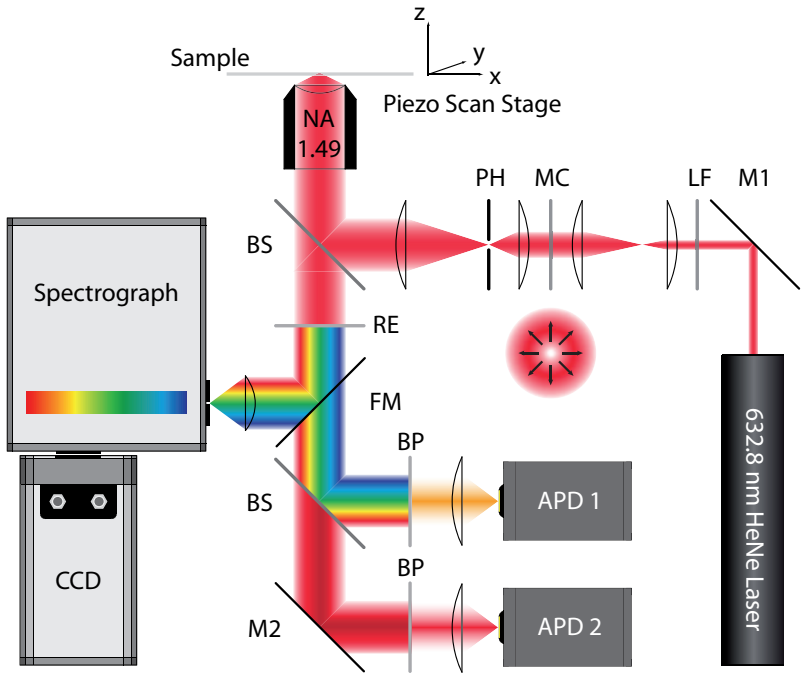

Fig. 4.6. Schematic of the confocal setup used for optical measurements. A laser was coupled into the excitation path via mirror M1 consisting of a laser line filter (LF), two pairs of lenses for beam expansion, a pinhole (PH) and a mode converter (MC) (optional). The laser was reflected onto the objective by a beam splitter (BS) and focused onto the sample. The backscattered laser light was blocked by a Raman edge filter (RE). The detection path was split into two channels, one for the visible and one for the near-infrared spectral region. The signal was detected with two avalanche photodiodes (APD) in combination with band pass filters (BP). For full spectroscopic information a spectrometer equipped with a CCD camera was available by flipping in the mirror FM. Figure taken from [23]

The commercial microscope body (*Nikon*, TE2000) was modified to a scanning laser microscope. For scanning the sample it was equipped with a piezo scan stage (*Physik Instrumente PI*, P-517.3) offering a scan range of 100 µm × 100 µm × 20 µm with sub-nanometer resolution in x-, y- and z-direction. Image acquisition was controlled by a surface probe microscopy (SPM) controller (*RHK Technologies*, SPM 1000).

A non-polarizing beam splitter (BS, 50 % transmission, 50 % reflection at 633 nm) reflected the laser onto the objective (*Nikon*, CFI Apo TIRF 60X Oil, NA = 1.49, working distance 0.12 mm, infinity corrected) focusing the beam onto the sample. The backscattered light was collected by the same objective, transmitted through the beamsplitter exiting the microscope at the side port.

The detection path consisted of a Raman edge (RE) filter blocking the reflected laser light. The signal was split into two channels by a dichroic beam splitter (BS). Using band pass filters (BP) the signal was spectrally filtered before being detected by two avalanche photodiodes (APD, *Perkin Elmer*, SPCM-AQR Series). For Raman imaging typically the Raman G-band was recorded occurring at a Raman shift of about 1600 cm^{-1} corresponding to wavelengths of 704 nm, 561 nm, 625 nm for excitation wavelengths of 632.8 nm, 514.5 nm, 568.2 nm, respectively. Therefore, band pass filters centered around the cor-

responding wavelengths were used in the detection path. The dichroic beam splitter had a cut-off wavelength of 760 nm. Therefore, Raman signals of SWCNTs that were in the visible wavelength region were detected by the first APD.
Alternatively, full spectra could be taken with a spectrometer (*Andor*, Shamrock 303i) and a charge-coupled device (CCD) camera (*Andor*, iDus DU420-BR-DD) using a flip mirror (FM).
It has to be mentioned that the microscope configuration used was not truly confocal due to the missing pinhole in the detection path. Instead, the detector itself (diameter of sensitive area $\approx 175\,\mu m$) acted as a large pinhole. However, since the width of the excitation point spread function was much smaller than the detection point spread function, the spatial resolution of the system for Raman imaging was determined by the excitation point spread function [127] and corresponded therefore to about half of the excitation wavelength used.

Electrical measurements on the SWCNT devices were performed by contacting the electrode pads shown in Fig. 4.3 and Fig. 4.4 with two tungsten needles (diameter 5 µm). The needles were held by two probe holders mounted on micromanipulators enabling precise positioning of the needles. Applying a bias voltage to the device and measuring the electrical current was done using a sourcemeter (*Keithley Instruments*, Model 2400). Electrical measurements were used to identify the contacted SWCNTs on the substrate. I-V-curves were recorded using the free program *LabTracer* provided by *Keithley*.

For **photocurrent measurements** the focused laser beam was raster scanned across a contacted SWCNT and the generated photocurrent was recorded at the same time. This technique is called scanning photocurrent microscopy (SPCM). Since the photocurrent signal was weak (nanoampere) compared to the noise level it required preamplification with a current-to-voltage amplifier (*Femto*, DLPCA-200) combined with a lock-in detector (*Stanford Research Systems*, SR 830). A schematic is shown in Fig. 4.7 a).
Typical amplification factors of the current-to-voltage amplifier were 10^6 or 10^7 V/A. The output voltage was connected to the lock-in amplifier. Signal modulation was achieved with a chopper (*Thorlabs*, MC2000, Blade MC1F10) in the excitation beam path at the focus position of the first lens pair. The maximum modulation frequency with this blade was 1 kHz. Typically, a modulation frequency of 800 Hz was used. A reference signal with the same frequency was connected to the lock-in detector acting as a very narrow band pass filter centered at the modulation frequency. The filtering occured by multiplying the reference signal with the amplified photocurrent signal (in V) resulting in a DC component for equal reference and signal frequency and in AC components for other frequencies. The DC component was filtered out by using a low pass filter (RC type). The bandwidth of this filter was set by adjusting the time constant. Increasing the time constant yielded in a more stable and reliable measurement, since a RC filter takes five time constants to settle to its final value. A large time constant, however, led to long measurement times.

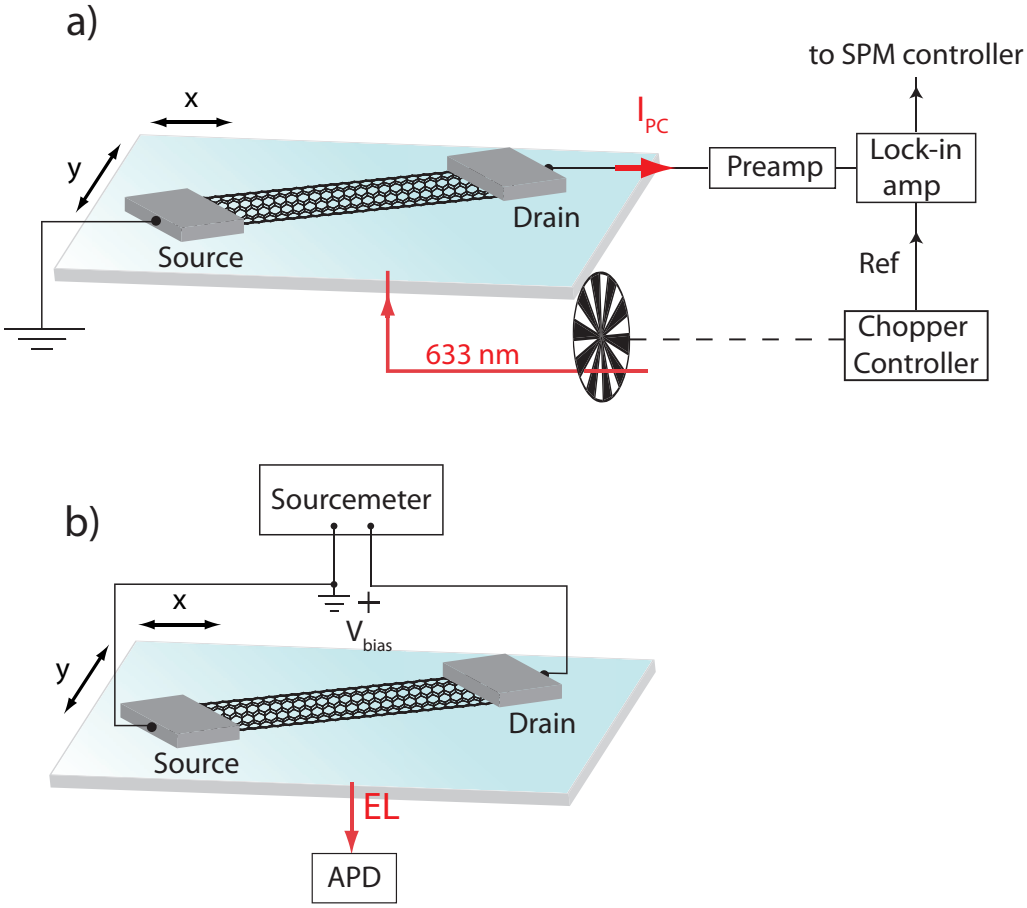

Fig. 4.7. Schematic of the setup used for optoelectronic measurements. a) Configuration for photocurrent measurements. A laser beam was focused onto the scanning sample. The generated photocurrent was preamplified by a current-to-voltage amplifier and detected by a lock-in detector. A chopper in the excitation beam path modulated the signal. The photocurrent was then recorded simultaneously with the the optical signal by the SPM controller. b) Configuration for the electroluminescence measurements. The excitation light was switched off and a bias voltage was applied to the device with a sourcemeter. The emitted electroluminescence was recorded by an APD.

For the same reason, the scan parameters of the image acquisition (scan speed, pixel size) had to be chosen such that the pixel dwell time is long enough. A standard value for the time constant of 10 ms was used and the scan parameters were set accordingly. The lock-in detector was connected to the SPM 1000 and photocurrent signal was recored simultaneously with the optical signal.

Electroluminescence measurements were performed by switching off the excitation light and applying a bias of several volts for electrical excitation (see Fig. 4.7 b)) using the Keithley 2400. Typically the bias voltage was between 5 and 15 V. Since the electroluminescence emitted by SWCNTs mainly appeared in the near-infrared (> 800 nm) the second APD or the spectrometer were used for detection without any additional filter. In contrast to Raman and photocurrent measurements, the spatial width of the electroluminescence signal was determined by the detection point spread function leading to a worse

spatial resolution of about 1-2 µm that reflected the effective size of the detector. Since the spectral range of the electroluminescence emission was broad, the wavelength dependent transmission and sensitivity of the optical elements (objective, beam splitter, gratings) and the detector (CCD camera) had to be taken into account. Therefore a correction curve was determined using a calibration lamp with known spectral emission. Every recorded electroluminescence spectrum was then corrected by this curve.
The durability of the devices during the electroluminescence measurement was limited due to the applied bias of several volts. This is a known problem and can be explained by electrical breakthrough at the regions of the largest voltage drop due to increased Joule heating leading to oxidation of the SWCNTs. Measures taken to prevent this failure, e. g. creating an Argon atmosphere or applying an ac-voltage instead of a dc-voltage to reduce the average dissipated power, did not show any significant improvement. Therefore, in general, the measurement times must be kept as short as possible e. g. by reducing the pixel number and increasing the scan speed. The short lifetime of the devices made systematic investigation of individual devices and antenna-enhanced measurements that were connected to long acquisition times challenging. Electroluminescence measurements were possible only for devices based on the long CVD grown SWCNTs, which turned out to be more durable. Photocurrent measurements at zero bias voltage, however, were performed using devices based on any SWCNT material.

4.2.2. Tip-enhanced near-field optical microscope-setup

Antenna-enhanced Raman, photocurrent as well as electroluminescence measurements can be performed by equipping the confocal setup with a distance control mechanism that enables the scanning of an optical antenna in close proximity to the sample surface. The distance control used a tuning fork shear force feedback system. The optical antennas were fabricated by electrochemical etching of a solid gold wire resulting in sharp gold tips. In addition to the confocal setup, a mode conversion of the laser beam was favorable. These three additional features are described in the following.

Tuning fork shear force distance control

The probe in any scanning probe microscope must be kept at small and constant distance to the sample surface requiring an active feedback mechanism that exploits some short-ranged interaction between sample and surface. In scanning tunneling microscopy (STM) the interaction is a tunneling current between tip and the sample. Atomic force microscopy (AFM) is based on the repulsive contact- or attractive van der Waals-forces between cantilever tip and sample. In both methods, the interaction used for the feedback is also the physical quantity of interest. Using the optical near-field itself in near-field optical microscopy, however, is not practicable. Using a tunneling current, as in STM, requires conductive samples and is therefore too restrictive. The forces involved in contact or tapping mode AFM are too large for a ductile gold tip and result in tip damage. A

distance control mechanism involving small oscillation amplitudes (few nanometer) and therefore small interaction forces (piconewton) is provided by the tuning fork shear force distance control mechanism that is based on the following principle: A tip attached to a commercial quartz tuning fork oscillates with a small amplitude due to the high stiffness of the tuning fork. Due to the piezoelectric nature of quartz, the mechanical oscillation induces surface charges picked up by electrodes deposited onto the tuning fork surface. This leads to an alternating voltage with same frequency as the mechanical oscillation proportional to the oscillation amplitude. Upon approaching the sample, the oscillation amplitude (usually few nanometers) decreases. This decrease is caused by damping of the oscillation by weak shear forces whose nature is still under debate. The decreasing oscillation amplitude is connected to an increase of the resonance frequency. One can either use the amplitude or the resonance frequency shift as a feedback signal. Using the amplitude as feedback signal has the drawback of a large response time to perturbations of the system and therefore slow scan speeds. Therefore, usually the frequency shift is used as feedback signal offering shorter response times [122].

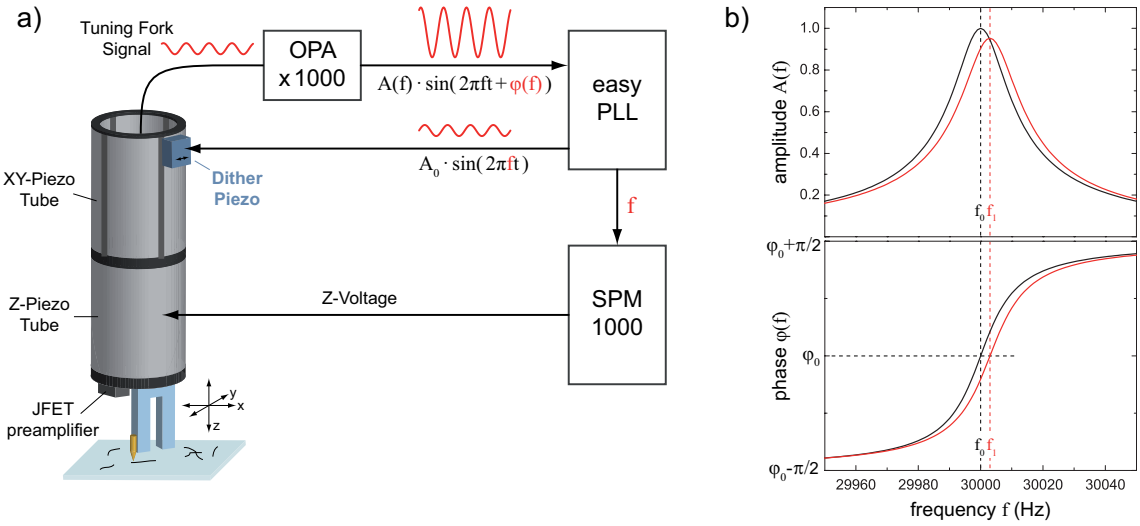

Fig. 4.8. a) Schematic of the shear force distance control system. The tuning fork was mechanically excited by a dither piezo at frequency f. The weak tuning fork signal was amplified by a junction field-effect transistor (JFET) and operational amplifiers and was detected by a phase-locked-loop (PLL). The PLL constantly measured the oscillation frequency f by adjusting the dither frequency such that the phase was kept constant at ϕ_0. The frequency f was then handed over to the SPM controller that regulated the voltage to the z-piezo to keep $f_1 - f_0$ constant. b) Amplitude and phase of the tuning fork oscillation as a function of the frequency. Black and red curves correspond to an oscillation without and with sample interaction. Upon approaching the sample the resonance frequency shifts by $f_1 - f_0$. The phase at resonance stays constant at ϕ_0. Figure taken from [23].

The schematic of the feedback loop used for the shear force distance control is shown in Fig. 4.8 a). Far away from the sample, the tuning fork oscillates at its resonance frequency of 32 678 Hz (2^{15} Hz) mechanically driven by a dither piezo. Glueing a tip onto one prong changed its resonance frequency by about 1 kHz, depending on the mass of tip

and glue. The weak signal was preamplified by a junction field-effect transistor (JFET) followed by a second amplification stage consisting of operational amplifiers. As can be seen in Fig. 4.8 b), by approaching the sample the resonance frequency shifts from f_0 to a higher frequency f_1 due to the damping caused by the shear forces. The phase shifts only in frequency and has the same value of ϕ_0 at resonance. While scanning over a topographic surface, the system maintained a constant frequency shift of about $f_1 - f_0 \approx 1 - 1.6\,\mathrm{Hz}$, the so-called setpoint, corresponding to a few nanometer distance to the sample. Therefore, the actual resonance frequency had to be constantly monitored. This is done by detecting the amplified tuning fork signal with a phase-locked-loop system (*nanoSurf*, easy PLL plus). The phase-locked-loop adjusted the dither frequency such that the phase was kept constant at ϕ_0. This ensured that the tuning fork was dithered always at its resonance frequency. This frequency was then handed over to the SPM 1000 controller. The SPM 1000 changed the voltage to the z-piezo such that the frequency shift matched the set-point value. The z-voltage was recorded during the scan as a topography signal using a calibration factor that depended on the z-piezo tube used (*EBL Products, Inc.*, EBL#3). Besides regulating the z-voltage and the voltages to the piezo scan stage, the SPM 1000 also provided the dc voltages for the x- and y-piezo in order to move the gold tip for precise positioning in the focus.

Antenna-enhanced optical and optoelectronic imaging

In order to perform antenna-enhanced Raman and optoelectronic imaging the confocal configurations for photocurrent and electroluminescence measurements, shown in Fig. 4.7, were combined with the described shear force distance control mechanism using an etched gold wire tip as a probe.

Therefore, the gold tip had to be centered in the laser focus to make sure that the tip apex is confocal with the detection focus. Furthermore, in the case of Raman and photocurrent measurements only a gold tip centered in the laser focus led to strong enhanced electric fields at the tip apex. This was achieved by recording the signal of the emitted gold photoluminescence with the APD. By changing the voltages to the x- and y-piezo (see Fig. 4.8 a)), the tip was slowly moved in the focus resulting in maximum signal for the center position. The tip then acted as optical antenna enhancing excitation, emission or both according to the antenna-enhanced schemes shown in Fig. 3.5.
Improved excitation enhancement was achieved by inserting a mode converter (MC) in the excitation beam path (see Fig. 4.6). The mode converter converted the incoming linearly polarized Gaussian beam to a radially polarized doughnut mode. Focusing this mode with a high NA objective resulted in a strong electric field component in the direction of propagation parallel to the tip axis. This polarization led to a large surface charge density at the apex causing stronger field enhancements. More details on the mode conversion can be found elsewhere [23, 122]. While the sample was scanned at slow scan speeds (about

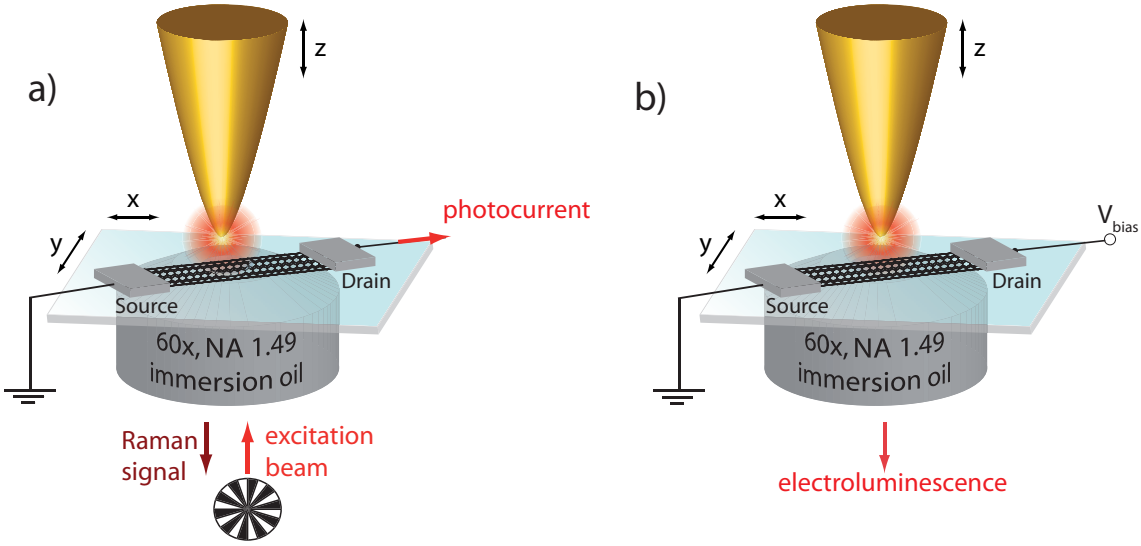

Fig. 4.9. Schematic of the setup for antenna-enhanced optoelectronic measurements. For both types of measurements a) and b) a sharp gold tip acting as optical antenna was kept at fixed position in close proximity to the scanning sample surface enhancing excitation and/or emission rates. Optical, optoelectronic and topographic signals were recorded simultaneously. For all measurements the gold tip had to be centered in the laser focus to ensure that the tip apex was confocal with the detection volume.

0.5 µm/s), the gold tip was kept fixed in the laser focus. Piezo drift, however, made long acquisition times very challenging. In photocurrent measurements one therefore had to compromise on the time constant of the lock-amplifier (see Sec. 4.2.1). The area of an antenna-enhanced scan was typically $1 \times 1\,\mu m^2$ with a pixel number per line of 128, leading to a pixel size of about 8 nm. Attention was paid to avoit scanning over the electrodes, since the feedback was optimized for topographic features of few nanometers (such as a SWCNT) leading to tip damage for much higher features.

An example for antenna-enhanced Raman and photocurrent imaging is given in Fig. 4.10. The upper two images a) and b) are simultaneously taken confocal Raman and photocurrent images. The Raman signal of the SWCNT is marked with the white arrow. The two electrodes appear bright in the optical image. Broad photocurrent signals of opposite sign are recorded close to the electrodes. In the antenna-enhanced configuration, only the region between the electrodes shown as an orange rectangle is scanned in order to avoid tip damaging. As a result, sub-diffraction Raman and photocurrent images are obtained as can be seen in Fig. 4.10 c) and d). The high spatial resolution allows to resolve many more details of both Raman and photocurrent signal that cannot be seen in the confocal images (Fig. 4.10 a) and d)). The interruption of the near-field Raman signal in the middle of the channel is due to the presence of a particle that is evident in the topography image (image not shown) and increases significantly the tip-SWCNT distance. Upon closer inspection, the photocurrent signal does not come from the SWCNT showing a strong Raman scattering intensity, but from a SWCNT lying next to the other one. The photo-

current signal shows sub-diffraction modulations that cannot be resolved in the confocal image Fig. 4.10 a).

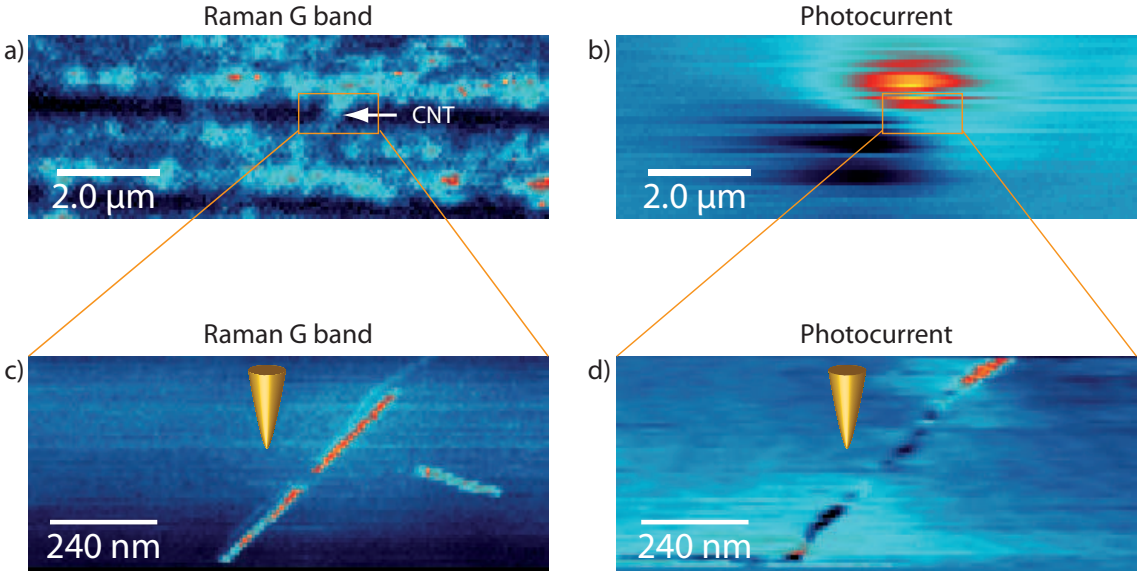

Fig. 4.10. Simultaneous antenna-enhanced Raman and photocurrent imaging. a) and b) Confocal Raman and photocurrent image. The Raman G band signature of the SWCNT is marked with the white arrow. c) and d) Antenna-enhanced Raman and photocurrent images recorded in the region defined by the orange rectangle. Besides the confocal background, strongly enhanced narrow Raman and photocurrent signals are detected. Due to the sub-diffraction resolution, many more details can be resolved compared to the confocal images shown in a) and b).

4.2.3. Gold tip fabrication

Sharp gold tips were fabricated by electrochemical etching of a solid gold wire (diameter 100 µm, *Chempur*, purity 99.995 %) in hydrochloric acid (37 %). A schematic is shown in Fig. 4.11 a).

The gold wire, used as anode, was dipped into a cuvette filled with hydrochloric acid. A platinum ring below the gold wire was used as cathode. By applying electrical pulses (positive pulses with a duration of 50 µs, repetition rate of 3 kHz and amplitude without load of 4 V) generated by a function generator (*BK Precision*, 4003A) the gold was oxidized at the anode via the following main reaction

$$Au + 4Cl^- \rightarrow AuCl_4^- + 3e^-$$

The formation of chloroaurate complexes decreased the diameter of the wire. However, the negatively charged reaction products feel attracted to the positive potential of the anode and hindered the reaction by blocking the access of chlorine ions. Therefore, a manual on/off switch was introduced in the setup to support the supply of chlorine ions at the gold surface. At the cathode H^+ was reduced to H_2 leading to gas production (bubbling) at the platinum ring.

The etching process was monitored with an optical microscope, providing a magnification

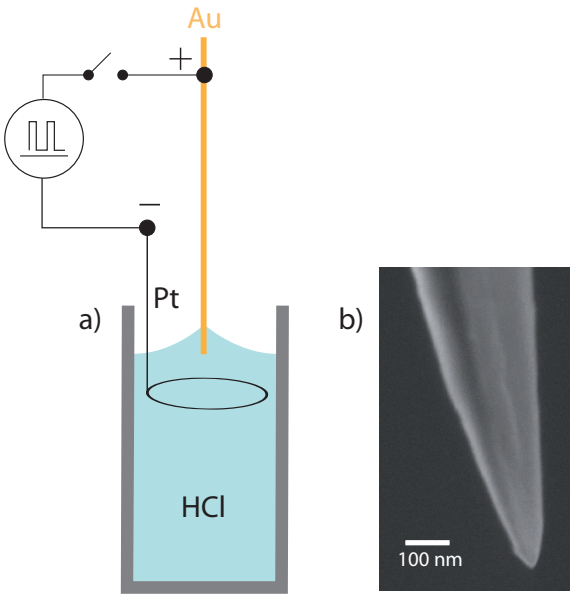

Fig. 4.11. a) Schematic of the setup for electrochemical etching of sharp gold tips. Electrical pulses were applied between a gold wire (anode) and a platinum ring (cathode) in hydrochloric acid. Oxidized gold ions forming complexes with chlorine ions led to a decrease of the wire diameter at the meniscus. b) SEM image of a gold tip with a diameter of about 15 nm.

of 80 in order to prevent overetching resulting in blunt tips. The tips were then rinsed carefully in distilled water. They were checked in a scanning electron microscope (SEM) to sort out bent, dirty or blunt tips. Using this etching method, sharp gold tips with diameters down to 15 nm were able to be reproducibly fabricated. An example of a SEM image of a tip with a diameter of about 15 nm is shown in Fig. 4.11 b).

5. Antenna-enhanced photocurrent microscopy of carbon nanotube devices

This chapter is based on the publication "Antenna-Enhanced Photocurrent Microscopy on Single-Walled Carbon Nanotubes at 30 nm Resolution" by Nina Rauhut, Michael Engel, Mathias Steiner, Ralph Krupke, Phaedon Avouris and Achim Hartschuh, *ACS Nano*, **6**, 6416-6421 (2012).

Confocal scanning photocurrent microscopy (SPCM) is a common tool to investigate the properties of nanoelectronic devices based on 1D or 2D nanostructures such as carbon nanotubes [80,88,89], inorganic nanowires [92] or graphene [94,128], as discussed in Sec. 2.2. It provides valuable information on different sources of built-in electric fields including internal pn-junctions [90], local defects [87] and nanostructure-metal interfaces [80, 81, 88, 89]. The latter are part of virtually all nanoscale devices and govern their overall performance [48, 60, 78]. At the metal contacts the current signal at zero bias is known to have at least two contributions. One results from the photovoltaic effect, i. e. the separation of the photoexcited charge carriers caused by a local built-in electric field. This electric field exists at the contact regions due to the formation of energy barriers and could also occur along the nanostructure caused by sample heterogeneities or external perturbations. Besides the photovoltaic contribution, there is evidence of an additional contribution to the zero bias current signal which stems from the illumination of the electrodes near the contact region [101, 103, 107]. This contribution is due to laser heating of one of the electrodes and can be thermoelectric in origin or caused by thermo-assisted tunneling of charge carriers through the energy barrier.
Up to now, nearly all SPCM measurements reported so far have been restricted to a spatial resolution of few hundred nanometers due to the diffraction limited size of the laser focus, making it impossible to optically characterize a device on the nanoscale. Therefore, the photothermal processes at the electrodes and the photovoltaic effect mentioned above could not be separately imaged in the past, since illumination of the band bending region at the contacts goes hand in hand with illumination of the electrodes due to the lack of sufficient spatial resolution. In addition, photovoltaic contributions originating from sub-diffraction potential variations along the SWCNT could not be detected due to spatial averaging.

There are only few near-field photocurrent studies on nanoelectronic devices reported so far [94,129]. In both studies an aperture probe was used and the spatial resolution achieved was about 100-200 nm. In this chapter antenna-enhanced scanning photocurrent microscopy is presented, based on a scanning optical antenna instead of an aperture probe, yielding a spatial resolution better than 30 nm. The principles of this technique were introduced in Chap. 3. In the first part, confocal SPCM measurements of carbon nanotube based devices are presented. On their basis, the powerfulness of the technique for the characterization of carbon based optoelectronic devices is depicted. The role of contacts and the contribution of non-photovoltaic effects to the photocurrent are addressed. Furthermore, the limitations of this confocal technique at very small length scales are pointed out. In the second part, these limitations are overcome by combining SPCM with the optical antenna concept. Antenna-enhanced photocurrent measurements with sub 30 spatial resolution were achieved revealing optoelectronic phenomena that remained hidden in confocal SPCM.

5.1. Confocal zero bias photocurrent measurements

In the following, confocal optical and photocurrent images of SWCNT devices fabricated according to the procedure in Sec. 4.1 are presented. The images have been recorded using the confocal scanning photocurrent microscope described in Sec. 4.2.1.
Typical photocurrent and optical images of two different SWCNT sample materials (CVD grown SWCNTs on quartz and IsoNanotubes-M^{TM}) are presented in Fig. 5.1. In Fig. 5.1 a) and b) a zero-bias photocurrent and an optical image of a device fabricated with a short metallic IsoNanotubes-M^{TM} as channel using electron beam lithography are shown. At zero bias, in case of the photovoltaic effect, the recorded photocurrent maps the local intrinsic fields present along the SWCNT.
The white dashed lines indicate the position of the electrodes. The electrode separation is 750 nm. Photocurrent signals of opposite sign appear at the CNT-metal contacts. The SWCNT can be identified in the optical image by its Raman G-band signature (marked by the white arrow). The bright spots on the electrodes come from residues of the photoresist used for the electron beam lithography. As mentioned before (Sec. 2.2), CNT-based optoelectronic devices are expected to show photocurrent signals upon asymmetric illumination of the two CNT-metal interfaces. These signals can be generated by the separation of optically excited electron-hole pairs in the local electric fields at the contacts at zero bias voltage (photovoltaic effect) and/or by laser heating of one of the contacts (photothermal effect). Electric fields at the contacts are caused by charge transfer between the electrode material and the CNT due to a difference in the work functions of the two materials. For semiconducting SWCNTs these interfaces are Schottky contacts. For metallic SWCNT devices as shown in Fig. 5.1 a) the appearance of these potential barriers is rather surprising but has been observed before [81]. A possible explanation is the inherently different

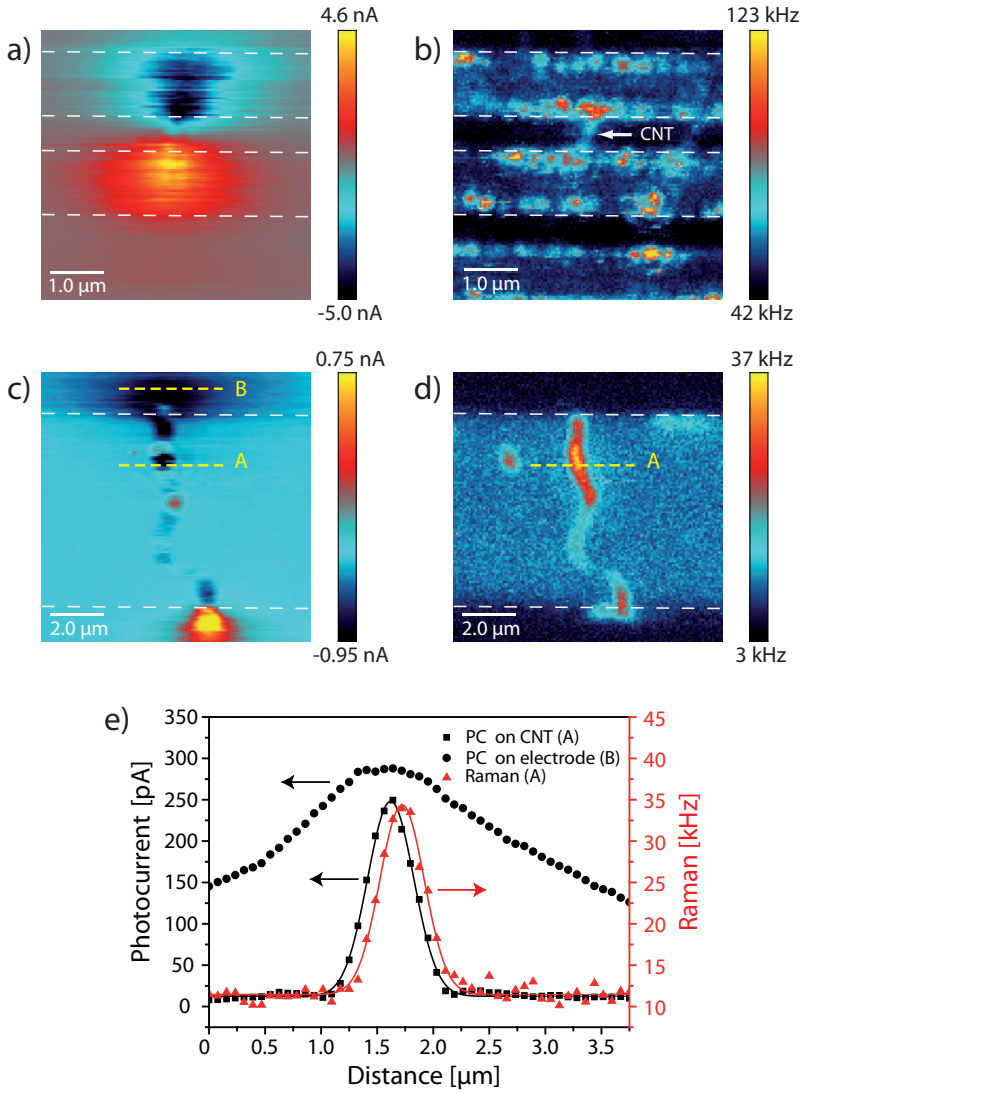

Fig. 5.1. Confocal zero bias photocurrent and optical images. a) Zero bias photocurrent image of a short metallic SWCNT (IsoNanotubes-M^{TM}). Two photocurrent signals of opposite sign appear at the contacts. b) Simultaneously taken optical image recorded with a band pass filter centered at the wavelength of the Raman G band of a CNT. The white arrow marks the Raman signature of the SWCNT. c) Zero-bias photocurrent image of longer CVD grown SWCNTs. In addition to the signals at the contacts photocurrent fluctuations along the SWCNT channel exist. d) Simultaneously taken optical image. The Raman signal indicates that the channel consists of more than one SWCNT. Strong Raman scattering correlates with strong photocurrent due to increased absorption. The position of the electrodes is marked by the white dashed lines. e) Cross-sections taken along the yellow dashed lines A and B in c) and d) together with a Gaussian fit. The spatial width of the photocurrent cross section taken at the electrodes at position A is much larger than far away from the contact at position B indicating a second thermoelectric contribution to the photocurrent. The spatial shift between the Raman and photocurrent signal comes from a delayed response of the lock-in detector caused by a large time constant.

3D-1D interface compared to a 3D-3D interface [82, 83].

In addition to the metal contacts, zero-bias photocurrents can also occur along the CNT channel. Fig. 5.1 c) and d) show the zero bias photocurrent and simultaneously recorded

optical image of CNT device with a larger electrode separation bridged by SWCNTs. For this device fabrication, the CVD grown SWCNTs on quarz were contacted using optical lithography (see Sec. 4.1). The photocurrent image reveals fluctuations connected to a frequent change of sign of photocurrent signal indicating that the energy bands of the SWCNT are not flat. They can be modulated by internal electric fields caused by structural defects [81, 87], CNT cross-junctions [91] and p-n junctions [69]. Such photocurrent variations along the channel are not observed for devices with a short channel length as in Fig. 5.1 a) due to spatial averaging caused by the diffraction limited resolution. The Raman image Fig. 5.1 d) shows regions of stronger and weaker Raman G-band intensities indicating that the channel does not consist of a single SWCNT. It is made of at least three crossing SWCNTs of different chiralities and different Raman absorption cross sections due to different degrees of resonance with the incident photon energy (see Sec. 2.1.2). Regions of strong Raman intensity spatially correspond to regions of strong (absolute) photocurrent due to increased absorption.

Whereas the photocurrent fluctuations along the CNT channel can be attributed to the photovoltaic effect only, the photocurrent signals at the metal contacts must have two contributions as can be derived from Fig. 5.1 c). The photocurrent signal at the contacts appears much broader than along the SWCNT. Fig. 5.1 e) shows the cross sections extracted along the yellow dashed lines in Fig. 5.1 c) and d) visualising this issue. The spatial width of the photocurrent signal far away from the electrodes obtained by fitting a Gaussian curve (w_{PC}=291 nm ± 3 nm) is close to the width of the Raman signal (w_R =279 nm ± 7 nm) and corresponds to the spatial resolution of the optical setup given by approximately half of the excitation wavelength. The photocurrent signal at the electrodes, however, shows a much larger spatial width (> 1 µm). This large difference suggests that the photocurrent at the contacts is not caused by the band bending alone but also by the photothermal effect coming from asymmetric heating of the two contacts . Also other effects like thermal-assisted tunneling through the energy barrier and excitation of electrons through photon absorption in the electrode material can play a role (see Sec. 2.2).
Another demonstration of the photothermal effect at the contacts is given in Fig. 5.2. Fig. 5.2 a) and b) show the photocurrent, Raman image of another third device using a metallic CheapTube as channel. The SWCNT is marked by the white arrow in the optical image. Due to the special geometric configuration - the SWCNT connects the end of the upper electrode with the lower electrode - the effect of illuminating the electrodes is directly seen by the asymmetric photocurrent distribution following the shape of the electrode. In addition, by inserting a polarizer in the excitation path, polarization dependent Raman and photocurrent measurements were performed on this device. Whereas the Raman signal shows a degree of polarization of about 0.5 with maximum intensity for a polarization along the orientation of the CNT, the photocurrent at the CNT-metal contact shows a degree of polarization of only 0.25. The degree of polarization is defined as $\frac{I_{max}-I_{min}}{I_{max}+I_{min}}$, where I_{max} and I_{min} is the maximum and minimum signal. The strong po-

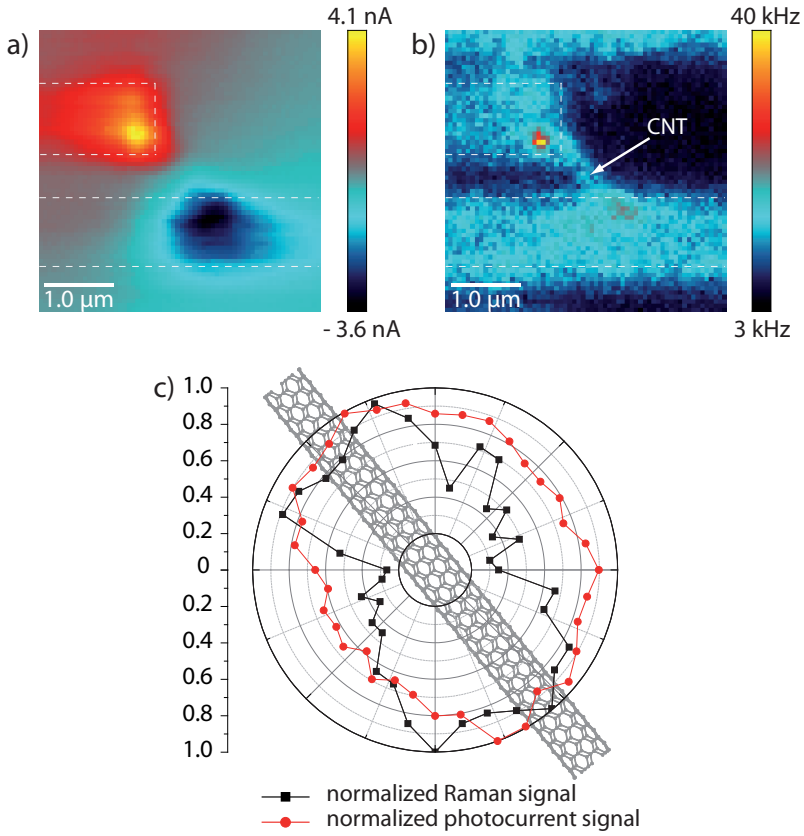

Fig. 5.2. Demonstration of the thermoelectric effect. a) Photocurrent image of a third device based on a metallic CheapTube. The asymmetric spatial photocurrent distribution following the shape of the electrode demonstrates the existence of a thermoelectric contribution. b) Simultaneously taken optical image recorded with a band pass filter centered at the wavelength of the Raman G band of a CNT. The Raman signature of the SWCNT is marked with a white arrow. c) Polarization dependent measurement of the photocurrent at the contacts and the Raman signal. Both signals show strongest signal for a polarization along the SWCNT axis. The Raman signal shows a larger degree of polarization of about 0.25 compared to 0.5 for the photocurrent. This indicates the existence of a polarization independent contribution that is assumed to be thermoelectric.

larization dependence of the Raman signal is due to the polarization dependent absorption as explained in Sec. 2.1.2. A similar degree of polarization is therefore expected for the photocurrent signal. The fact that the degree of polarization is smaller can be attributed to the thermoelectric contribution that is assumed to be polarization independent, because it is caused by absorption in the bulk metal.

Therefore, the two effects - thermoelectric and photovoltaic effect - both contribute to a varying degree to the photocurrent at the metal contacts of any CNT based device. Whereas the thermoelectric contribution exists at the interface only, the contribution coming from the band bending extends along the channel. However, the diffraction limited spatial resolution of a confocal scanning photocurrent microscope is not sufficient to image both contributions separately.

5.2. Antenna-enhanced photocurrent imaging

As described in Sec. 2.2 confocal scanning photocurrent microscopy is a powerful tool to characterize carbon based optoelectronic devices. However, due to the size mismatch between the device and the wavelength of visible light, it reaches its limits at sub-diffraction dimensions, hindering a characterization of the device on nanoscale length dimensions. This section reports on the first photocurrent measurements along single carbon nanotube devices yielding a spatial resolution of about 30 nm. At the beginning, by comparing the simultaneously taken Raman and photocurrent signals, the difference in the signal enhancement mechanism for the two antenna schemes are pointed out according to the discussion in Sec. 3.5. Then, two applications of antenna-enhanced photocurrent microscopy for the sub-diffraction investigation of CNT devices are demonstrated. First, it is applied to image the band bending at the metal contacts separatly from the photothermal effect and to determine its spatial extension. Second, sub-diffraction potential modulations, that cannot be resolved with confocal techniques, are detected with antenna-enhanced SPCM. Simultaneously recorded Raman scattering images reveal the structural properties and the defect densities of the SWCNTs.

5.2.1. Photocurrent signal enhancement

The principle of antenna-enhanced photocurrent imaging is shown in Fig. 5.3. As described in Sec. 3.5, the Raman signal in known to scale approximately with the fourth power of the field enhancement factor f. This relation takes into account that both the excitation rate and the emission rate are enhanced by the square of f. The same enhancement factor f is used for both excitation and emission, since the shift between the excitation and emission wavelength is small in the case of Raman scattering.

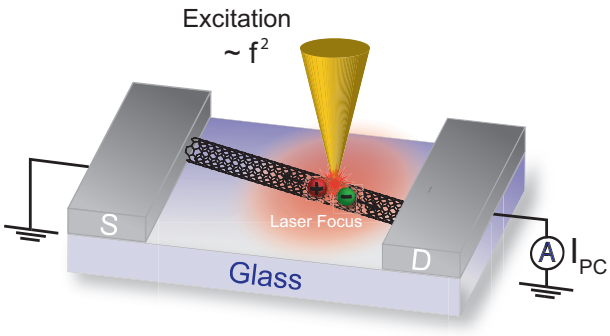

Fig. 5.3. Schematic of antenna-enhanced photocurrent microscopy. The optical antenna locally increases both excitation and emission rates each scaling with the square of the field enhancement factor f.

In the photovoltaic scheme only the excitation rate is enhanced. Therefore, an increased photocurrent proportional to the square of f is expected from theory (see Sec. 3.5). This assumption is confirmed experimentally in the following. Fig. 5.4 a) displays a confocal photocurrent image of a contacted carbon nanotube with an electrode separation of about 500 nm (device A) depicting two almost symmetric signals of opposite signs occurring at the source (S) and drain (D) electrode. These typical features of a diffraction-limited SPCM image can be understood considering the scheme shown in Fig. 2.8.

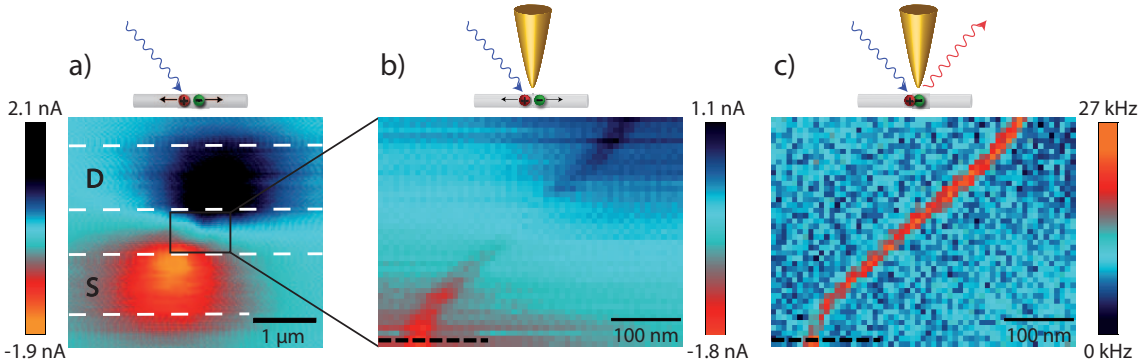

Fig. 5.4. Antenna-enhanced imaging of a single CNT device. a) Confocal photocurrent image of device A. The positions of source (S) and drain (D) electrodes are indicated by dashed white lines. b) and c) Antenna-enhanced photocurrent and Raman images obtained by scanning the black rectangular region in a). The Raman image represents the G-band intensity. The rather uniform Raman signal intensity indicates an almost constant antenna enhancement.

Antenna-enhanced photocurrent and Raman images of device A, presented in Fig. 5.4 b) and c), are obtained by scanning the sample with respect to a metal tip centered in the laser focus in close proximity. The photocurrent image in Fig. 5.4 b) shows two narrow sub-diffraction contributions of opposite sign extending from the electrode regions following the Raman signature of the carbon nanotube in Fig. 5.4 c). In scanning probe microscopy the width of the signal can be taken as the spatial resolution, which in general scales with the diameter of the probe. The width of the cross section w_{PC} taken along the black dashed line in the photocurrent image in Fig. 5.4 b) shown together with its corresponding Gaussian fit function in Fig. 5.5 a) demonstrates a spatial resolution of about 28 nm. Therefore, the enhanced photocurrent signal originates from a 28 nm long nanotube section located underneath the scanning tip. The width of the simultaneously recorded Raman signal w_R at the same position is about 19 nm (see Fig. 5.5 a)). The ratio between the linewidth of photocurrent and Raman signal of $w_{PC}/w_R = 28/19 = 1.47$ is approximately equal to $\sqrt{2}$ and is more or less constant along the whole SWCNT (see Fig. 5.5 b)) with a mean value of 1.49 and a standard deviation of 0.26. From theory a ratio of $\sqrt{2}$ is expected from the model depicted in Fig. 5.3 considering the enhancement mechanisms of optically and electrically detected signals as explained in Sec. 3.5.2. The antenna-enhanced fields cause increased excitation and, due to reciprocity, emission rates. The intensity of optically detected Raman scattering I_R hence scales with f^4. A factor of $\sqrt{2}$ for the ratio of the linewidths of the Gaussian cross sections suggests that $I_R \propto (I_{PC})^2$, because the square of a Gaussian function with linewidth w is again a Gaussian function with linewidth $\frac{w}{\sqrt{2}}$. This implies that the enhanced photocurrent signal scales with f^2. This is consistent with the fact that for the electrically detected photocurrent signal the enhancement only affects the excitation rate as discussed in Sec. 3.5. The small derivation of the theoretical value of $\sqrt{2}$ and the measured mean value of 1.49 ± 0.26 could be caused by an asymmetric tip shape exhibiting a non-Gaussian position dependence of the enhancement factor.

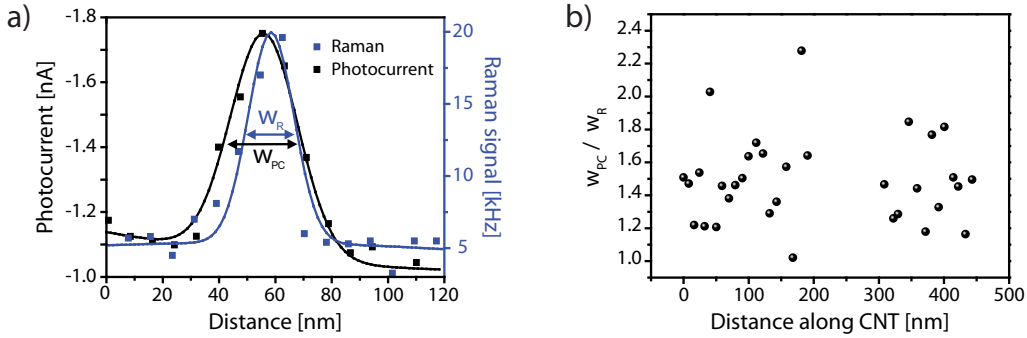

Fig. 5.5. a) Cross sections taken along the dashed black lines in Fig. 5.4 a) and b) together with their Gaussian fits. The spatial resolution of the photocurrent image taken as the full width at half maximum w_{PC} is about 28 nm. The value obtained from the Raman signal is $w_R = 19$ nm, about a factor of $1/\sqrt{2}$ smaller. b) Ratio between photocurrent and Raman linewidths determined along device A. The ratio w_{PC}/w_R observed in the figure is centered at a mean value of 1.49 with a standard deviation of 0.26, close to the predicted value of $\sqrt{2} = 1.41$.

5.2.2. Determination of the photo-carrier quantum efficiency

From the enhanced Raman and photocurrent signals the photo-carrier quantum efficiency can be estimated close to the contacts in the region of the band bending.
The quantum efficiency η defined as the ratio between the number of created carriers and absorbed photons can be calculated using the following equation

$$\eta = \frac{h\nu}{e}\frac{I_{PC}}{\alpha I_{NF}}. \tag{5.1}$$

Here, $h\nu$ denotes the photon energy, I_{PC} the enhanced photocurrent signal, α the absorption cross section (taken as $\alpha = 1.7 \times 10^{-17}\,\mathrm{cm}^2$ [130]) and I_{NF} the laser intensity at the position of the antenna amplified by the field enhancement factor f^2. From the experimental data, the enhancement factor f is determined to be approximately 3 using the enhancement of the Raman signal which is spatially uniform along the SWCNT. The near-field intensity I_{NF} therefore calculates as $I_{NF} = f^2 \cdot I_{FF}$, with $I_{FF} = \frac{I_L}{\pi r^2}$, where r=150 nm is the radius of the diffraction limited laser spot and $I_L \approx 1$ mW is the laser power at the sample position. However, I_{NF} is restricted to a CNT segement of about 20 nm, therefore the absorption cross section has to be calculated for a 20 nm long CNT segment. Estimating the number of carbon atoms for a (6,5) nanotube in a 20 nm long segment yields a number of about 1800. This is of course just a rough estimation because this value and also the absorption cross section will be different for the present, metallic SWCNT with unknown chirality. Taking a value for I_{PC} that is about 1 nA close to the contacts and inserting it together with all other parameters into Eqn. 5.1 yields a quantum efficiency on the order of

$$\eta \approx 10^{-3}.$$

There are only few values of quantum efficiencies of SWCNT devices reported in literature. Freitag et *al.* determined a higher quantum efficiency of 10^{-1} [7]. However, this device was biased and consisted of a semiconducting SWCNT. For the given metallic, unbiased device, the quantum efficiency is indeed expected to be lower.

5.2.3. Imaging of the band bending

All confocal photocurrent images of short SWCNTs show broad signals at the metal contacts caused by a photovoltaic and a photothermal effect. Due to the limited spatial resolution, the two contributions cannot be separately imaged (see Fig. 5.4 a)). However, this is possible with the high spatial resolution provided by antenna-enhanced photocurrent imaging as demonstrated in Fig. 5.4 b) showing enhanced photocurrent signals extending away from the electrode. In principle, local laser heating along the SWCNT followed by heat transport could lead to an asymmetric temperature increase at the electrodes resulting in an indirect photothermal contribution to the detected current. This contribution from a nanoscale CNT section is expected to be far smaller than what is observed upon direct confocal illumination of one of the macroscopic electrodes (see Fig. 5.4 a)). However, the experimental data for confocal and antenna-enhanced photocurrent signals are on the same order of magnitude, which indicates that local laser heating along the CNT is not the dominating process. Therefore, the photocurrent signal away from the contacts is attibuted to the band bending whose shape and spatial extension will be quantified in the following.
By performing Gaussian fits for each line in Fig. 5.4 b) the antenna-enhanced signal can be extracted from the background resulting from confocal far-field excitation of the CNT and the electrode region. The near-field amplitude along the nanotube is plotted in Fig. 5.6 a). Because the enhancement takes place within a nanotube section of about 30 nm at the position of the antenna at distances of up to few 100 nm away from the electrodes, the enhanced photocurrent signal cannot be due to laser-illumination of the electrode, but results from locally enhanced optical excitation of the CNT. Separation of the photoexcited charge carriers at zero bias requires a local built-in electric field that stems from band bending at the metal contacts extending into the CNT. Its decay length L is quantified in the following. As discussed in Sec. 2.2 for 1D nanostructures linear scaling between the photocurrent I_{PC} and the electric field expressed as the band gradient corresponding to

$$I_{PC} \propto -dE/dr$$

has been reported, where r denotes the position along the structure and E the energy of the electronic band. Integrating the photocurrent signal recorded along the CNT shown in Fig. 5.4 b), the band energy profile can be obtained. It is plotted together with the antenna-enhanced photocurrent signal in Fig. 5.6 a). The band profile can be well fitted by the sum of two exponential decay curves with equal decay length L and amplitude shown as red curve in Fig. 5.6 a). The fit function used is $F(r) = -A \cdot e^{-r/L} + A \cdot e^{(r-B)/L)} + A \cdot (1+$

$e^{-B/L}$), where r denotes the position along the CNT. The first term describes the decay at the left, and the second term the decay at the right contact, respectively. The last term is a constant offset to set the band energy at the contacts to zero. The common decay length of the two single exponentials determined by the fit is $L = 517\,\text{nm} \pm 210\,\text{nm}$. The parameter $B = 525\,\text{nm} \pm 1\,\text{nm}$ is the channel length. The Raman spectrum of this SWCNT is shown in Fig. 5.7 a) and reveals a RBM at an energy of $190\,\text{cm}^{-1}$. Using the Kataura plot shown in Fig. 2.6 a) together with the excitation wavelength of 632.8 nm = 1.96 eV, indicates that the nanotube is metallic. An energy barrier is therefore surprising, because it is not expected for a metal-metal contact. However, its existence is confirmed by the antenna-enhanced measurement that decouples the photovoltaic from the thermoelectric contribution. Its origin presumably lies in the one-dimensionality of the SWCNT forming a 1D-3D contact instead of a 3D-3D contact. One explanation could be a less efficient screening caused by a reduced number of free electrons in a 1D compared to a bulk channel [83].

Fig. 5.6 a) indicates a downward bending of the band at the contacts. This is confirmed by $I-V$-curves recorded illuminating the CNT at either source or drain contact (Fig. 5.6 b)). From the dark curve it becomes evident that a positive current corresponds to an electron flow from source to drain. Illuminating the drain contact offsets the $I-V$-curve by a positive photocurrent I_{PC} implying that additional electrons flow onto the drain electrode. From this, it can be followed that a positive photocurrent corresponds to a downward band bending for this specific device.

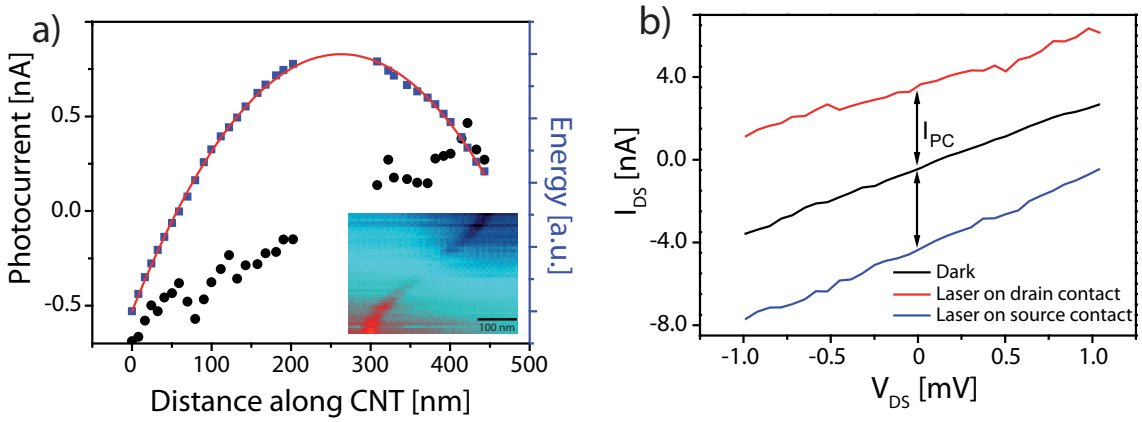

Fig. 5.6. Determination of the extension of band bending. a) Antenna-enhanced photocurrent signal along the CNT of device A (black round symbols). The missing data points in the middle correspond to the region where the enhanced signal was too weak to perform a Gaussian fit. The photocurrent signal integrated in space along the CNT reconstructs the band energy profile (blue square symbols) fitted by a sum of two exponential decay curves with opposite sign (red curve) resulting in a common decay length of L = 517 nm ± 210 nm. The large uncertainty is due to the superposition of symmetric band bending contributions from the two contacts with opposite sign that cancel in the middle of the CNT and does not reflect signal noise. b) Source-drain I-V curves recorded under confocal illumination of the nanotube at either source or drain electrode. The curves experience either a positive or negative offset I_{PC} indicating the direction of electron flow at the respective electrodes.

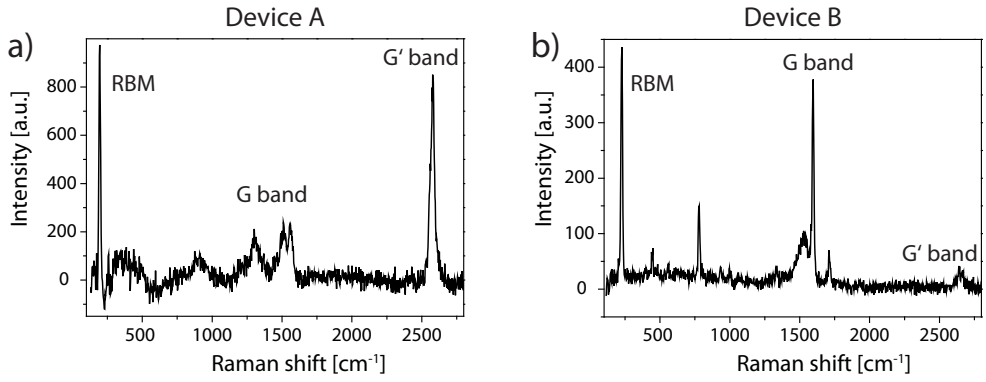

Fig. 5.7. Raman spectra of the studied devices. a) Raman spectrum of device A. b) Raman spectrum of device B. The Raman shifts of 190 cm^{-1} and 230 cm^{-1} of the RBM together with the laser excitation wavelength 632.8 nm used in the experiments reveal the metallic character of the nanotubes.

5.2.4. Imaging of sub-diffraction potential modulations

A second metallic device B with longer channel length ($\approx 1\,\mu m$) was investigated to study band energy fluctuations along a single nanotube. As for device A, the metallic character of the SWCNT was deduced from the Raman spectrum (see Fig. 5.7 b)). Fig. 5.8 b) and c) show the simultaneously recorded antenna-enhanced photocurrent and Raman G-band images. In contrast to device A, device B exhibits an additional change of sign of the photocurrent occurring in the middle of the device, approximately at the position of the dashed horizontal yellow line in Fig. 5.8 a)-c). This change of sign is again an indication that the photocurrent is not caused by an asymmetric temperature increase at the electrodes after local laser heating along the CNT and supports its assignment to charge separation by local built-in electric fields. The effect of direct confocal laser heating of the electrodes exists and is shown for device B in Fig. 5.2 a).

Integrating the photocurrent signal along the length of the nanotube reconstructs the band energy profile as discussed above and is shown in Fig. 5.8 d). The band features a linear offset, which can be attributed to charging of the substrate during the scanning process [87]. Fig. 5.8 e) shows the result after slope subtraction together with the topography profile along the SWCNT. The local minimum in the electronic band of the SWCNT at 570 nm coincides exactly with the position of a particle seen in the topography data in Fig. 5.8 a) and e).

The presented band energy profile therefore is a superposition of the contributions from the contacts and the modulations along the channel, making it unfeasible to quantify the decay length of the band bending at the contacts as it was done for device A. However, for both devices the decay happens on the same length scale. Remarkably, the photocurrent fluctuations cannot be detected in the confocal image shown in Fig. 5.2 a) due to spatial averaging (see Fig. 5.8 f)). Due to the large focus size, both the rising and the falling edge of the potential minimum are illuminated at the same time leading to positive and negative photocurrents canceling out each other. Upon closer inspection of the near-field

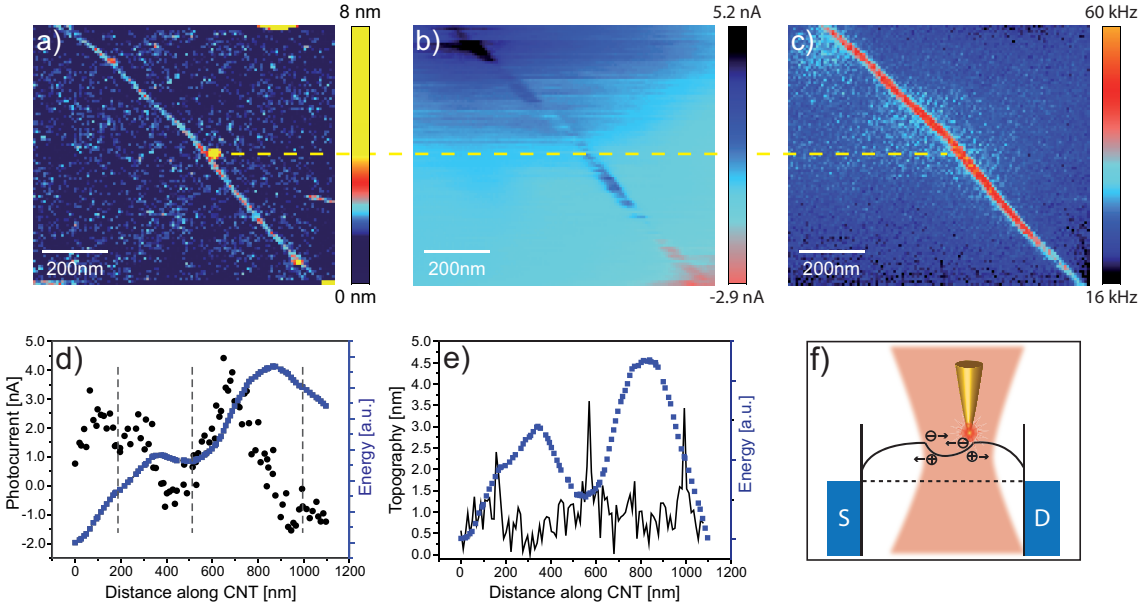

Fig. 5.8. Antenna-enhanced imaging of photocurrent fluctuations along a single SWCNT (device B). a) Topography image. The drain and source electrodes appear at the top and at the bottom of the image. b) and c) Antenna-enhanced photocurrent and Raman G-band image. The dashed yellow line marks the position of the central particle. d) Amplitude of fitted antenna-enhanced photocurrent signal along the SWCNT (black round symbols). The integrated photocurrent signal (blue square symbols) reconstructs the shape of the band potential. e) Integrated photocurrent signal from d) after a slope subtraction (blue symbols). The local minimum and kinks in the band energy profile seen in d) and e) coincide with the locations of particles seen as peaks in the topography data (black curve in e)). These are marked in d) by dashed vertical lines. f) Schematic band diagram. The local minimum cannot be resolved with a diffraction limited laser spot due to spatial averaging of photocurrent signals with opposite signs.

data, two less pronounced photocurrent signatures at 150 nm and 1000 nm can also be correlated with particles occurring in topography (compare Fig. 5.8 d) and e)). Based on this spatial correlation, in the present case, the observed potential modulations are caused by charged particles rather than structural defects within the CNT as reported before [87]. Structural defects in SWCNTs can be studied by Raman spectroscopy leading to characteristic D-band scattering (see Sec. 2.1.2). This interpretation is supported by recording simultaneous high-resolution Raman spectroscopic and photocurrent images focusing on the region around the central particle. For this purpose, a full Raman spectrum is taken at each image pixel. The Raman intensity maps can then be obtained by integrating each band over the respective energy range. These images are presented in Fig. 5.9. Whereas the G band intensity is constant ensuring a constant signal enhancement, the D band map shows a varying D band intensity along the CNT indicating the presence of structural defects. However, no correlated increase of the photocurrent signal exists as observed in [87].

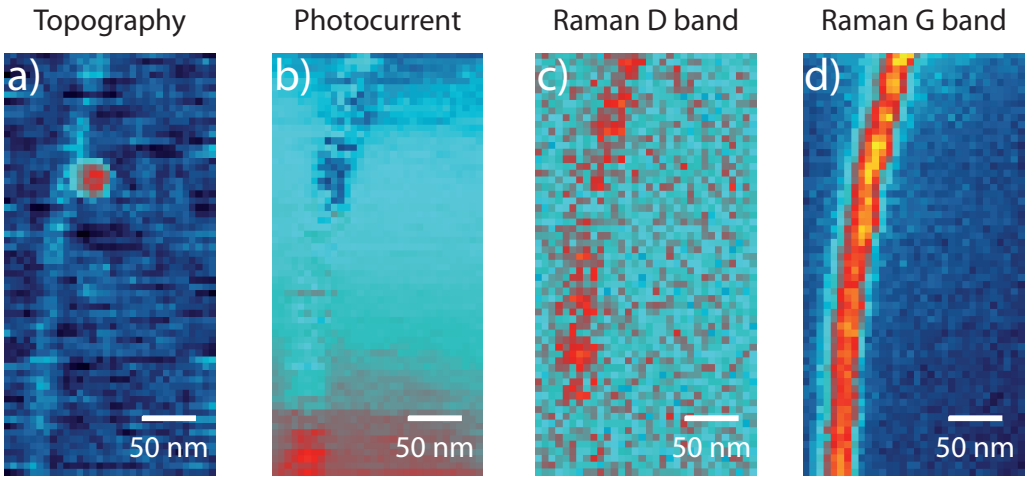

Fig. 5.9. High-resolution spectroscopic imaging of the central region of device B. a) Topography, b) photocurrent, c) Raman D band intensity and d) Raman G band intensity taken along device B containing the particle seen in the center of Fig. 5.8. A varying D band signal strength can be observed along the SWCNT, but without showing any correlation with the photocurrent signal. In this measurement, complete Raman spectra were taken at each image pixel. The Raman D and G band intensities were derived by integrating the respective spectral contribution.

5.3. Summary

In summary, this chapter presented antenna-enhanced scanning photocurrent microscopy that enabled the simultaneous recording of optical and photocurrent signals with nanoscale spatial resolution and improved detection sensitivity. While the limits of confocal SPCM were pointed out in the first part, the second part demonstrated high-resolution antenna-enhanced photocurrent measurements on two different devices. With the help of Raman spectroscopy, both involved SWCNTs were identified as metallic. The observed enhanced photocurrent signal was due to locally increased absorption. By comparing it to the simultaneously obtained Raman signal, a signal enhancement proportional to the square of the field enhancement factor as predicted by theory in Sec. 3.5 was experimentally confirmed.

Two applications of antenna-enhanced photocurrent microscopy were presented. First, the technique was used to study the decay length of the band bending at the contacts of a metallic SWCNT device. It was found that it can be well described by a sum of two exponential decay functions, one for each contact, with equal amplitudes and decay lengths. For this specific device a decay length of about 520 nm was determined.

For a second device, again a metallic SWCNT, local variations in the electronic structure along the SWCNT were probed. These modulation could not be detected by confocal microscopy due to spatial averaging of the photocurrent signal. The investigations were complemented by antenna-enhanced spectroscopic images that allows to create Raman maps for different Raman bands. The map of the Raman D band showed the presence of defects, but did not show any correlation with the photocurrent signal. Instead, the photocurrent signal correlated with the topography map, revealing a particle at position of

the signal change of the photocurrent. Therefore, the potential modulations were ascribed to charges associated with this particle rather than to structural defects.
Both investigated devices were based on metallic SWCNTs as channel. Antenna-enhanced SPCM can also be applied to semiconducting SWCNTs. However, because semiconducting SWCNTs exhibit exciton diffusion lenghts of about 100 nm [22], excitons can drift into the region of the local electric fields complicating the image contrast formation in antenna-enhanced photocurrent measurements. In principle, antenna-enhanced SPCM could be applied to any other 1D or 2D structure. It extends the available set of scanning probe techniques by combining high-resolution photovoltaic and optical probing.

6. Antenna-enhanced electroluminescence microscopy of carbon nanotube devices

This chapter is based on the publication "Antenna-Enhanced Optoelectronic Probing of Single-Walled Carbon Nanotubes" by Nina Mauser, Nicolai Hartmann, Matthias S. Hofmann, Julia Janik, Alexander Högele, Achim Hartschuh, *Nano Letters*, **14**, 3773-3778 (2014).

In the previous chapter, SWCNTs were employed in light detecting devices and their photovoltaic response was probed. As described in Sec. 2.2, SWCNTs can also be the basis for light emitting devices. In this configuration, they act as electrical-to-optical transducers, emitting electrically induced light. A variety of different SWCNT based light emitters has been suggested, incorporating suspended and non-suspended CNTs [9, 10, 108–110, 114, 116, 118, 119] or films [101, 131–133]. As in case of photocurrent, several mechanisms responsible for the electroluminescence (EL) are suggested in these reports, including recombination due to ambipolar transport, impact excitation, Joule heating and phonon-assisted decay (see Sec. 2.2). Depending on the device configuration, these mechanisms can contribute to the EL signal to a varying degree.
Exploiting the electric field enhancement associated with an optical antenna, the performance of any light emitting device can be improved. Up to date, only static antenna configurations have been realized for a variety of sample materials including OLEDs [134], and p-n junction devices [135, 136]. This chapter presents the first sub-diffraction electroluminescence images of a nano-electronic device, using a scanning optical antenna. It represents thus the implementation of the third antenna scheme depicted in Fig. 3.5 c). The powerfulness of this study lies in the combination of all three antenna schemes (Fig. 3.5 a) to c)) complemented by topographic information, allowing deep insights into the optoelectronic properties of CNT based nanoscale devices. In the first part, spatially resolved, resolution-limited EL measurements on a large number of devices are presented together with spectroscopic measurements. The second part focuses on the antenna-enhanced study of a particular CNT device with a spatial resolution of 40 nm. The high spatial resolution allowed for the determination of the size of the electroluminescence source, i. e. the length of the emitting CNT segment, for two different devices. By correlating the antenna-enhanced EL with photocurrent and topographic measurements, conclusions on the origin of the EL emission could be drawn.

6.1. Spatially and spectrally resolved electroluminescence measurements

The EL emission of a large number of devices was investigated by means of confocal electroluminescence imaging using the setup described in Sec. 4.2.1. Spatially as well as spectrally resolved measurements were performed. The studied SWCNTs were grown on a quartz substrate by chemical vapor deposition (see Sec. 4.1) and devices were fabricated with optical lithography. In contrast to photocurrent measurements, devices consisting of long SWCNTs were more favorable because of their longer durability under an applied voltage of a few volts as required for the EL measurements.

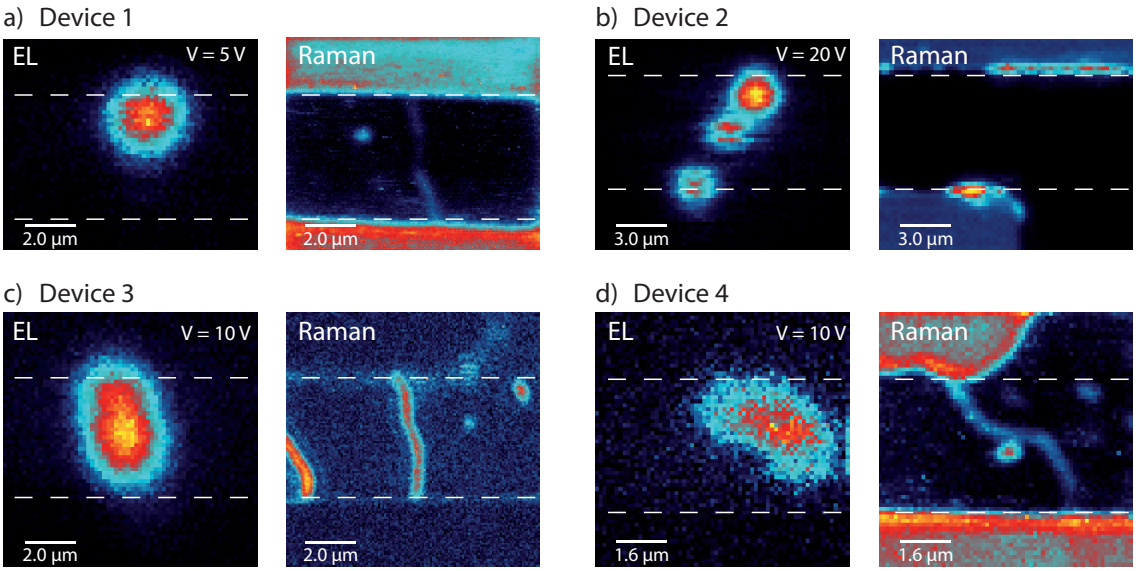

Fig. 6.1. Spatial EL intensity distribution for four different devices. The left image of each pair depicts the EL image, the right one the Raman image, taken for the same scan area. The Raman images were recorded with a band pass filter centered at 703 nm, imaging the Raman G band, whereas no filter was used for the EL measurements. The edges of the electrodes are indicated by white dashed lines. The EL intensity was located at the contacts (device 1 and 2), or along the CNT channel (device 2,3 and 4). Depending on device and bias voltage, the EL intensity appeared spot-like or had an elongated shape.

Confocal EL images were taken for a large number of devices, all in all about 50 devices were investigated. Four of them are represented in Fig. 6.1 together with optical images taken for the same scan area. The position of the electrodes could be identified from the Raman image, as well as the Raman G band signature of the involved SWCNT, except of for device 4 which did not show any Raman signal. These images visualize the EL position within the device. However, the spatial resolution achieved in the EL measurement was not as high as the resolution obtained in the Raman measurement due to the absence of a pin-hole in the detection path (see Sec. 4.2.1). Depending on the device, the EL intensity distribution appeared spot-like (device 1 and 2) or had an elongated shape (device 3 and 4). For a given device, the shape also strongly depended on the bias voltage as shown in Fig. 6.2. Increasing the bias voltage, lead to an increase of the nanotube segment

length from which EL was emitted resulting in a spatially more extended emission. The observation of an elongated EL intensity distribution required the length of the emitting CNT segment to be non-negigible compared to the spatial resolution. For most devices, the EL intensity was located at the contacts as shown for device 1. However, EL emission also occurred along the CNT as for device 2 to 4. In addition, for some devices, several distinguishable emission spots appeared (device 2). The position and bias dependance can be understood considering the mechanism behind the EL emission. As discussed in Sec. 2.2, in principle four mechanisms can contribute to the EL emission: recombination due to ambipolar transport, phonon-assisted decay, Joule heating or impact excitation. For the present device configuration, unipolar transport was expected. It is known that SWCNTs at ambient conditions without any gate behave as p-doped conductors [73]. Therefore, recombination due to ambipolar transport was unlikely to occur. Phonon-assisted decay from the M-point as observed in [119] could be excluded based on the spectral shape of the emission (see Sec. 6.2). Joule heating was expected to occur at position of highest temperature of a CNT, i. e. where the resistance was high. Therefore, EL emission due to Joule heating was expected to appear at the contacts or at positions of high resistance along the CNT. Impact excitation happens in regions of high, local electric fields. As for Joule heating, these exist either at the contacts, in the region of band bending, or along the CNT, and were probed by SPCM in Chap. 5. Both Joule heating and impact excitation could in principle explain the bias dependent shape of the EL intensity presented in Fig. 6.2. The contributions of the possible four mechanisms are discussed in more detail in Sec. 6.2.

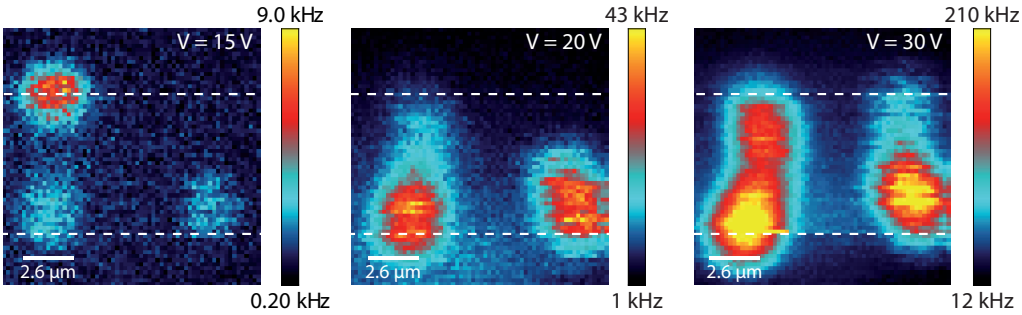

Fig. 6.2. Spatial EL intensity distribution for the same device for different bias voltages. The device consisted of two channels. The dashed white lines indicate the position of the electrodes as determined from the Raman image (not shown). The EL spot got more elongated with increasing voltage because of an increasing length of the emitting CNT segment. Presumably, at 30 V the whole (left) CNT channel emitted light.

EL spectra for a large number of devices were taken after recording an EL scan and moving the sample to the position of maximum intensity. A selection of all recorded spectra is shown in Fig. 6.3. Typical integration times were 10 s. The spectra were corrected for the wavelength dependent transmission and reflection of the optical elements (beam splitter, objective, grating) and the wavelength dependent sensitivity of the CCD camera using a calibration lamp as described in Sec. 4.2.1.

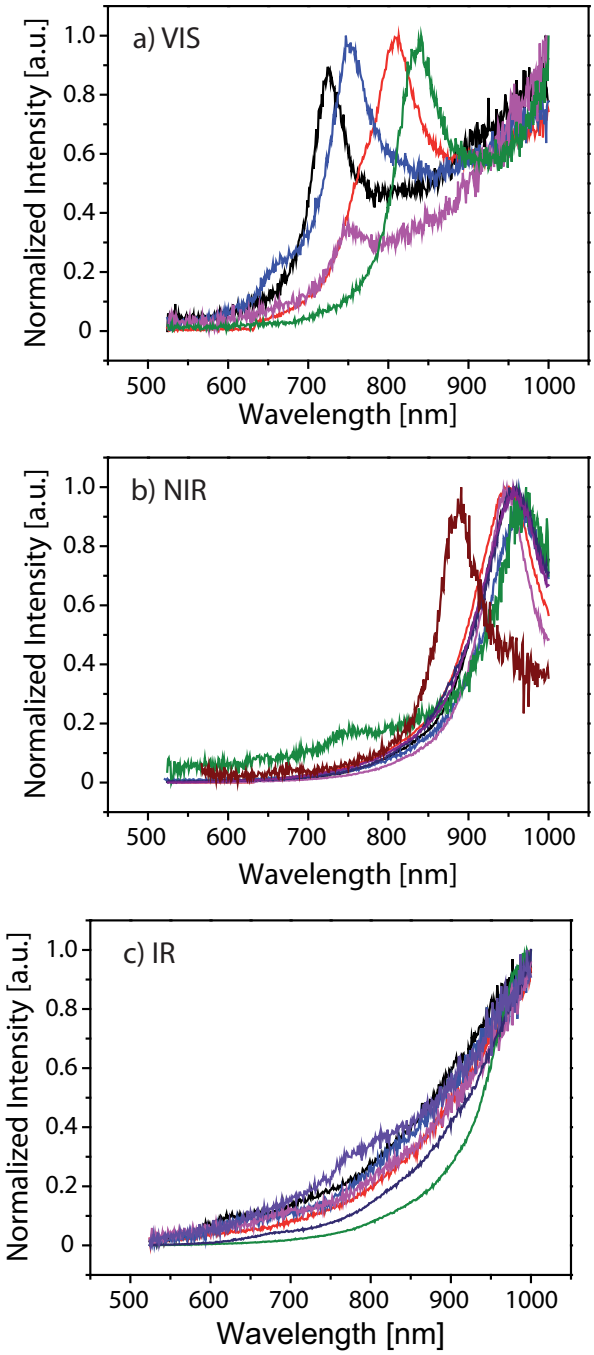

Fig. 6.3. EL spectra taken for a large number of devices. The detected spectral range is 500-1000 nm. Different emission energies in the (a) visible, (b) near-infrared, (c) infrared wavelength region were observed reflecting the different optical transition energies SWCNTs of different chiralities. The spectra were corrected for the wavelength dependent transmission of the optical elements and the sensitivity of the CCD camera.

This was required because the EL was emitted over a broader spectral range as compared to Raman scattering. The spectra revealed emission energy peaks in a broad spectral range and are divided into three groups. One group exhibits emission spectra in the visible (see Fig. 6.3 a)) wavelength region and the second in the near-infrared (see Fig. 6.3 b)). The third group shows an increasing intensity towards the infrared without any distinct maximum. Emission peaks are expected to occur at wavelengths larger than 1000 nm (see Fig. 6.3 c)). The emission energies reflect the optical transitions E_{ii} occurring in the involved SWCNTs that are different for different chiralities. In case of recombination upon ambipolar transport, a single emission peak corresponding to the E_{11}-transition is expected. Joule heating can also lead to the population of higher electronic bands, enabling emission energies corresponding to the E_{22} or even E_{33} transition. The same applies to impact excitation. At large enough electric fields, the creation of E_{22} or E_{33} excitons besides the E_{11} exciton becomes possible.

In principle, the emitting SWCNT could be identified with photoluminescence spectroscopy. Unfortunately, no photoluminescence was observed from the CVD grown SWCNTs on quartz, probably due to strong interaction with the substrate caused by the absence of a surfactant. Raman spectroscopy is another tool for the chirality assignment of a SWCNT. The radial breathing mode (RBM) is observed only in case of exact resonance of the excitation energy with a real transition of the SWCNT. Therefore, Raman measurements at four different excitation

wavelengths (514 nm, 568 nm, 633 nm and 834 nm) were performed. However, a RBM could be observed only for very few CNTs, at very low Raman shifts (around 130 cm^{-1}) corresponding to large diameter CNTs. For these CNTs, the assignment with the help of the Kataura plot is not very reliable, because the individual branches for the different transitions are very close to each other in the Kataura plot (see Fig. 2.6). Most likely, the observed EL emission did not come from E_{11} transitions, because only very thin CNTs emit in the visible or near-infrared (see Fig. 2.6). Instead, rather E_{22} or possibly even E_{33} transitions were detected, while the by far strongest E_{11} emission occurred in the infrared, far below the detection range.
The spectral width (full width at half maximum FWHM) lies for all spectra between 50 and 60 nm, larger than in case of photoluminescence. This broadening can be explained by self heating of the CNT creating hot electrons and phonons [109, 137].
The spatially resolved measurements illustrate that the EL position and shape can be very different from device to device and change with the applied bias. The spatial resolution of 1.6 µm, however, does not allow to determine the size of the actual emitting nanotube segment. Even the highest resolution of about 300 nm that could be achieved using focused light is not sufficient. In the following section, antenna-enhanced electroluminescence measurements are presented achieving a resolution of better than 40 nm.

6.2. Antenna-enhanced electroluminescence imaging

As for the resolution-limited EL measurements, antenna-enhanced investigations were performed on devices involving long CVD grown SWCNTs. In the following, antenna-enhanced EL measurements on two different devices are presented. The first device consists of a source and drain electrode made of gold fabricated by optical lithography as described in Sec. 4.1 with a separation of 12 µm. The channel is a heterogeneous network consisting of at least four CNTs. The second device is more homogeneous with a channel consisting of only one CNT.

6.2.1. Confocal investigations and network characterization

The heterogeneous device was first characterized by confocal laser microscopy, a platform used intensively in the past to gain valuable information on the optoelectronic properties of carbon based devices (see Sec. 2.2).
Fig. 6.4 presents the characterization of the investigated device by means of conventional confocal photocurrent, Raman and electroluminescence microscopy. A scanning confocal zero bias photocurrent image of the device is presented in Fig. 6.4 a) showing typical features such as photocurrent fluctuations along the CNT caused by local built-in electric fields. The inset illustrates the photocurrent signal along the channel following the white dashed line. The sudden increase in photocurrent by a factor of about 10 in the middle of the channel can be explained with the help of the Raman measurement displayed

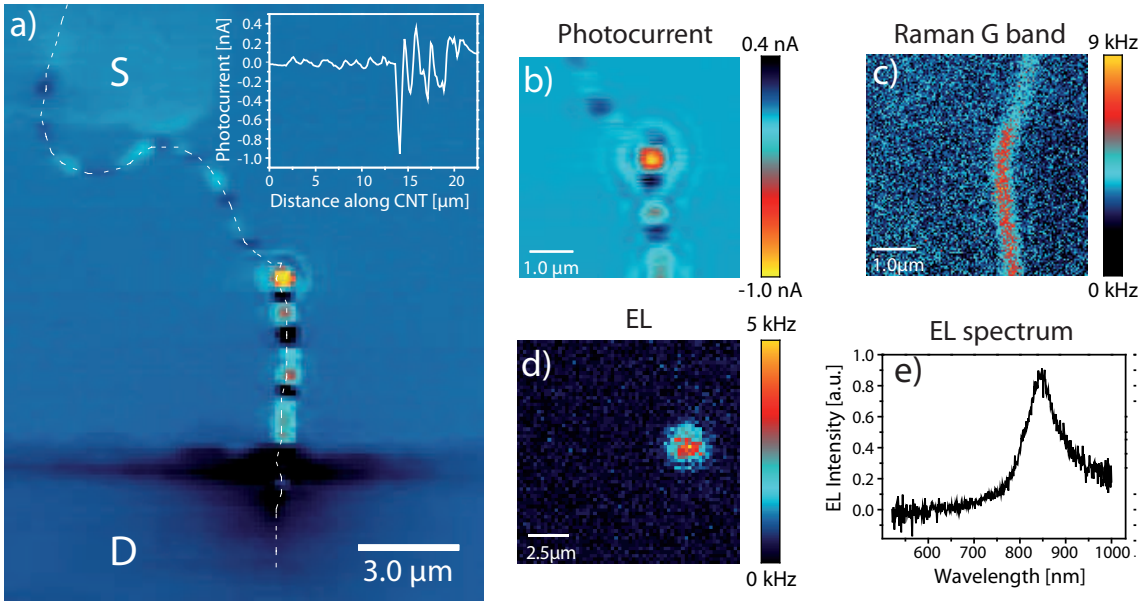

Fig. 6.4. Confocal Raman, EL and photocurrent study. a) Confocal zero bias photocurrent image of a CNT network on glass. S and D denote source and drain electrode. The inset shows the zero bias photocurrent signal detected along the white dashed line. A sudden increase in magnitude happens in the middle of the channel. b) Confocal zero bias photocurrent image (zoom). c) Confocal Raman G band image of the same region as in b). d) Confocal electroluminescence image. e) EL spectrum recorded at the bright spot in d).

in Fig. 6.4 c) that was simultaneously taken with the photocurrent measurement shown in Fig. 6.4 b). In contrast to the region of strong photocurrent fluctuations there was no detectable Raman G band signal in the region of weak photocurrent signals indicating an off resonance condition of the excitation energy for this specific SWCNT. Therefore, more than one SWCNT of different chiralities must be responsible for the current transport. The electroluminescence image presented in Fig. 6.4 d) was obtained by switching off the excitation light and applying a source-drain bias of 9 V. Bright EL appears at the location of the sudden change in the photocurrent and Raman signal. The emission has a spectral maximum in the near-infrared at about 850 nm (Fig. 6.4 e)). The spatial resolution of the photocurrent and the Raman image is diffraction-limited and given by approximately half of the laser wavelength (300 nm). Note the reduced spatial resolution of 1.6 µm in the electroluminescence image that reflects the effective size of the photo detector since no additional pinhole was used in the detection path.

In order to characterize the heterogeneous network, confocal and antenna-enhanced Raman measurements using different wavelengths were performed. Fig. 6.5 shows the network characterization in the region of interest, i. e. the region shown in Fig. 6.4 b) where the photocurrent suddenly strongly increases. Fig. 6.5 a) and b) show Raman maps of this region taken with two different excitation wavelengths of 834 nm, 633 nm, respectively. Fig. 6.6 depicts the corresponding Raman spectra.

With the help of the Raman spectra the network can be characterized according to the schematic drawing shown in Fig. 6.5 c):

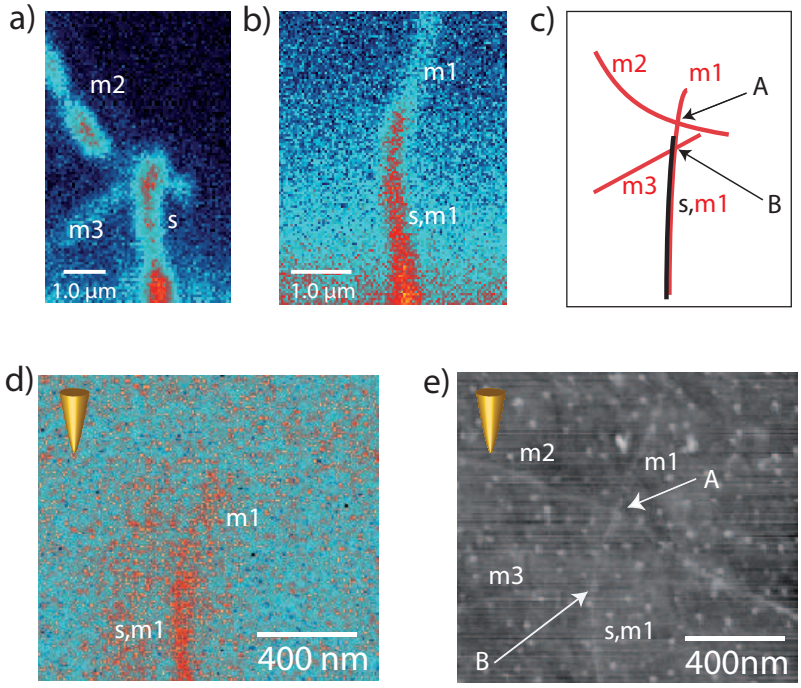

Fig. 6.5. Overview of the SWCNT network a) Raman G band image with excitation wavelength 834 nm. b) Raman G band image with excitation wavelength 633 nm. c) Schematic drawing of the CNT network showing the character of the involved CNTs. *m* stands for a metallic SWCNT, *s* for a semiconducting SWCNT as determined from the respective confocal Raman spectra in Fig. 6.6. A and B denote the two nanotube crossings referred to in the main text. d) Antenna-enhanced Raman G band image. e) Simultaneously taken topography image showing the two crossings A and B.

- $m1$ is a metallic SWCNT. Its spectrum is shown in Fig. 6.6 d). The RBM at around 200 cm^{-1} together with the excitation wavelength of 633 nm indicate that the SWCNT is metallic using the Kataura plot for CVD grown SWCNTs on quartz (see Fig. 2.6 b)).

- $m2$ and $m3$ are also metallic SWCNTs. Their Raman spectra are depicted in Fig. 6.6 a) and b). The RBM at 142 cm^{-1} together with the excitation wavelength of 834 nm (see Fig. 2.6 b)) and the shape of the G band (see Sec. 2.1.2) indicate that the SWCNTs are metallic.

- s is a semiconducting SWCNT. Its spectrum at the excitation wavelength of 633 nm is shown in Fig. 6.6 c). The fact that it shows a strong G band signal for both the excitation wavelengths 834 nm and 633 nm as shown in the Raman maps in Fig. 6.5 a) and b), indicates that this SWCNT is semiconducting (see Fig. 2.6 b)).

The topography image reveals two CNT-CNT crossings denoted by A and B in Fig. 6.5 e) in the region around the sudden photocurrent signal increase. The type of crossing can be identified using the Raman measurements. Crossing A is a crossing between two metallic SWCNTs as can be seen from the antenna-enhanced Raman image and the simultaneously

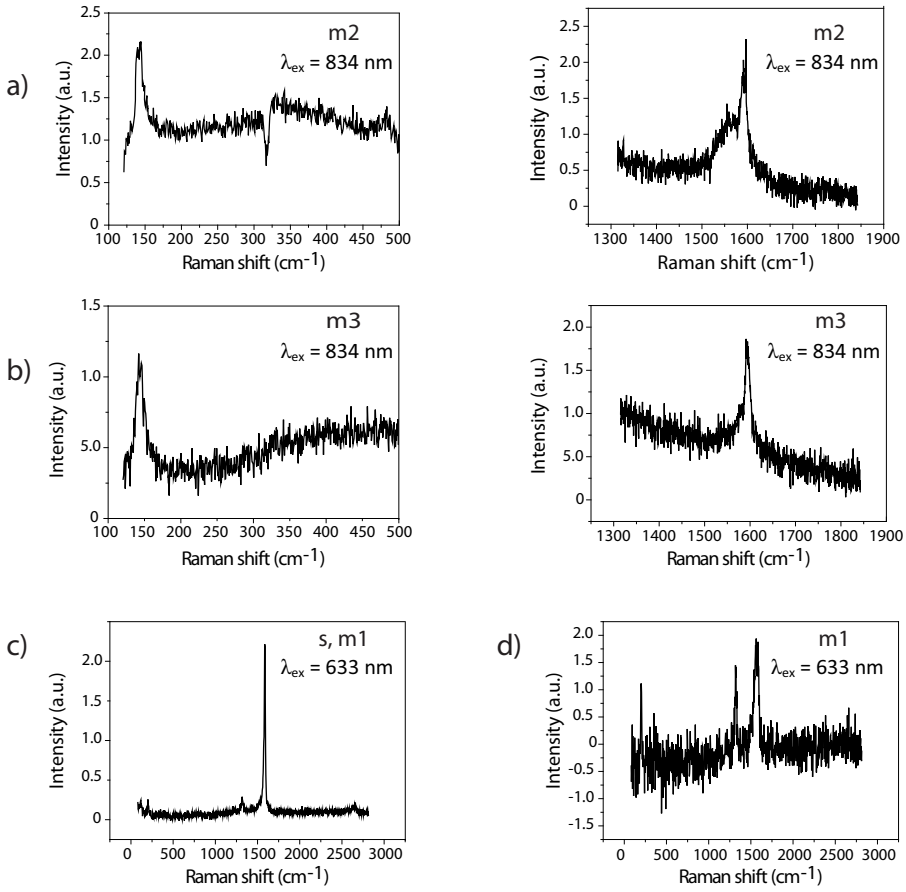

Fig. 6.6. Raman spectra of the SWCNTs of the network labeled in Fig. 6.5 c) by $m1$, $m2$, $m3$ and s. The shape of the G band at about 1600 cm^{-1} together with the position of the RBM peaks at low energies indicate the metallic character of $m1$, $m2$, $m3$ and the semiconducting character of s.

taken topography shown in Fig. 6.5 d) and e). The Raman intensity increases only below crossing A, indicating that the semiconducting SWCNT s starts behind the crossing. Crossing B involves at least the semiconducting SWCNT s and one metallic SWCNT ($m3$, eventually also $m1$). Whereas the first crossing is assumed to be a crossing of two metallic SWCNTs, the second crossing contains at least one semiconducting and one metallic SWCNT leading to a Schottky type of contact.

6.2.2. Determination of the size and the origin of the electroluminescence source

Although the network could be successfully characterized by confocal techniques and AFM measurements, the optimum spatial resolution of few hundred nanometers achievable using focused light is not sufficient to resolve the size of the source of electroluminescence and to correlate the observed signals with the nanotube network structure. In the following it is demonstrated that antenna-enhanced optoelectronic microscopy can reach a spatial resolution as high as 40 nm. Using this technique, it is possible to record sub-diffraction

photocurrent and electroluminescence images of the device yielding information that is not achievable by confocal microscopy.

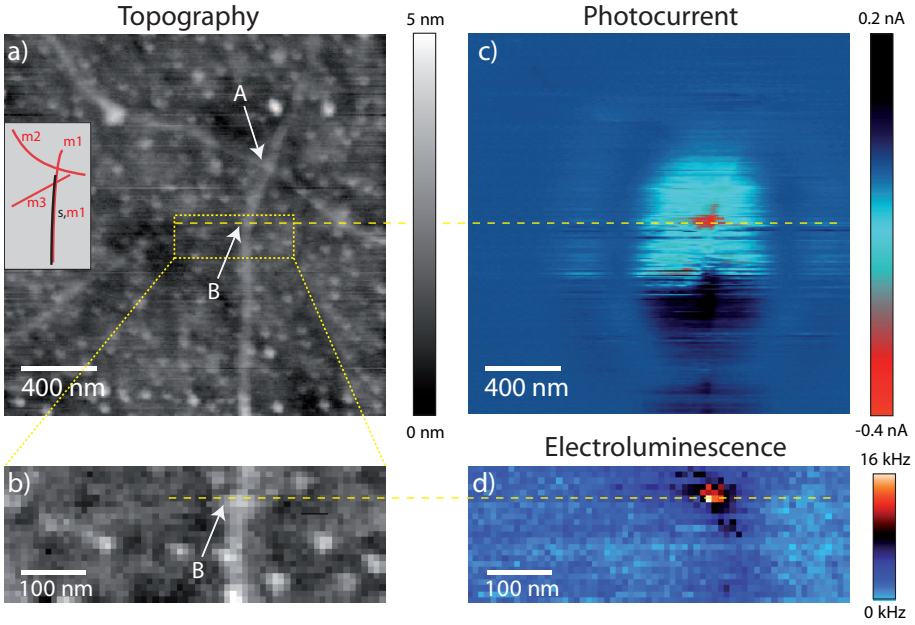

Fig. 6.7. Antenna-enhanced optoelectronic study. a) Topography image revealing two CNT-CNT junctions denoted by A and B. b) Magnified view of the topography image in the area of the lower junction B. c) Antenna-enhanced zero bias photocurrent image. d) Antenna-enhanced electroluminescence image. Sub-diffraction resolution is clearly achieved for both signals. The location of strongest absolute photocurrent and electroluminescence coincide exactly with the position of junction B as indicated by the horizontal dashed lines.

Fig. 6.7 shows the combined antenna-enhanced study of the region around the CNT-CNT crossings. The topography images (see Fig. 6.7 a) and b)) of the region where EL was observed reveal the appearance of two CNT-CNT junctions denoted by A and B. The simultaneously taken antenna-enhanced photocurrent image is shown in Fig. 6.7 c). By increasing the light absorption cross section in a nanoscale volume given by the tip apex, an enhanced narrow signal in addition to the broad confocal background observed by focused light in Fig. 6.4 a) and b) is obtained, that shows a strong maximum followed by a rapid change of signal sign. The high spatial resolution clearly reveals that junction B is responsible for the large photocurrent signal. Since the photocurrent originates from the dissociation of electron-hole pairs, a strong local electric field exists at this position. As before, a direct proportionality between the electric field and the photocurrent is assumed. The electric field is probably caused by the crossing of two or three nanotubes, forming a Schottky contact consisting of at least one metallic and one semiconducting CNT, as indicated by Raman measurements as described before. The formation of a local electric field at the junction of a metallic and a semiconducting CNT has been demonstrated before by transport and photocurrent measurements [91, 138]. The electroluminescence measurement with a source-drain voltage of 7 V reveals a bright emission site (Fig. 6.7 d)). The observed enhanced emission appears point-like in good contrast to the confocal background

and is localized at the position of the strongest electric field probed by the photocurrent configuration at junction B discussed above. Note that no emission is observed at junction A (data not shown). This can be attributed to a weaker electric field than at junction B due to the metallic character of both crossing CNTs. The antenna-enhanced EL measurement makes it possible for the first time to determine the spatial extension of the emitting nanotube segment. In the past, the extension of the emission site was hidden behind the broad diffraction-limited signal. In the case of ambipolar transport this figure gives information about the spatial extent of the recombination length and has been determined in [88] to be equal to or less than 2 µm. In the case of impact excitation, the size of the light source is a figure of merit for the screening length [9].

By taking cross sections in the directions perpendicular to and along the CNT the spatial extension of the emission site can be determined. Fig. 6.8 a) shows the cross section perpendicular to the nanotube. The narrow signal (highlighted by the red line) that is due to the near-field interaction between the emission and the antenna has a spatial width of about (45 ± 10) nm (full width at half-maximum). Because the diameter of the CNT of about 1 nm is substantially smaller, the width of the recorded signal can be taken as the spatial resolution of the experiment. The signal background consists of two contributions that can be seen in the insets in Fig. 6.8 a) and b): The nearly uniform confocal background resulting from diffraction-limited collection that appears in blue; and an additional contribution seen as black area with a spatial width of around 100 nm that could be attributed to a long-range electrostatic interaction between tip and nanotube. During the scanning process the gold tip might get slightly electrostatically charged and act as a weak local gate influencing the band energy of the nanotube. Such a Coulomb interaction will scale with the inverse of the tip-sample distance and is thus expected to lead to a longer ranged interaction and hence broader signal contrast compared to the near-field optical interaction that is based on a dipolar interaction [124].

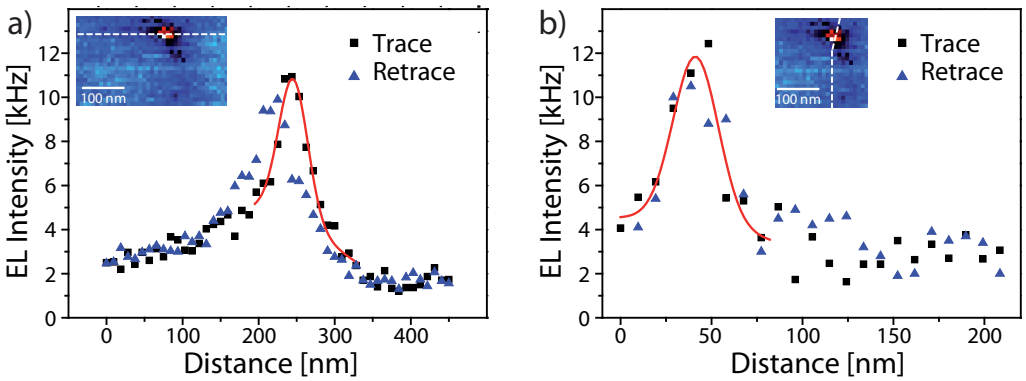

Fig. 6.8. Size of the source of electroluminescence. a) Antenna-enhanced EL cross sections perpendicular and b) along the CNT. The red lines are a guide to the eye to highlight the near-field contribution. Since the cross sections taken along and perpendicular to the CNT have about the same width of 40 nm, the extension of the EL source along the CNT needs to be substantially smaller, probably below 20 nm.

The cross section taken along the CNT (Fig. 6.8 b)) also shows a spatial width of about (30 ± 10) nm. The values for both directions lie in the expected range of the spatial resolution of the system that is determined by the tip size. Because the signal width recorded along the nanotube is similar to the spatial resolution determined from the perpendicular cross section as discussed above, the actual width of the EL source must be substantially smaller. More specifically, the detected EL image is a convolution of the actual EL source and the point-spread function (PSF) of the near-field imaging system. The latter can be approximated by the cross section recorded perpendicular to the CNT due to the small CNT diameter. Assuming a Gaussian PSF and Gaussian shaped EL intensity distribution of the source, the measured signal width will be $w = \sqrt{w_{PSF}^2 + w_{ELsource}^2}$, where w_{PSF} and $w_{ELsource}$ are the width of the PSF and of the source, respectively. Because the measured width w is approximately equal to the measured w_{PSF} with an absolute error of 20 nm, the size of the EL source must be smaller than 20 nm. Therefore, the emission is assumed to be point-like and occurs on a length scale smaller than 20 nm.
From Fig. 6.8 a) the enhancement factor f of the radiative rate $f_{rad} = \frac{k_{rad}^{antenna}}{k_{rad}}$ induced by the antenna can be estimated. Neglecting changes in the non-radiative relaxation rate f_{rad} is equal to the intensity enhancement $f_{rad} = \frac{I_{NF}}{I_{FF}} \approx \frac{9\,\mathrm{kHz}}{2\,\mathrm{kHz}}$, where I_{NF} is the intensity of the enhanced near-field signal, I_{FF} the intensity of the confocal far-field signal. Here, it was taken into account that the near-field volume is equal to the far-field volume due to the small extension of the EL source (see Sec. 3.4). The present value of $f_{rad} \approx 4.5$ is comparable to previous results obtained for the photoluminescence from carbon nanotubes with etched gold tips [21].

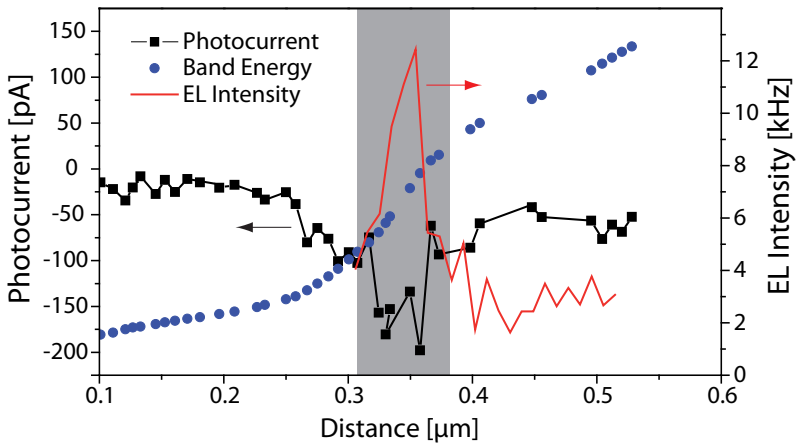

Fig. 6.9. Spatial correlation between EL and photocurrent. Antenna-enhanced zero bias photocurrent measured along the device (black square symbols), band energy (blue round symbols) and measured EL intensity (red line). The EL peaks at the position of highest photocurrent and highest band energy gradient.

From Fig. 6.7 it is clear that a spatial correlation between the photocurrent and the electroluminescence exists and that both peak at the position at which the vertically oriented CNT carrying the photocurrent crosses a second, horizontally oriented CNT slightly visible in the topography image. Since the photocurrent signal is proportional to the dissociation

rate of the optically created excitons, it scales with the local electric field that is present in the excitation region. Spatial integration of the photocurrent along the CNT gives the electron band energy profile $E(r) = -\int I_{PC}\mathrm{d}r$ as illustrated in Fig. 6.9. The black squares represent the antenna-enhanced photocurrent obtained by fitting the near-field contribution of the signal cross sections perpendicular to the nanotube by a Gaussian function for all positions along the nanotube. The blue circles represent the electron band energy profile E. The negative photocurrent peak results in a steep increase of the band energy. By overlaying the photocurrent and electroluminescence signal along the CNT as shown in Fig. 6.9 (gray shaded region), it can be seen that the electroluminescence spot appears at the position of highest (absolute) photocurrent, at the steepest region of the energy band, respectively. This indicates that the electroluminescence is caused by impact excitation. This mechanism requires a strong electric field in which charge carriers are accelerated locally gaining the kinetic energy sufficient for creating excitons via collisions with other carriers. These excitons can decay radiatively generating an electroluminescence signal with a photon energy that corresponds to the involved exciton energy. In principle, other mechanisms besides impact excitation could also contribute to the observed emission as discussed in Sec. 2.2. However, substantial contributions of these mechanisms are unlikely based on the device configuration and the experimental results. More specifically, charge carrier recombination due to ambipolar transport for the non-gated devices can be ruled out. CNT devices without gate voltage are known to act as p-doped unipolar devices under ambient conditions [73]. The ambipolar regime could be reached by fabricating a p-n junction [111], asymmetric contacts [112] or suitable bias-gate-voltage combinations [109, 110]. Phonon-assisted radiative decay from the M-point discussed in [119] can be excluded, because the associated emission peaks at 1.4 and 1.8 eV are not observed (see spectrum in Fig. 6.4 e)). Finally, electroluminescence can also be due to radiative recombination from thermally populated higher energy bands due to Joule heating. Joule heating is expected to be strongest at the position of the largest voltage drop along the channel, which could indeed occur at the junction where the electrical resistance will be high. However, strong thermal emission was only observed for suspended metallic SWCNTs [116, 118] while for non-suspended SWCNTs, as in the present case, only very weak emission occurred due to highly efficient substrate cooling [119]. On the basis of this discussion and the occurrence of the EL at the position of the strongest local field as determined from the photocurrent data as well as its spectral characteristics, impact excitation is considered as the main cause for the observed emission.

While pinning of the EL to a point-like region of about 20 nm was observed for the device discussed in the previous section, another device showed EL emission from an extended region of more than 100 nm length with weaker contrast (see Fig. 6.10 c)). As can be seen from the confocal EL and PC images (see Fig. 6.10 a) and b)), the EL occurs at about half of the channel length at the position of strongest photocurrent. As for the previous device this indicates, that the EL is caused by impact excitation. However, in contrast to the

first device, the EL does not appear at a cross-junction but along a single SWCNT with an extended electric field in this region. Local built-in electric fields along CNT devices have been observed before and can be attributed to structural defects or environmental effects such as charge traps in the substrate or doping by local adsorbants [87].

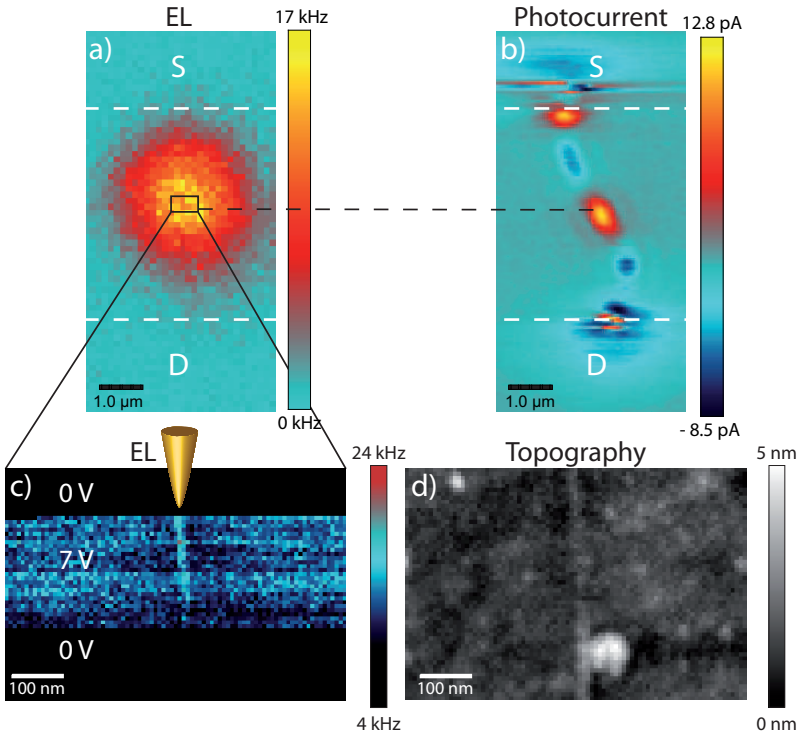

Fig. 6.10. Antenna-enhanced EL of a second device. a) Confocal EL image and b) Confocal photocurrent image. The EL occurs at the position of strongest photocurrent signal. c) Antenna-enhanced EL image. The confocal and enhanced EL appear upon biasing (7 V). d) Simultaneously taken topography image. The high spatial resolution reveals an emitting nanotube segment that is longer than 100 nm.

6.3. Summary

In summary, this chapter presented confocal and antenna-enhanced electroluminescence measurements of SWCNT devices. Resolution-limited measurements showed strong variation of the position and shape of the EL intensity from device to device. In most cases, the EL emission was observed at the contacts, but some devices also showed EL emission along the CNT channel. The length of the emitting CNT segment increased with increasing bias voltage, leading to an elongated shape of the EL intensity distribution. Both effects could be explained by considering Joule heating or impact excitation as origin of the EL emission. Spectrally resolved measurements revealed distinct emission peaks from device to device, corresponding to the transitions of the different involved SWCNT chiralities. Emission energies in the visible, near infrared and in the far infrared were observed. Although spatially resolved measurements showed a variation in the EL spot size, the resolution was not sufficient to resolve the size of the source, i. e. the length of the emit-

ting CNT segment. Antenna-enhanced electroluminescence measurements were presented, demonstrating a spatial resolution of about 40 nm. They revealed that the source of EL can be point-like with an extension smaller than 20 nm. This pinning to a point-like region took place at a CNT-CNT nanotube junction. By complementing the EL measurements with antenna-enhanced photocurrent measurements, a strong local electric field was probed at this junction, indicating that impact excitation was the responsible mechanism. Antenna-enhanced and confocal Raman measurements revealed that the junction consisted of at least one metallic and one semiconducting CNT, i. e. a Schottky contact that is known to be associated with an electric field. While this device showed a strong localization of the EL to a point-like region, a second investigated device revealed that the EL comes from a CNT segment with a length of at least 100 nm.
By combining EL, photocurrent and Raman measurements, antenna-enhanced optoelectronic probing was shown to be a powerful tool for the investigation of nanoscale devices. However, due to the short electrical stability of the CNT devices during the voltage apply, time-consuming, systematic near-field studies on the same device are challenging. Therefore, only few devices could be successfully investigated by keeping the image acquisition time as short as possible. Different means to improve the durability of the devices were tested, such as working under inert atmosphere or applying an ac-voltage to reduce the average dissipated power, but no significant improvement could be achieved. This problem is not expected for thicker 1D or 2D structures.

7. Summary and outlook

In the course of this work, the first high-resolution optoelectronic images recorded with a scanning tip operating as an optical antenna were accomplished. Up to date, tip-enhanced near-field optical microscopy has been mainly used in spectroscopic applications. Purely optical responses such as fluorescence or Raman scattering of a variety of sample materials could be studied with sub-diffraction resolution allowing deep insights into the optical and electronic properties of nanostructures. In this work, TENOM was applied to nanoelectronic devices based on carbon nanotubes to probe their optoelectronic response, i. e. photocurrent and electroluminescence signals, with a spatial resolution of better than 40 nm.

An important prerequisite for the successful implementation of this technique was the development of a reliable sample preparation method. All samples required to be transparent and to be homogeneously covered with single CNTs with an appropriate density. For this, different CNT materials were tested before the actual device fabrication via electron beam and optical lithography. The optical measurements were performed using a confocal optical microscope. This was modified and extended in order to record confocal and antenna-enhanced photocurrent and electroluminescence signals. As a result, high-resolution Raman, photocurrent and electroluminescence images with a spatial resolution better than 40 nm could be recorded. By combining all three measurement types and the topographic information, new insights into the optoelectronic properties of CNT based optoelectronic devices could be gained. The key findings are described in the following.

First, antenna-enhanced photocurrent microscopy was applied to single CNT devices in order to study the signal enhancement mechanism for optoelectronic signals. In optoelectronic applications either the excitation *or* the emission rate is enhanced, in contrast to spectroscopy, where both rates are affected by the antenna. This leads to a weaker enhancement and thus lower spatial resolution in case of optoelectronic signals. In fact, theory predicts a signal enhancement weaker by a factor of $\sqrt{2}$ compared to Raman scattering. By simultaneously imaging the Raman and photocurrent signal of a CNT device, this ratio could be experimentally verified. A mean value of 1.49 and a standard deviation of 0.26 was found for the ratio of both signals. This value is very close to the mathematically predicted number. The small derivation could be attributed to a non-perfect Gaussian position dependence of the field enhancement factor caused by an asymmetric tip.

Then, two applications of antenna-enhanced photocurrent microscopy were presented. First, the CNT-metal contacts of a device based on a single, metallic CNT were studied. At CNT-metal interfaces, photocurrent signals at zero bias voltage can be generated

by both a photovoltaic and a thermoelectric effect. Up to date, the contributions of both effects could not be imaged separately due to an insufficient spatial resolution. The high resolution provided by antenna-enhanced photocurrent imaging made it possible to map the photovoltaic contribution that manifests itself in a decaying photocurrent signal reflecting the shape of the energy band. It was found that the band energy decays exponentially with a decay length of about 500 nm for this device. This measurement confirmed also the existence of an energy barrier for a metallic CNT contact. For such a metal-metal contact this observation was rather surprising and was attributed to the low-dimensionality of a CNT.
As a second application, antenna-enhanced photocurrent microscopy was applied to another device to detect fluctuations of the CNT band energy occurring on a very small length scale. With confocal photocurrent imaging, these modulations could not be detected at all due to spatial averaging. High-resolution spectroscopic Raman images were recorded simultaneously with the photocurrent in order to reveal the origin of the modulations. As a result, they were not caused by defects that would lead to an increased D band scattering intensity in the Raman spectrum. Instead, correlating the photocurrent with the simultaneously taken topography revealed that these fluctuations occurred at positions of distinct features in the topography profile along the CNT. The most pronounced feature, a potential minimum, was present at the position of a small nanoparticle in the vicinity of the CNT. Therefore, charges associated with this particle were assumed to be the cause.

Second, the reverse process, electrically-induced light emission was studied. Resolution-limited measurements showed, that the position and spatial extension of the EL intensity varied from device to device. However, the diffraction-limited resolution did not allow to determine the exact size of the emitting CNT segment. Antenna-enhanced electroluminescence microscopy was then implemented and the first high-resolution EL measurements of a nanoelectronic device could be recorded. It was applied to study the EL emitted by a device consisting of several CNTs of different chiralities. The EL emission was found to occur at the position of a cross junction of at least two CNTs and the intensity was strongly localized to a point-like region. From this measurement the size of the EL source could be determined to be smaller than 20 nm. Such a strong pinning of EL emission was never observed before. Raman measurements revealed that the junction consisted of at least one semiconducting and one metallic CNT, forming thus a nanoscale Schottky contact. Schottky contacts are known to be connected to an electric field in the interface region. This electric field could be probed by antenna-enhanced photocurrent imaging. Thus, by combining both antenna-enhanced photocurrent and electroluminescence imaging, insight into the origin of the EL emission for this specific device was gained. In principle, there are several mechanisms that could be responsible for the observed light emission, each contributing to a varying degree. The fact that EL occurred at the position of strongest electric field, indicated that the mechanism was most likely impact excitation. Impact

excitation requires strong local electric fields, in which charge carriers are accelerated and create excitons via collisions with other carriers.
A strong localization of the EL emission was shown for this specific device at a cross junction. A second, more homogeneous device was investigated. In contrast to the first device, EL emission from a CNT segment with a length of more than 100 nm was probed. This revealed that the emission could occur on several length scales, depending on the local electric field responsible for the EL emission.
The results obtained in the scope of this work demonstrated that antenna-enhanced optoelectronic probing could be successfully applied to study CNT based optoelectronic devices. However, systematic studies on the same device are challenging. Upon a large voltage apply as in EL measurements, the devices were not very durable and electrical failure occurred on a regular basis. The cause could be oxidation of Joule heated CNTs leading to an electric break down. As a consequence, the measurement times must be kept as short as possible. Besides this, antenna-enhanced optoelectronic probing is a very versatile tool that could also be applied to other sample materials, for example graphene, MoS_2 or films of pentacene. Also the investigation of devices based on 1D materials others than CNTs, such as semiconducting, inorganic nanowires, e. g. cadmium selenide or gallium arsenide nanowires is expected to be straightforward. Devices based on these nanowires are also expected to be more enduring due to their larger diameter. In the course of this work, all measurements have been performed without a gate electrode. Including a gate electrode into the device configuration will open up many new possibilities. For example, the influence of the gate on the extension of the band bending could be studied via antenna-enhanced photocurrent microscopy. With the help of a gate electrode the ambipolar transport regime can be accessed and one could study the spatial extension of the recombination length via antenna-enhanced electroluminescence microscopy. Using semiconducting CNTs that show photoluminescence makes many new future experiments possible. By correlating the spatial distribution of photoluminescence, photocurrent and electroluminescence signals, new insights into the role of excitons in the signal generation could be gained.

A. Sample fabrication details

A.1. Electron beam lithography

In the following, the exact parameters for the electron beam and optical lithography are listed.

Spin coating of PMMA 500k
step 1: 3 s at 800 rpm
step 2: 30 s at 5000 rpm
Soft bake (hot plate)
time 120 s
temperature170 °C

UHV thermal evaporation of chromium
layer thickness 2-3 nm

Electron beam writing acceleration voltage 10 kV
dose 150µC/cm^2

Stripping of chromium layer
chromium etchant (No.1, *MicroChemicals*):water 1:1, time 25 s
rinse with DI water

Development developer MIBK:isopropanole 1:3 time 50 s
isopropanole bath to stop developing time 15 s

Metal evaporation
Titanium 0.5 adhesion layer
Gold or Palladium 30 nm

lift-off
Remover acetone bath or NMP
soak-in time 15-20 min
temperature 40 °C

pipette bubbling, ultrasound bath

A.2. Optical lithography

Spin coating of resist S1813
step 1: 3 s at 800 rpm
step 2: 30 at 6000 rpm

Soft bake (hot plate)
time 90 s
temperature 115 °C

Exposure
exposure time 15 s

Development
developer Microposit 351
time 20 s

Metal evaporation
Titanium 0.5 adhesion layer
Gold 30 nm

lift-off
remover acetone or NMP
soak-in time 15-20 min
temperature 40 °C
pipette bubbling, ultrasound bath

B. Tip-enhancement of up-conversion photoluminescence of rare earth ion doped nanocrystals

This chapter is based on the manuscript "Tip-enhancement of up-conversion photoluminescence from rare-earth ion doped nanocrystals", *submitted* (2014).

B.1. Introduction

Tip-enhanced near-field optical microscopy (TENOM) is a scanning probe technique that is widely employed to study nanostructures with sub-diffraction spatial resolution combined with substantial signal enhancement [139]. It exploits the locally enhanced electric fields in the vicinity of a sharp metal tip to amplify the excitation and emission rates in a nearby sample object. In this sense the tip acts as an optical antenna [124] that can be used to enhance multiple optical responses including Raman scattering, photoluminescence, electroluminescence as well as photocurrent [139]. Because of the rapid decay of the locally enhanced field inside the sample material, on the order of 10 nm depending on the tip size [140], TENOM is a surface sensitive technique. It is hence ideally suited for the investigation of very thin nanomaterials or sub-surface structures and has been applied to a huge variety of materials, including polymer thin films [141], carbon nanotubes [21, 140, 142], inorganic semiconducting nanowires [28–30], single molecules [26, 27], RNA [32] and graphene [24, 25].

In the simplest case the enhanced detected signal scales linearly with the incident laser intensity, while its source remains completely local. For higher excitation intensities non-linear processes such as two-photon absorption [143] and stimulated Raman scattering [144] could become important, while for spatially extended structures energy transport [141, 145] leading to non-local emission can complicate the image contrast formation. Here, tip-enhanced two-photon photoluminescence measurements on extended nanocrystals doped with Er^{3+} and Yb^{3+} is reported. Rare-earth ion doped crystals provide an efficient conversion of near-infrared into visible light and are thus of particular interest for a variety of applications such as multi-modal bioimaging contrast agents [146, 147] and solar cell activators [148]. Metal-particle enhanced up-conversion has been reported by several groups up to date. The first results were obtained by introducing silver particles into

the crystal matrix [149–151]. More recent studies were based on depositing nanocrystals on a gold pyramid substrate [152] or on a gold nanograting [153]. Schietinger *et al.* [154] performed experiments in which they controlled the particle-nanocrystal distance using an AFM. They demonstrated the controlled plasmon-enhancement of the up-conversion PL in $NaYF_4$ nanocrystals doped with Er^{3+} ions together with a reduction of the excited state lifetime.
In this work, the first near-field studies using a scanning tip is presented. A large signal enhancement is observed and two-photon excitation and homo-energy transfer between the ions within the nanocrystal are discussed as possible contributions. The discussion is complemented by time-resolved PL measurements. In addition, inhomogeneous spatial intensity distributions are observed that are different for the emission wavelengths of Er^{3+}. This can be attributed to the interplay between the actual tip shape and the nanocrystal topography becoming particularly relevant in case of large sample structures.

B.2. Experimental setup and sample fabrication

The nanocrystals consisted of a α-$NaYF_4$ crystal matrix doped with Yb^{3+} as a sensitizer and Er^{3+} as the activator. The dopant concentration for Yb^{3+} was 20 Mol % and 2 Mol % for Er^{3+} respectively. Due to the preparation procedure, the dopant concentration was considered to be homogeneous within the nanocrystal. The excited state level scheme of the activator-sensitizer system showing the two detected transitions in the visible is presented in Fig. B.1 together with a schematic of the experimental setup.

B.2.1. Microscope setup

The optical setup combines an inverted confocal oil immersion microscope with a tuning fork shear-force distance control as described in Sec. 4.2. A scheme of the setup is shown in Fig. B.1 a). The nanocrystals were excited with a Gaussian laser beam at 980 nm focused by a high NA objective (NA=1.49) onto the nanocrystals. For image acquisition the sample was raster scanned while keeping tip and focus position fixed. The detection path was split into two channels in order to record two emission bands simultaneously. The two emission bands belong to the ${}^4S_{3/2}$,${}^2H_{11/2} \rightarrow {}^4I_{15/2}$ and the ${}^4F_{9/2} \rightarrow {}^4I_{15/2}$ transition (see Fig. B.1 b)) and were detected using two APDs after band pass filtering centered at 550 nm ± 25 nm for the green emission and at 660 nm ± 15 nm for the red emission, respectively. No additional detection pin-hole was used. Hence the spatial resolution of the confocal experiments was given by diffraction at the excitation wavelength $\Delta x = \approx 0.51/\sqrt{2} \cdot 980\,\mathrm{nm}/\mathrm{NA} = 252\,\mathrm{nm}$. For time-resolved measurements a multiscaler card (MSA-300, Becker& Hickl) was used triggered by the laser operating in the pulse mode and generating 5 µs long pulses. The effective temporal resolution of the detection system was about 5 µs.

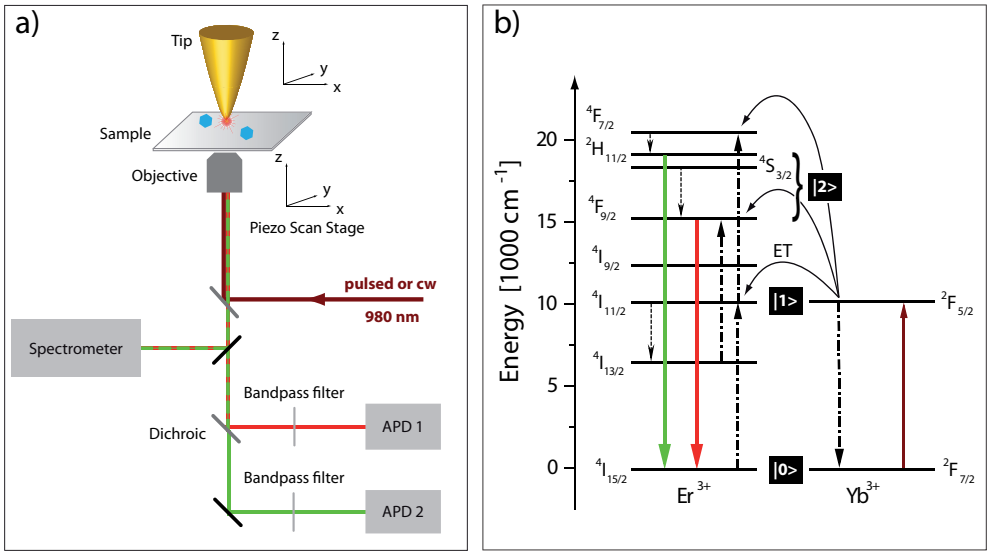

Fig. B.1. a) Schematic of the experimental setup. An inverted confocal microscope was combined with a tuning fork AFM to scan a gold tip in close vicinity to the sample surface. The detection path consisted of two channels equipped with avalanche photodiodes (APDs). Spectral bandpass filters centered at (550 ± 25) nm and (660 ± 15) nm were used to select the ${}^4S_{3/2}, {}^2H_{11/2} \rightarrow {}^4I_{15/2}$ and the ${}^4F_{9/2} \rightarrow {}^4I_{15/2}$ transition, respectively. b) Excited state level scheme of the activator - sensitizer system comprising Yb^{3+} and Er^{3+} ions in a single nanocrystal. Brown solid, dashed-dotted and dashed lines indicate absorption, energy transfer (ET) and multi-phonon relaxation, respectively. The radiative transitions giving rise to green and red emission are indicated with solid lines. The ground, intermediate and first excited states are marked with $|0\rangle$, $|1\rangle$ and $|2\rangle$.

B.2.2. Sample preparation

The nanocrystals were synthesized following the procedure described in [155] and are existent in the cubic α-$NaYF_4$ phase. A homogeneous distribution of the dopants within the nanocrystal is assumed for the following reason: During the doping process, Y^{3+} ions are randomly replaced by Yb^{3+} and Er^{3+} and the respective concentrations of 20 % and 2 %. At such high concentrations the doping must be homogeneous substituting Y^{3+} or occur close to the surface creating defects in the nanocrystal matrix. Because XRD measurements performed after the synthesis do not show the presence of any defects, the doping is considered as homogeneous. The nanocrystals dispersed in chloroform were then spin-coated onto a glass substrate for the optical and topographic measurements.

B.3. Results and Discussion

B.3.1. Quantification of the volume normalized signal enhancement

Fig. B.2 a) shows a tip-enhanced near-field image of a nanocrystal probing the ${}^4S_{3/2}, {}^2H_{11/2} \rightarrow {}^4I_{15/2}$ transition together with the simultaneously recorded topography image in b). The optical image features two distinct signal contributions: First, a narrow circular contribution with nearly uniform intensity and steep edges that dominates the image contrast. Indicated by the dashed lines in a) and b), this contribution is centered at the

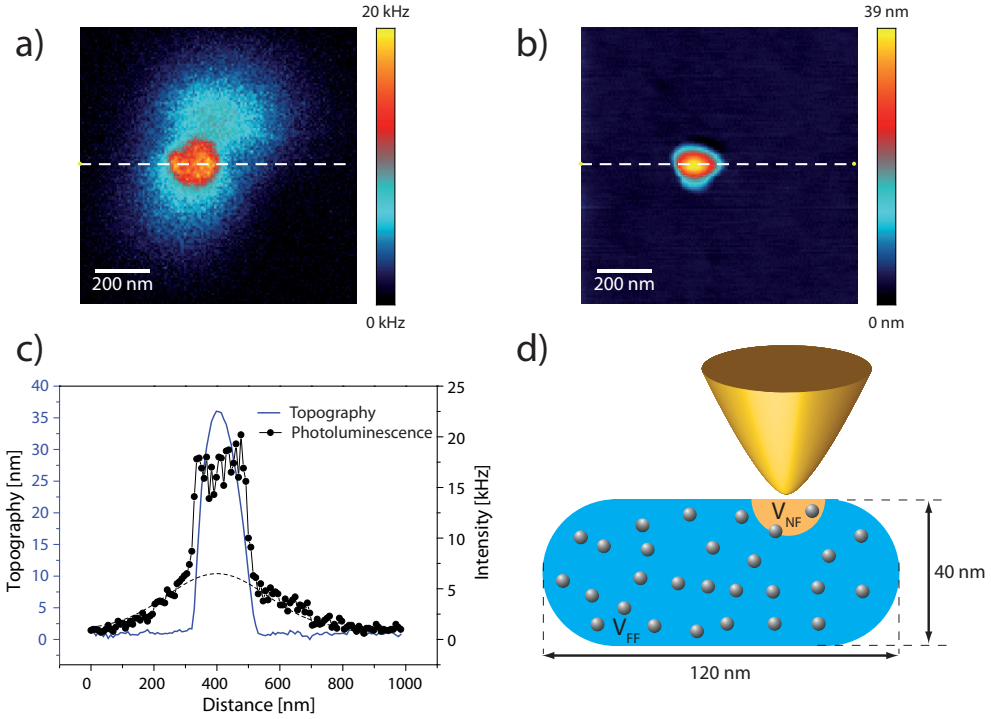

Fig. B.2. a) Tip-enhanced PL image of the green emission at 550 nm upon two photon excitation at 980 nm. In addition to the far-field background, there is a clearly sub-diffraction enhanced contribution. b) Simultaneously taken topography image. c) Topography (blue line) and intensity (black dots) cross sections taken along the white dashed lines in a) and b), respectively. The Gaussian fit to the far-field signal is shown as black dashed line. d) Schematic of the tip-enhancement of the nanocrystal PL together the nanocrystal dimensions as determined from the topography data in b). The far-field and near-field volume is shown in blue, orange respectively. The gray spheres symbolize the Er^{3+} ions.

position of the nanocrystal as determined from the topography data. The spatial width of the contribution of about 190 nm is clearly below the diffraction limit at the excitation wavelength even considering two-photon absorption ($\approx 0.51/\sqrt{2} \cdot 980\,\mathrm{nm}/\mathrm{NA} = 252\,\mathrm{nm}$) and thus demonstrates tip-enhanced near-field interactions.

The second about 400 nm wide signal is the confocal far-field contribution. Its elongated shape is expected. Since the transition dipole moments of the ions are isotropically distributed within the nanocrystal, the confocal image reflects the excitation intensity distribution [156]. Strong focusing is known to lead to two lobes with significant longitudinal field components that are displaced from the center of the focus rendering a quasi elliptical intensity distribution. The near-field contribution identified above occurs in one of the longitudinal side lobes since tip-enhancement is strongest for axial field components [157].

To quantify the near-field to far-field image contrast, the signal intensity was extracted along the dashed white line shown in Fig. B.2 a) together with a Gaussian fit of the far-field contribution to determine its amplitude. This gave a near-field intensity of about 22 kHz (photon counts per second) and a far-field signal of 7 kHz, respectively, yielding an intensity enhancement of about $\frac{I_{NF}}{I_{FF}} = \frac{29-7}{7} \approx 3$. The steep edges and plateau-like pattern in Fig. B.2 a) can be understood based on the sketch shown in Fig. B.2 d). Because

of the short penetration depth of the locally enhanced field that determines the near-field interaction volume, a further increase of the topographic height did not lead to an increase of the near-field signal.

For the determination of the local signal enhancement factor, the different volumes that contributed to the near-field and far-field signal must be considered. Since the nanocrystal size was substantially smaller than the confocal far-field excitation spot, the volume generating the far-field signal corresponds to the nanocrystal volume that could be estimated from the AFM data and the topography profile shown in Fig. B.2 b) and c). The AFM data suggests a nanocrystal width of about 200 nm in both lateral directions and a height of 40 nm. The observed shape is of course influenced by the tip geometry. Especially at large nanocrystal heights, the finite tip diameter and particularly a large opening angle can significantly broaden the observed spatial width. In order to estimate the actual nanocrystal volume, the influence of the tip diameter and opening angle on the topography profile was studied by means of simple geometric considerations presented in Sec. B.5.1. A broad tip with a large diameter of 60 nm and opening angle of 45° was taken into account in order to determine a lower limit for the crystal volume. It was found that the nanocrystal had at least a width of 120 nm to result in a width of about 200 nm when imaged by the tip. The associated volume of $390 \cdot 10^3\,\mathrm{nm}^3$ is taken as a lower limit for the nanocrystal volume. Because only sharp tips are known to provide a strong electric field enhancement as observed in Fig. B.2 a), the tip diameter was probably substantially smaller, yielding even larger nanocrystal volumes. A sketch of the experimental configuration including the nanocrystal dimensions is given in Fig. B.2 d), depicting the nanocrystal as elongated structure. Its endings were approximated by half spheres in order to simplify the calculations.

According to this sketch, the near-field interaction volume was approximated by a spheric section, with diameter and height depending on the tip diameter. Assuming a sharp tip with a diameter of 20 nm, it is a half-sphere with a radius of 10 nm corresponding to a sample volume of $V_{NF,min} = \frac{2}{3}\pi 10^3\,\mathrm{nm}^3 = 2.1 \cdot 10^3\,\mathrm{nm}^3$. Here, the 10 nm reflect the penetration depth of the near-field into the nanocrystal. The near-field interaction volume is associated with an uncertainty coming from the exact tip size. While the lateral extension for a broader tip increases, the penetration depth will probably be less affected due to dielectric screening in the crystal. For a tip with a diameter of 60 nm, the near-field volume was approximated by a spheric section with a radius of 30 nm and a height of 15 nm leading to a $V_{NF,max} \approx 18 \cdot 10^3\,\mathrm{nm}^3$.

Based on these considerations, a minimum value of $V_{FF}/V_{NF} = 390 \cdot 10^3/18 \cdot 10^3 \approx 22$ and a maximum value of $V_{FF}/V_{NF} = 390 \cdot 10^3/2.1 \cdot 10^3 \approx 185$ for the far-field to near-field volume ratio were obtained. These values give a lower and an upper limit of the volume-normalized enhancement ratio of $\left(\frac{I_{NF}}{I_{FF}}\frac{V_{FF}}{V_{NF}}\right)_{min} = 66$ and $\left(\frac{I_{NF}}{I_{FF}}\frac{V_{FF}}{V_{NF}}\right)_{max} = 555$. Remarkably, even the lower limit is substantially larger than what is typically observed for the PL intensity enhancement in other sample materials such as nanotubes and nanowires using the same type of tips [21, 30]. These experiments are usually performed using a

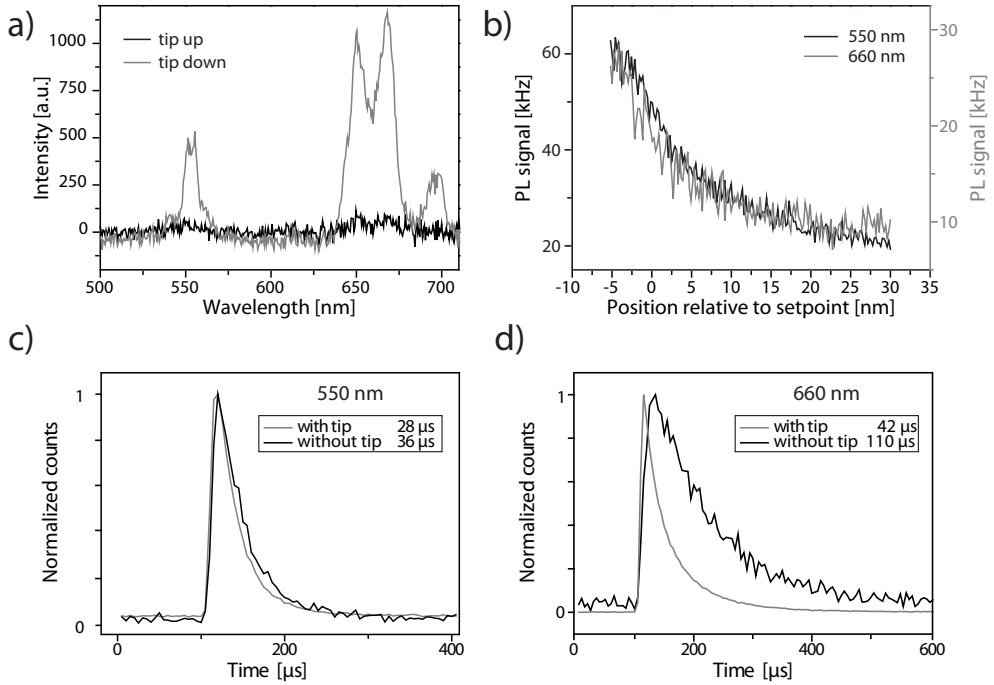

Fig. B.3. a) Spectra with retracted and approached tip, respectively. Both emission bands are clearly enhanced. b) Tip-sample distance dependence of the emission detected at 550 nm and 660 nm. The continuous signal rise for decreasing tip-sample distance clearly proofs the short-ranged near-field origin of the enhancement. Up to the minimum absolute distance, no signal decrease is observed that would indicate metal-induced quenching. The life time reduction seen in c) and d) is therefore due to radiative rate enhancement. c) and d) Transients for red and green emission detected with and without tip at 550 nm and 660 nm, respectively. The lifetime with tip is substantially shorter than without tip.

radially polarized donut mode, that has a strong electric field component in the direction of propagation leading to a very efficient enhancement. Considering this, the enhancement observed here, using a Gaussian mode, is even more striking.

Similar near-field to far-field intensity ratios were measured for several nanocrystals and tips. For the red emission similar or even larger intensity ratios were observed depending on the tip used as can be seen in the tip up/down-spectra in Fig. B.3 a) and in Fig. B.4. For the tip used in Fig. B.2 a), the lower and upper limit for the volume normalized near-field to far-field ratios of the red emission detected at 660 nm were 330 and 2775 (data not shown).

B.3.2. Discussion of the two-photon excitation process

In the following, the two-photon excitation process is discussed as possible origin of the observed large intensity enhancement.

A model based on rate equations for a simplified energy level scheme similar to [158] was developed, including only the three states of Er^{3+} that are involved in the energy transfer, labeled by $|0\rangle$, $|1\rangle$ and $|2\rangle$ in Fig. B.1 b), and two states of Yb^{3+}. Ground state and excited state absorption were neglected of Er^{3+} because of the much higher doping

concentration of Yb^{3+} and its about 10 times higher absorption cross section [159, 160]. Also back-energy transfer from Er^{3+} to $Yb^{3+}$was neglected. The rate equations are then solved for the steady state and the weak excitation regime (see Sec. B.5.2). The following expression for the signal enhancement for a single sensitizer-activator pair is obtained:

$$\frac{I_{NF}}{I_{FF}} = f_{10}^4 \frac{c_{10}}{c_{10}^{tip}} \frac{\eta_{20}^{tip}}{\eta_{20}} \left(\frac{k_{ET}^{tip}}{k_{ET}}\right)^2 \frac{(w_{10} + k_{ET} n_{all})^2}{(w_{10}^{tip} + k_{ET} n_{all})^2} \approx f_{10}^4 \frac{c_{10}}{c_{10}^{tip}} \frac{\eta_{20}^{tip}}{\eta_{20}} \tag{B.1}$$

Here, f_{10} denotes the enhancement factor for the excitation of Yb^{3+}, c_{10} the decay rate of the Er^{3+} intermediate state ($^4I_{11/2}$), w_{10} the decay rate of the Yb^{3+} excited state ($^2F_{5/2}$), η_{20} the quantum efficiency of the emitting Er^{3+} state ($^4S_{3/2}$,$^2H_{11/2}$ or $^4F_{9/2}$), k_{ET} the energy transfer rate and n_{all} the population of all levels of Er^{3+}. As in [158] the decay from the emitting to the intermediate state is neglected, i. e. $c_{21} = 0$. The superscript "tip" indicates the presence of the tip. Assuming that the tip does not influence the energy transfer rate k_{ET} [161] and that the transfer is fast, i. e. k_{ET} is large compared to w_{10}, the decay of the long living excited Yb^{3+} state, the last factor in the first expression of Eqn. B.1 can be set to one. At first glance, the enhancement seems to scale with the fourth power of the absorption enhancement factor f_{10} as expected for a two-photon process. However, the excitation enhancement competes with an enhanced depopulation of the $^4I_{11/2}$ level of Er^{3+} and the $^2F_{5/2}$ level of Yb^{3+}. The latter effect is less pronounced and can be neglected because the energy transfer is assumed to be fast and efficient such that most of the Yb^{3+} ions relax via energy transfer and not radiatively. The former process is accounted for by the factor $\frac{c_{10}}{c_{10}^{tip}}$ in Eqn. B.1. If there are no non-radiative losses, this expression yields $1/f_{10}^2$ leading to a quadratic dependence of the signal enhancement on the enhancement factor f_{10}, similar to fluorescence based on one-photon absorption.

Assuming that the Yb^{3+} and Er^{3+} ions do not interact with ions of the same species, Eqn. B.1 is also valid for the whole nanocrystal consisting of many ions. Using the obtained approximated expression given in Eqn. B.1 the experimentally observed enhancement was estimated. Therefore, approximated values for the quantum efficiency $\eta_{20} \approx 7\%$ (green emission) and $\eta_{10} \approx 30\%$ [162] were used and the ratios $\frac{\eta_{20}^{tip}}{\eta_{20}}$ and $\frac{c_{10}}{c_{10}^{tip}}$ were calculated assuming a typical enhancement factor of about $f_{10} \approx 3$ for the excitation in the near-infrared and $f_{20} \approx 5$ for the visible for standard tips [21]. Inserting these values, into Eqn. Eqn. B.1 a value of about $\frac{I_{NF}}{I_{FF}} \approx 222$ for the near-field to far-field intensity ratio was obtained. Here, the excitation rate enhancement described by the factor $f_{10}^4 \frac{c_{10}}{c_{10}^{tip}} \approx 23.8$ in Eqn. B.1 was more than twice as large as the radiative rate enhancement given by $\frac{\eta_{20}^{tip}}{\eta_{20}} \approx 9.3$.
The value $\frac{I_{NF}}{I_{FF}} \approx 222$ is in the range of the volume normalized intensity ratio estimated for the green emission above ($66 \leq \frac{I_{NF}}{I_{FF}} \frac{V_{FF}}{V_{NF}} \leq 555$). In reality, the energy landscape will be far more complex than the simplified scheme depicted in Fig. B.1 b). Nonetheless, this

simplified model shows, that the two-photon process combined with high field enhancement factors could in principle explain the observed large signal enhancement.

B.3.3. Discussion of homo-energy transfer

However, the model is valid for isolated sensitizer-activator pairs only and neglects coupling among emitters of the same species. In the following, it is investigated if energy migration, i. e. energy transfer among Yb^{3+} or Er^{3+} within a single nanocrystal, could play a role.
In fact, the large signal enhancement can also be understood considering the size and composition of the doped nanocrystals. The high doping concentrations of both types of ions, $c(Yb^{3+}) = 20\%$ and $c(Er^{3+}) = 2\%$, could allow for an efficient energy transfer not only between the Yb^{3+} and Er^{3+} ions (hetero-transfer), but also between the Yb^{3+} and Er^{3+} ions themselves (homo-transfer) leading to energy migration within the nanocrystal [163]. After locally enhanced excitation in the vicinity of the tip, the electronic energy could be distributed over a larger nanocrystal volume. On the other hand, in the case of efficient transfer, an extended volume could benefit from tip-induced radiative rate enhancement. Energy migration would thus lead to a non-local signal contribution complicating the image contrast formation and the discussion of the signal enhancement.
For Yb^{3+} homo-transfer the Förster radius is 2.1 nm, although calculated for a different nanocrystal matrix [164], but substantially larger than the average ion distance of 0.5 nm (see Sec. B.5.3) at the present doping concentration. For Er^{3+} homo-transfer Förster radii between 1.0 and 1.8 nm are reported depending on the matrix and transitions [165–167], comparable to the mean ion distance of 1 nm. The Förster radius for the present activator - sensitizer combination is reported to range between 1.5 and 2.0 nm [164].
With these values the range of energy migration between the identical ions by calculating the root mean square displacement (*rmsd*) using a 3D random walk model was estimated. The *rmsd* for a diffusive process in three dimensions is given by $\sqrt{< x^2(t) >} = \sqrt{6Dt}$, where D is the diffusion coefficient depending on the mean ion distance and the energy transfer rate, and t the time after which the *rmsd* is evaluated. The details of the calculation can be found in Sec. B.5.4. The *rmsd* depends strongly on the Förster radii and the mean ion distances, since the transfer rate scales with the sixth power of their ratio. Therefore, an uncertainty for both values of 0.2 nm was accounted for and lower and upper boundaries for the *rmsd* were estimated.
Assuming a range of 1.9-2.3 nm for the Förster radius and 0.3-0.7 nm for the mean ion separation a *rmsd* ranging from 4 to 50 nm is obtained in the case of energy transfer between Yb^{3+} ions. For Er^{3+} ions, smaller values between 3 and 25 nm are obtained using the given range of Förster radii and an uncertainty of the mean distance of 0.2 nm as for Yb^{3+}. Due to the larger ion separation and the smaller Förster radius, homo-transfer between Er^{3+} ions is not as efficient as between Yb^{3+} ions. Hence, depending on the exact values for the ion distances and Förster radii, the nanocrystal volume affected by energy migration can become comparable or even larger than the volume probed in the near-field.

For the lower limit of 4 and 3 nm, respectively, the influence of energy migration will be negligible and the signal enhancement can be calculated according to Eqn. B.1. Discussing the upper limit of the migration range the following was found. After locally enhanced excitation of mainly the Yb^{3+} ions due to their stronger absorption in the vicinity of the tip, the electronic energy could migrate for up to 50 nm exceeding the near-field interaction range. Since the migration range for the emitting Er^{3+} ions is shorter (25 nm vs. 50 nm), radiative rate enhancement would thus affect not all excited states created by near-field excitation. On the other hand, energy migration between Er^{3+} ions always results in a larger total number of ions benefiting from radiative rate enhancement as compared to the situation without transfer due to the confocal excitation within the migration range. The discussion shows the complex interplay between energy transfer processes and the excitation and emission rate enhancement.

B.3.4. Time-resolved measurements

The study was complemented by time-resolved measurements that are shown in Fig. B.3. The recorded PL transients for both detection energies (Fig. B.3 c) and d)) show a significantly faster decay in the presence of the tip. Since a continuous signal enhancement is observed for decreasing tip-sample distances (Fig. B.3 b)) without indications of metal-induced PL quenching even for the smallest distances achieved in the experiment, the lifetime reduction can be assigned to tip-induced radiative rate enhancement. The transients recorded for the red emission show an even stronger decrease of the lifetime that can be ascribed to a wavelength dependent radiative rate enhancement of the tip. This is also seen in the PL spectra shown in Fig. B.3 a). The quantitative values for the lifetimes are determined by biexponential fits, yielding an intensity-weighted average lifetime for the red emission of about $\tau = 110\,\mu s$ without tip, $\tau^{tip} = 42\,\mu s$ with tip, respectively. The time-resolved measurements support the idea of homo-energy transfer. Transients detected in the presence of the tip (Fig. B.3 d)) do not show a substantial remaining slow component on the order of 110 µs that would be expected in the absence of homo-energy transfer between the ions. This indicates that the local tip-induced radiative rate enhancement could lead to a faster relaxation of the emissive states within a larger volume.

B.3.5. Influence of the tip geometry on the image contrast formation

After the discussion of the two-photon process and the role of homo-energy transfer it is now focused on the influence of the nanocrystal topography on TENOM images. As noted above, the decay length of the enhanced field is limited to about 10-15 nm [168]. While the TENOM signal would thus increase for increasing sample thickness, it is expected to saturate for structures higher than 10-15 nm or in the presence of efficient homo-energy transfer. Indeed, the near-field up-conversion PL image and the cross section shown in Fig. B.2 a) and c), respectively, showed this behavior. Plateau-type PL images were also observed for other nanocrystals (Fig. B.4 a) and d)). For red emission recorded with the same tip, how-

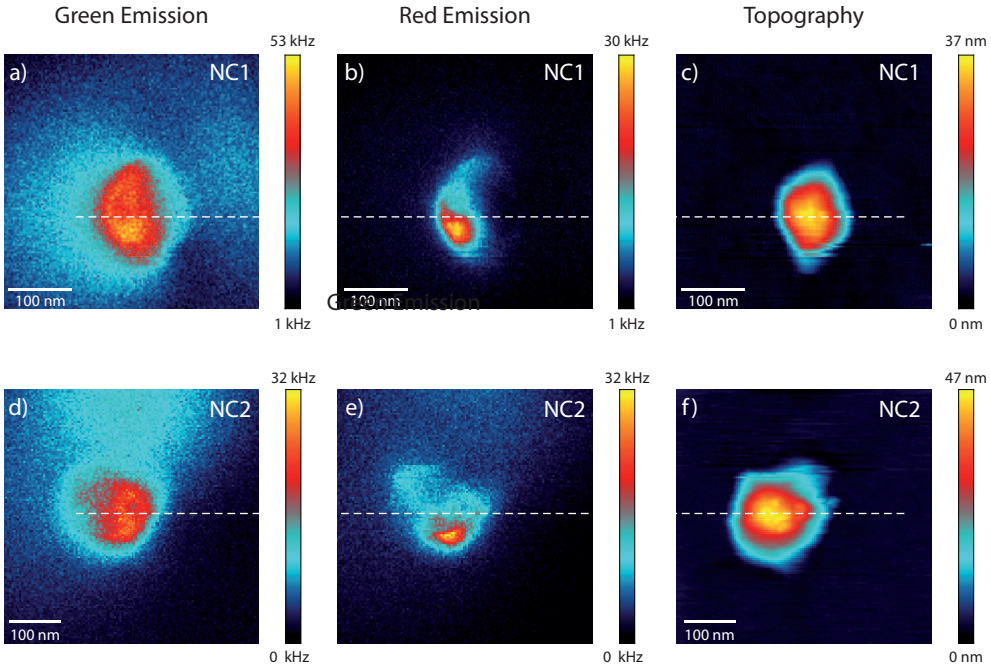

Fig. B.4. Simultaneously recorded topography (c,f) and tip-enhanced up-conversion photoluminescence images (a, b, d, e) for two different nanocrystals. The red emission shows a stronger image contrast than the green emission, indicating a stronger signal enhancement for the red wavelength. Both nanocrystals show a non-uniform spatial distribution of the enhanced PL that is localized at the lower nanocrystal edge for the red emission.

ever, the image contrast turned out to be very different (Fig. B.4 b) and e)). It appeared that while the whole nanocrystals are seen in the near-field image, additional strong enhancement occurred localized at their lower edges. Since ion-doping was uniform, the field enhancement at the tip is assumed to be spatially asymmetric. In general, this asymmetry could result from the tip fabrication by electrochemical etching and from tip wear during scanning. Because extended sample structures interact with a larger part of the tip, the resulting influence on the image contrast is expected to be more pronounced than for thin structures that only interact with the foremost part of the tip.

To clarify the influence of the tip on the near-field images further, the image contrast for the nanocrystal NC1 (Fig. B.4 (a-c)) using a different tip was studied. Both optical and topographic images are very different as illustrated in Fig. B.5. As can be seen from the images in Fig. B.5 a) and b) and in particular from the cross sections Fig. B.5 d), the intensity is localized at the nanocrystal edges while it disappears in the center. Based on the apparent larger topographic width of the nanocrystal and it somewhat irregular shape, it is concluded that the tip used was broader and less defined. Given the uniform ion doping and the comparison with Fig. B.4 (a-c), the vanishing PL intensity in the center of the nanocrystal must be an artifact. Interestingly, a similar enhancement and image contrast for red and green emission was observed in this case. As for scanning probe techniques in general, irregular tip shapes can lead to imaging artifacts that will become

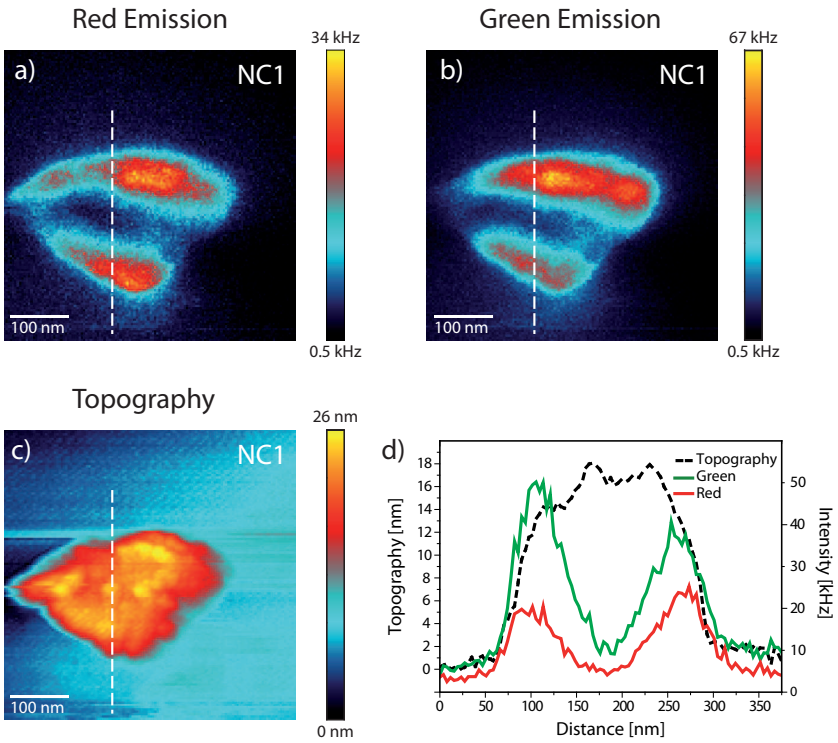

Fig. B.5. Simultaneously recorded tip-enhanced up-conversion photoluminescence images for the a) ${}^4F_{9/2} \rightarrow {}^4 I_{15/2}$ and b) ${}^4S_{3/2}, {}^2H_{11/2} \rightarrow {}^4 I_{15/2}$ transition of nanocrystal NC1 (Fig. B.4 (a-c)) with another tip. The scan direction is rotated by 55° with respect to Fig. B.4 (a-c). The intensity distribution and image contrast is similar for both wavelengths. c) Simultaneously taken topography image. Comparing this image with the topography image recorded with the first tip shown in Fig. B.4 c, it is concluded that this tip is broader and less defined. e) PL - and topographic cross-sections along the white dashed line in a)-c). The enhanced PL is strongest at the nanocrystal edges and nearly disappears in the center. Since ion-doping is assumed to homogeneous the observed intensity distribution needs to be an artifact resulting from the particular tip shape.

particularly relevant for larger sample structures. TENOM experiments on higher samples should thus be reproduced and tested with several tips.

B.4. Summary

In summary, tip-enhanced up-conversion PL of rare-earth ion-doped nanocrystals were presented. Near-field images of single nanocrystals showed clear sub-diffraction resolution. Time-resolved PL measurements together with tip-sample distance curves demonstrated the contribution of radiative rate enhancement. The experimentally measured near-field to far-field intensity ratios were compared to theoretically predicted values. Therefor, an expression for the enhancement for two-photon absorption based on the rate equations using a simplified energy level system was derived. It was found that for large enhancement factors this model predicts signal enhancements of the same order of magnitude of the experimentally determined values. Considering the ion doping levels we also suggested a non-local contribution to the tip-enhanced signal caused by efficient non-radiative homo-energy transfer between the ions in the nanocrystals. In this way, emitters in a volume

larger than the near-field interaction volume can benefit from radiative rate enhancement. Comparison between different nanocrystals and tips showed a strong influence of the tip shape that could lead to imaging artifacts. The studies clearly showed that TENOM can be applied to larger sample structures, while the image contrast needs to be interpreted carefully.

B.5. Calculation details

B.5.1. Influence of the tip geometry on the measured topography profile

The influence of the tip geometry on the measured topographic width was estimated by simple geometric considerations. The problem in 2D is illustrated in Fig. B.6 showing the tip with radius r and opening angle α. In order to have a geometric configuration as simple as possible, the crystal shape was approximated as shown in the sketch. Its endings were assumed to be half spheres with radius R. The same geometry applies to the slow scan direction.

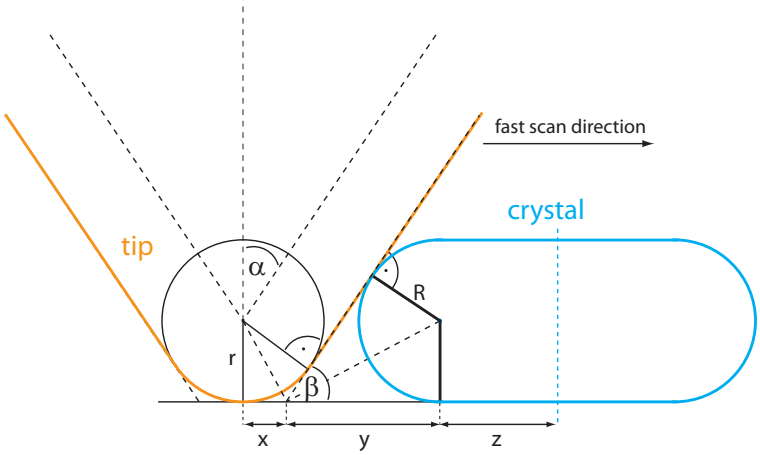

Fig. B.6. Simplified geometric configuration of the AFM measurement for the fast scan direction. The tip with opening angle α and radius r is shown in yellow. The shape of the nanocrystal depicted in blue is approximated by assuming spherical endings with radius R. Using this geometry, the influence of the tip diameter and opening angle on the measured topography profile can be estimated.

The measured topographic width w for this configuration is given by

$$w = 2 \cdot (x + y + z), \tag{B.2}$$

with x, y and z being the distances depicted in Fig. B.6.
From trigonometry it follows that

$$x = \frac{r}{\tan\left(\frac{180°-\beta}{2}\right)} \tag{B.3}$$

$$y = \frac{R}{\tan\left(\frac{\beta}{2}\right)}. \tag{B.4}$$

Between α and β the relation

$$\beta = 90° - \alpha \tag{B.5}$$

holds. An opening angle of $\alpha = 45°$ and radius of $r = 30\,\text{nm}$ were assumed, values that are rather large for standard tips. For these values, the lateral dimension given by $2(R + z)$ that a nanocrystal must have in order to yield a measured topographic width of 200 nm were calculated using Eqn. B.2 to Eqn. B.5. As a result for the minimum lateral extension of a nanocrystal a value of 120 nm was obtained leading to a crystal volume of $390 \cdot 10^3\,\text{nm}^3$.

B.5.2. Rate equations

According to the level scheme in Fig. B.7 the following rate equations can be set up:

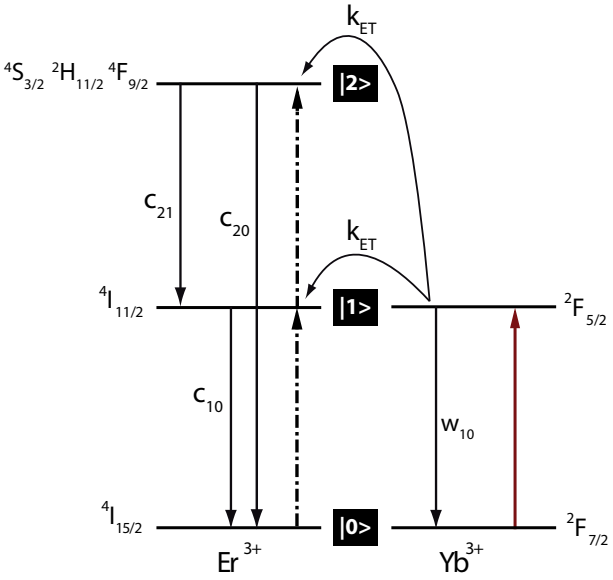

Fig. B.7. Simplified energy level system showing the transitions that are included in the model. The transition rates are denoted by w_{ij} and c_{ij} for transitions from level j to level i in Yb^{3+}, Er^{3+}, respectively. k_{ET} is the Förster energy transfer rate.

$$\frac{\partial N_0}{\partial t} = -N_0\frac{\sigma_{10}I}{\hbar\omega_{10}} + N_1 w_{10} + N_1 n_0 k_{ET} + N_1 n_1 k_{ET} \tag{B.6}$$

$$\frac{\partial n_0}{\partial t} = n_1 c_{10} + n_2 c_{20} - N_1 n_0 k_{ET} \tag{B.7}$$

$$\frac{\partial n_1}{\partial t} = -n_1 c_{10} + N_1 n_0 k_{ET} - N_1 n_1 k_{ET} \tag{B.8}$$

$$\frac{\partial n_2}{\partial t} = -n_2 c_{20} + N_1 n_1 k_{ET} \tag{B.9}$$

N_i (n_i) denotes the population of level i of Yb^{3+} (Er^{3+}). The transition rates w_{ij} and c_{ij} are illustrated in Fig. B.7 and k_{ET} is the Förster energy transfer rate. N_{all} (n_{all}) is the population of all levels, i. e. $N_{all} = N_1 + N_2$ ($n_{all} = n_0 + n_1 + n_2$). The absorption rate for Yb^{3+} is given by $\frac{\sigma_{10}\, I}{\hbar\omega_{10}}$, where σ_{10} is the absorption cross section, $\hbar\omega_{10}$ the photon energy and I the locally enhanced intensity, that is proportional to the square of the field enhancement factor f_{10}. Setting up these equations, the following approximations similar to [158] were made: first, the absorption of Er^{3+} was neglected due to a much smaller absorption cross section [159, 160] and a lower doping concentration compared to Yb^{3+} and second, c_{21} was considered to be small and therefore was neglected. For steady state conditions, as present under cw-illumination, all time derivatives were set to zero. Furthermore, in the weak excitation regime, $N_0 \approx N_{all} \gg N_1$ and $n_0 \approx n_{all} \gg n_1, n_2$ holds. Terms proportional to n_0 and N_0 are thus considered as large compared to others. The fourth term in (B.6), the second in (B.7) and the third in (B.8) can therefore be neglected.
Under these conditions, it follows from (B.6) to (B.8)

$$N_1 \approx \frac{\sigma_{10} I N_{all}}{\hbar\omega_{10}(w_{10} + k_{ET} n_0)} \tag{B.10}$$

$$n_1 \approx \frac{k_{ET} N_1 n_{all}}{c_{10}} \tag{B.11}$$

Solving (B.9) for n_2 and inserting (B.10) and (B.11) yields

$$n_2 \propto \frac{k_{ET}^2 I^2}{c_{10} c_{20} (w_{10} + k_{ET} n_{all})^2}. \tag{B.12}$$

The emitted power is then proportional to $n_2 \cdot c_{20}^{rad}$. The dependence of n_2 on the square of the intensity in (B.12) arises from the two-photon absorption process. Because I^2 scales with the fourth power of the field enhancement factor, $I^2 \propto f_{10}^4$, the following near-field to far-field intensity ratio was obtained

$$\frac{I_{NF}}{I_{FF}} = f_{10}^4 \frac{c_{10}}{c_{10}^{tip}} \frac{\eta_{20}^{tip}}{\eta_{20}} \left(\frac{k_{ET}^{tip}}{k_{ET}}\right)^2 \left(\frac{w_{10} + k_{ET} n_{all}}{w_{10}^{tip} + k_{ET}^{tip} n_{all}}\right)^2. \tag{B.13}$$

Here, the relation $\eta_{20} = \frac{c_{20}^{rad}}{c_{20}}$ was used. By neglecting the influence of the tip on the transfer rate k_{ET}, [161] and by assuming a fast energy transfer compared to the lifetime of the Yb^{3+} excited state, i. e. $k_{ET} n_{all} \gg w_{10}$, it follows that

$$\frac{I_{NF}}{I_{FF}} = f_{10}^4 \frac{c_{10}}{c_{10}^{tip}} \frac{\eta_{20}^{tip}}{\eta_{20}}. \tag{B.14}$$

While the model used has analogies with the one developed in [158], Yb^{3+} and Er^{3+} were not considered to be in a fast equilibrium and therefore assumed different decay rates w_{10} and c_{10} for Yb^{3+} and Er^{3+}. In addition, population and depopulation due to energy transfer were included, i. e. terms proportional to the transfer rate k_{ET}, in the rate equations. As a consequence, the expression for the near-field to far-field intensity ratio ((B.14)) differs from the expression derived in [158]. In the absence of non-radiative losses, i. e. $c_{10}^{tip} = c_{10}^{tip,rad} = f_{10}^2 c_{10}$, (B.14) still leads to an excitation enhancement proportional to f_{10}^2, whereas in [158] no further excitation enhancement is achieved.

B.5.3. Calculation of the mean ion distances

The mean ion distances for Yb^{3+} and Er^{3+} were calculated from the doping concentrations and the unit cell parameters. The number of atoms in the unit cell of undoped $NaYF_4$ is 8 for F, 2 for Na, 2 for Y. During the doping process, 2% of the Y atoms were subsituted by Er and 20% by Yb atoms. Therefore, the unit cell of doped $NaYF_4$ consists of 0.04 Er, 0.4 Yb and 1.56 Y atoms. The volume of the unit cell V_{UC} were calculated based on the lattice constant a that is known to be 0.547 nm [169]. From the unit cell volume the volume occupied by one Er and Yb atom was calculated by $V_{Er} = V_{UC}/0.04$ and $V_{Yb} = V_{UC}/0.4$. From these volumes the mean average distances were determined as

$$r_{Er} = \sqrt[3]{\frac{3V_{Er}}{4\pi}} \tag{B.15}$$

$$r_{Yb} = \sqrt[3]{\frac{3V_{Yb}}{4\pi}}. \tag{B.16}$$

Using these equations, mean ion distances of r_{Er}=1.0 nm and r_{Yb}= 0.50 nm were obtained.

B.5.4. Calculation of the root mean square displacement treating the energy transfer process as a random walk in three dimensions

Considering the energy transfer as a diffusive process, the root mean square displacement in three dimensions can be calculated by

$$\sqrt{< x^2(t) >} = 6Dt. \tag{B.17}$$

Here, D is the diffusion coefficient that is given by

$$D = \frac{r^2}{2\tau}, \tag{B.18}$$

where r is the mean distance between two events, i. e. the mean ion separation. τ denotes the average time between two events, i. e. two energy transfer processes given by the inverse Förster transfer rate k_{ET}. k_{ET} can be calculated by

$$k_{ET} \approx N \cdot \frac{1}{\tau_0} \frac{r_0^6}{r^6}. \tag{B.19}$$

r_0 is the Förster radius for the transition involved in the energy transfer and τ_0 the lifetime of the excited state of the same transition in the absence of the activator. N accounts for the number of intermediate neighbours of every ion and is 6 for the cubic lattice structure. Energy transfer to ions others than next neighbours were neglected.
The following values for the estimation of the root mean square displacement were used:

	r_0	r	τ_0	t
Yb^{3+}	1.9-2.1 nm	0.3-0.7 nm	1.4 ms [164]	10 µs
Er^{3+}	1.2-2.0 nm	0.8-1.2 nm	0.4 ms [170]	100 µs

The values for τ_0 were taken from the references indicated and might be slightly different for the nanocrystals used. For Yb^{3+} it is the lifetime of the ${}^2F_{5/2} \rightarrow {}^2F_{7/2}$ transition, for Er^{3+} the ${}^4F_{9/2} \rightarrow {}^4I_{15/2}$ transition that corresponds to the emissive state at 660 nm was chosen. Energy transfer between other states can also occur but was not considered in the model.
The values for t, the time for which the *rmsd* was evaluated was different for both transfers. A value of 10 µs was used for Yb^{3+} i. e. the time needed to populate the ${}^4F_{9/2}$ state and corresponds to the rise time in the transient shown in Fig. B.3 d). For Er^{3+} a value of 100 µs was used, that is the approximate lifetime of the ${}^4F_{9/2}$ state determined from the same transient.
Inserting all values into (B.19), (B.18) and (B.17) yields a range for the root mean square displacements for Yb^{3+} and Er^{3+} of 4-50 nm and 3-25 nm.

Bibliography

[1] N. P. Guisinger and M. S. Arnold, "Beyond silicon: carbon-based nanotechnology," MRS Bulletin **35**, 273–279 (2010).

[2] R. Arghavani and H. M'saad, Solid State Technology, May (2008).

[3] M. Bohr and K. Mistry, "Intel's revolutionary 22 nm transistor technology," http://download.intel.com/newsroom/kits/22nm/pdfs/22nm - details_presentation.pdf (27.08.2014).

[4] S. J. Tans, A. R. M. Verschueren, and C. Dekker, "Room-temperature transistor based on a single carbon nanotube," Nature **393**, 49–51 (1998).

[5] R. Martel, T. Schmidt, H. R. Shea, T. Hertel, and P. Avouris, "Single- and multi-wall carbon nanotube field-effect transistors," Appl. Phys. Lett. **73**, 2447–2449 (1998).

[6] M. M. Shulaker, G. Hills, N. Patil, H. Wei, H.-Y. Chen, H.-S. P. Wong, and S. Mitra, "Carbon nanotube computer," Nature **501**, 526–530 (2013).

[7] M. Freitag, Y. Martin, J. A. Misewich, R. Martel, and P. Avouris, "Photoconductivity of single carbon nanotubes," Nano Letters **3**, 1067–1071 (2003).

[8] M. S. Arnold, J. L. Blackburn, J. J. Crochet, S. K. Doorn, J. G. Duque, A. Mohite, and H. Telg, "Recent developments in the photophysics of single-walled carbon nanotubes for their use as active and passive material elements in thin film photovoltaics," Phys. Chem. Chem. Phys. **15**, 14896–14918 (2013).

[9] J. Chen, V. Perebeinos, M. Freitag, J. Tsang, Q. Fu, J. Liu, and P. Avouris, "Bright infrared emission from electrically induced excitons in carbon nanotubes," Science **310**, 1171–1174 (2005).

[10] L. Marty, E. Adam, L. Albert, R. Doyon, D. Ménard, and R. Martel, "Exciton formation and annihilation during 1D impact excitation of carbon nanotubes," Phys. Rev. Lett. **96**, 136803 (2006).

[11] C. M. Aguirre, S. Auvray, S. Pigeon, R. Izquierdo, P. Desjardins, and R. Martel, "Carbon nanotube sheets as electrodes in organic light-emitting diodes," Appl. Phys. Lett. **88**, 183104 (2006).

[12] C. Wang, J. L. Zhang, K. M. Ryu, A. Badmaev, L. G. De Arco, and C. W. Zhou, "Wafer-scale fabrication of separated carbon nanotube thin-film transistors for display applications," Nano Lett. **9**, 4285–4291 (2009).

[13] Y. M. Chien, F. Lefevre, I. Shih, and R. Izquierdo, "A solution processed top emission OLED with transparent carbon nanotube electrodes," Nanotechnol. **21**, 134020 (2010).

[14] S. J. Tans and C. Dekker, "Potential modulations along carbon nanotubes," Nature **404**, 834–835 (2000).

[15] M. Freitag, M. Radosavljevic, Y. Zhou, A. Johnson, and W. F. Smith, "Controlled creation of a carbon nanotube diode by a scanned gate," Appl. Phys. Lett. **79**, 3326–3328 (2001).

[16] Y. Kim, Y. M. Oh, J.-Y. Park, and S.-J. Kahng, "Mapping potential landscapes of semiconducting carbon nanotubes with scanning gate microscopy," Nanotechnol. **18**, 475712 (2007).

[17] A. Bachtold, M. S. Fuhrer, S. Plyasunov, M. Forero, E. H. Anderson, A. Zettl, and P. L. McEuen, "Scanned probe microscopy of electronic transport in carbon nanotubes," Phys. Rev. Lett. **84**, 6082–6085 (2000).

[18] Y. Miyato, K. Kobayashi, K. Matsushige, and H. Yamada, "Surface potential investigation on single wall carbon nanotubes by Kelvin probe force microscopy and atomic force microscope potentiometry," Nanotechnol. **18**, 084008 (2007).

[19] T. Umesaka, H. Ohnaka, Y. Ohono, S. Kishimoto, K. Maezawa, and T. Mizutani, "Surface potential measurement of carbon nanotube field-effect transistors using Kelvin probe force microscopy," Jpn. J. Appl. Phys. **46**, 2496–2500 (2007).

[20] A. Hartschuh, "Tip-enhanced near-field optical microscopy," Angew. Chem. Int. Ed. **47**, 8178–8191 (2008).

[21] M. Böhmler, N. Hartmann, C. Georgi, F. Hennrich, M. C. Hersam, and A. Hartschuh, "Enhancing and redirecting carbon nanotube photoluminescence by an optical antenna," Opt. Express **18**, 16443–16451 (2010).

[22] C. Georgi, A. A. Green, M. C. Hersam, and A. Hartschuh, "Probing exciton localization in single-walled carbon nanotubes using high-resolution near-field microscopy," ACS Nano **4**, 5914–5920 (2010).

[23] C. Georgi, "Exciton mobility and localized defects in single carbon nanotubes studied with tip-enhanced near-field optical microscopy," Ph.D. thesis, Ludwig-Maximilians-Universität München (2011).

[24] J. Stadler, T. Schmid, and R. Zenobi, "Nanoscale chemical imaging of single-layer graphene," ACS Nano **5**, 8442–8448 (2011).

[25] W. Su and D. Roy, "Visualizing graphene edges using tip-enhanced Raman spectroscopy," J. Vac. Sci. Technol. B **31**, 041808 (2013).

[26] J. Steidtner and B. Pettinger, "Tip-enhanced Raman spectroscopy and microscopy on single dye molecules with 15 nm resolution," Phys. Rev. Lett. **100**, 236101 (2008).

[27] T. H. Taminiau, F. D. Stefani, F. B. Segerink, and N. F. van Hulst, "Optical antennas direct single-molecule emission," Nat. Photon. **2**, 234–237 (2008).

[28] W. Bao, M. Melli, N. Caselli, F. Riboli, D. S. Wiersma, M. Staffaroni, H. Choo, D. F. Olgetree, S. ALoni, J. Bokor, S. Cabrini, F. Intonti, M. B. Salmeron, E. Yablonovitch, P. J. Schuck, and A. Weber-Bargioni, "Mapping local charge recombination heterogeneity by multidimensional nanospectroscopic imaging," Science **338**, 1317–1321 (2012).

[29] M. Böhmler, Z. Wang, A. Myalitsin, A. Mews, and A. Hartschuh, "Optical imaging of CdSe nanowires with nanoscale resolution," Angew. Chem. Int. Ed. **50**, 11536 (2011).

[30] M. Böhmler and A. Hartschuh, "Tip-enhanced near-field optical microscopy of single quasi-1D nanostructures," Chem. Phys. Chem. **13**, 927–929 (2012).

[31] S. Berweger, C. C. Neacsu, Y. Mao, H. Zhou, S. S. Wong, and M. B. Raschke, "Optical nanocrystallography with tip-enhanced phonon Raman spectroscopy," Nat. Nanotechnol. **4**, 496–499 (2009).

[32] E. Bailo and V. Deckert, "Tip-enhanced Raman spectroscopy of single RNA strands: towards a novel direct-sequencing method," Angew. Chem. Int. Ed. **47**, 1658–1661 (2008).

[33] M. Paulite, C. Blum, T. Schmid, L. Opilik, K. Eyer, G. C. Walker, and R. Zenobi, "Full spectroscopic tip-enhanced Raman imaging of single nanotapes formed from β-amyloid(1-40) peptide fragments," ACS Nano **7**, 911–920 (2013).

[34] B. R. Wood, M. Asghari-Khiavi, E. Bailo, D. McNaughton, and V. Deckert, "Detection of nano-oxidation sites on the surface of hemoglobin crystals using tip-enhanced Raman scattering," Nano Lett. **12**, 1555–1560 (2012).

[35] C. Georgi and A. Hartschuh, "Tip-enhanced Raman spectroscopic imaging of localized defects in carbon nanotubes," Appl. Phys. Lett. **97**, 143117 (2010).

[36] N. Anderson, A. Hartschuh, and L. Novotny, "Chirality changes in carbon nanotubes studied with near-field Raman spectroscopy," Nano Lett. **7**, 577–582 (2007).

[37] H. Qian, P. T. Araujo, C. Georgi, T. Gokus, N. Hartmann, A. A. Green, A. Jorio, M. C. Hersam, L. Novotny, and A. Hartschuh, "Visualizing the local optical response of semiconducting carbon nanotubes to DNA-wrapping," Nano Lett. **8**, 2706–2711 (2008).

[38] H. Qian, C. Georgi, N. Anderson, A. A. Green, M. C. Hersam, L. Novotny, and A. Hartschuh, "Exciton energy transfer in pairs of single-walled carbon nanotubes," Nano Lett. **8**, 1363–1367 (2008).

[39] T. Yano, P. Verma, Y. Saito, T. Ichimura, and S. Kawata, "Pressure-assisted tip-enhanced Raman imaging at a resolution of a few nanometres," Nat. Photon. **3**, 473–477 (2009).

[40] M. Scarselli, P. Castrucci, and M. De Crescenzi, "Electronic and optoelectronic nano-devices based on carbon nanotubes," J. Phys.: Condens. Matter **24**, 313202 (2012).

[41] K. S. Novoselov, A. K. Geim, S. V. Morozov, D. Jiang, Y. Zhang, S. V. Dubonos, I. V. Grigorieva, and A. A. Firsov, "Electric field effect in atomically thin carbon films," Science **306**, 666–669 (2004).

[42] S. Iijima, "Helical microtubules of graphitic carbon," Nature **354**, 56–58 (1991).

[43] S. Iijima and T. Ichihashi, "Single-shell nanotubes of 1-nm diameter," Nature **363**, 603–605 (1993).

[44] A. Jorio, M. S. Dresselhaus, and G. Dresselhaus, eds., *Carbon nanotubes*, vol. 111 of *Topics in Applied Physics* (Springer, Berlin / Heidelberg, 2008).

[45] M. S. Dresselhaus, G. Dresselhaus, R. Saito, and A. Jorio, "Raman spectroscopy of carbon nanotubes," Phys. Reports **409**, 47–99 (2006).

[46] R. Saito, G. Dresselhaus, and M. S. Dresselhaus, *Physical properties of carbon nanotubes* (Imperial College Press, London, 1998).

[47] S. Reich, C. Thomsen, and J. Maultzsch, *Carbon nanotubes: basic concepts and physical properties* (Wiley-VCH, Berlin, 2004).

[48] J. Svensson and E. E. B. Campbell, "Schottky barriers in carbon nanotube-metal contacts," J. Appl. Phys. **110**, 111101 (2011).

[49] T. Ando, "Excitons in carbon nanotubes," J. Phys. Soc. Jap. **66**, 1066–1073 (1997).

[50] F. Wang, G. Dukovic, L. E. Brus, and T. H. Heinz, "The optical resonances in carbon nanotubes arise from excitons," Science **308**, 838–841 (2005).

[51] C. Manzoni, A. Gambetta, E. Menna, M. Meneghetti, G. Lanzani, and G. Cerullo, "Intersubband exciton relaxation dynamics in single-walled carbon nanotubes," Phys. Rev. Lett. **94**, 207401 (2005).

[52] R. B. Weisman and S. M. Bachilo, "Dependence of optical transition energies on structure for single-walled carbon nanotubes in aqueous suspension:an empirical Kataura plot," Nano Letters **3**, 1235–1238 (2003).

[53] H. Ajiki and T. Ando, "Carbon nanotubes: optical absorption in Aharonov-Bohm flux," Jpn. J. Appl. Phys. **34**, 107–109 (1995).

[54] G. S. Duesberg, I. Loa, M. Burghard, K. Syassen, and S. Roth, "Polarized Raman spectroscopy on isolated single-wall carbon nanotubes," Phys. Rev. Lett. **2000**, 5436–5439 (85).

[55] P. T. Araujo, I. O. Maciel, P. B. C. Pesce, M. A. Pimenta, S. K. Doorn, H. Qian, A. Hartschuh, M. Steiner, L. Grigorian, K. Hata, and A. Jorio, "Nature of the constant factor in the relation between radial breathing mode frequency and tube diameter for single-wall carbon nanotubes," Phys. Rev. B **77**, 241403 (2008).

[56] J. S. Soares, L. G. Cançado, E. B. Barros, and A. Jorio, "The Kataura plot for single wall carbon nanotubes on top of crystalline quartz," Phys. Stat. Sol. B **247**, 2835–2837 (2010).

[57] S. Ilani and P. L. McEuen, "Electron transport in carbon nanotubes," Annu. Rev. Condens. Matter Phys. **1**, 1–25 (2010).

[58] J.-C. Charlier, X. Blase, and S. Roche, "Electronic and transport properties of nanotubes," Rev. Mod. Phys. **79**, 677–732 (2007).

[59] P. Avouris, "Electronics with carbon nanotubes," Physics World **20**, 40–45 (2007).

[60] P. Avouris, Z. Chen, and V. Perebeinos, "Carbon-based electronics," Nat. Nanotechnol. **2**, 605–615 (2007).

[61] P. Avouris and R. Martel, "Progress in carbon nanotube electronics and photonics," MRS Bulletin **35**, 306–313 (2010).

[62] S. Nanot, E. Hároz, J.-H. Kim, R. H. Hauge, and J. Kono, "Optoelectronic properties of single-wall carbon nanotubes," Adv. Mater. **24**, 4977–4994 (2012).

[63] T. Ando and T. Nakanishi, "Impurity scattering in carbon nanotubes: absence of back scattering," J. Phys. Soc. Jap. **67**, 1704–1713 (1998).

[64] C. T. White and T. N. Todorov, "Carbon nanotubes as long ballistic conductors," Nature **393**, 240–242 (1998).

[65] P. L. McEuen, M. Bockrath, D. H. Cobden, Y.-G. Yoon, and S. G. Louie, "Disorder, pseudospins and backscattering in carbon nanotubes," Phys. Rev. Lett. **83**, 5098–5101 (1999).

[66] Z. Yao, C. L. Kane, and C. Dekker, "High-field electrical transport in single-wall carbon nanotubes," Phys. Rev. Lett. **84**, 2941–2944 (2000).

[67] S. R. Naeemi, A. and J. D. Meindl, "Performance comparison between carbon nanotube and copper interconnects for GSI," IEDM Digest pp. 699–702 (2004).

[68] J. U. Lee, P. P. Gipp, and C. M. Heller, "Carbon nanotube p-n junction diodes," Appl. Phys. Lett. **85**, 145–147 (2004).

[69] J. U. Lee, "Photovoltaic effect in ideal carbon nanotube diodes," Appl. Phys. Lett. **87**, 073101 (2005).

[70] C. Zhou, J. Kong, and H. Dai, "Electrical measurements of individual semiconducting single-walled carbon nanotubes of various diameters," Appl. Phys. Lett. **76**, 1597–1599 (2000).

[71] R. Martel, V. Derycke, C. Lavoie, J. Appenzeller, K. K. Chan, J. Tersoff, and P. Avouris, "Ambipolar electrical transport in semiconducting single-wall carbon nanotubes," Phys. Rev. Lett. **87**, 256805 (2001).

[72] S. Heinze, J. Tersoff, R. Martel, V. Derycke, J. Appenzeller, and P. Avouris, "Carbon nanotubes as Schottky barrier transistors," Phys. Rev. Lett. **89**, 106801 (2002).

[73] V. Derycke, R. Martel, J. Appenzeller, and P. Avouris, "Controlling doping and carrier injection in carbon nanotube transistors," Appl. Phys. Lett. **80**, 2773–2775 (2002).

[74] J. Appenzeller, M. Radosavljević, J. Knoch, and P. Avouris, "Tunneling versus thermionic emission in one-dimensional semiconductors," Phys. Rev. Lett. **92**, 048301 (2004).

[75] S. C. Lim, J. H. Jang, D. J. Bae, G. H. Han, S. Lee, I.-S. Yeo, and Y. H. Lee, "Contact resistance between metal and carbon nanotube interconnects: effect of work function and wettability," Appl. Phys. Lett. **95**, 264103 (2009).

[76] Y. Zhang, N. W. Franklin, R. J. Chen, and H. Dai, "Metal coating on suspended carbon nanotubes and its implication to metal-tube interaction," Chem. Phys. Lett. **331**, 35–41 (2000).

[77] Y. Zhang and H. Dai, "Formation of metal nanowires on suspended single-walled carbon nanotubes," Appl. Phys. Lett. **77**, 3015–3017 (2000).

[78] Z. Chen, J. Appenzeller, J. Knoch, Y. Lin, and P. Avouris, "The role of metal-nanotube contact in the performance of carbon nanotube field-effect transistors," Nano Letters **5**, 1497–1502 (2005).

[79] Y. Chen and M. S. Fuhrer, "Tuning from thermionic emission to ohmic tunnel contacts via doping in Schottky-barrier nanotube transistors," Nano Lett. **6**, 2158–2162 (2006).

[80] K. Balasubramanian, Y. Fan, M. Burghard, K. Kern, M. Friedrich, U. Wannek, and A. Mews, "Photoelectronic transport imaging of individual semiconducting carbon nanotubes," Appl. Phys. Lett. **84**, 2400–2402 (2004).

[81] K. Balasubramanian, M. Burghard, K. Kern, M. Scolari, and A. Mews, "Photocurrent imaging of charge transport barriers in carbon nanotube devices," Nano Lett. **5**, 507–510 (2005).

[82] K. Kong, S. Han, and J. Ihm, "Development of an energy barrier at the metal-chain-metallic-carbon-nanotube nanocontact," Phys. Rev. B **60**, 6074–6079 (1999).

[83] T. Hunger, B. Lengeler, and J. Appenzeller, "Transport in ropes of carbon nanotubes: contact barriers and Luttinger liquid theory," Phys. Rev. B **69**, 195406 (2004).

[84] N. M. Gabor, Z. Zhong, K. Bosnick, J. Park, and P. L. McEuen, "Extremely efficient multiple electron-hole pair generation in carbon nanotube photodiodes," Science **325**, 1367–1371 (2009).

[85] G. Buchs, M. Barkelid, S. Bagiante, G. A. Steele, and V. Zwiller, "Imaging the formation of a p-n junction in a suspended carbon nanotube with scanning photocurrent microscopy," J. Appl. Phys. **110**, 074308 (2011).

[86] M. Barkelid and V. Zwiller, "Single carbon nanotube photovoltaic device," J. Appl. Phys. **114**, 164320 (2013).

[87] M. Freitag, J. C. Tsang, A. Bol, and P. Avouris, "Scanning photovoltage microscopy of potential modulations in carbon nanotubes," Appl. Phys. Lett. **91**, 031101 (2007).

[88] M. Freitag, J. C. Tsang, A. Bol, D. Yuan, J. Liu, and P. Avouris, "Imaging of the Schottky barriers and charge depletion in nanotube transistors," Nano Letters **7**, 2037–2042 (2007).

[89] E. J. H. Lee, K. Balasubramanian, J. Dorfmüller, R. Vogelgesang, N. Fu, A. Mews, M. Burghard, and K. Kern, "Electronic band structure mapping of nanotube transistors by scanning photocurrent microscopy," Small **3**, 2038–2042 (2007).

[90] Y. H. Ahn, A. W. Tsen, B. Kim, Y. W. Park, and J. Park, "Photocurrent imaging of p-n junctions in ambipolar carbon nanotube transistors," Nano Lett. **7**, 3320–3323 (2007).

[91] E. J. H. Lee, K. Balasubramanian, M. Burghard, and K. Kern, "Spatially resolved potential distribution in carbon nanotube cross-junction devices," Adv. Mater. **21**, 2720–2724 (2009).

[92] Y. Ahn, J. Dunning, and J. Park, "Scanning photocurrent imaging and electronic band studies in silicon nanowire field effect transistors," Nano Lett. **5**, 1367–1370 (2005).

[93] Y. Gu, J. P. Romankiewicz, J. K. David, J. L. Lensch, L. J. Lauhona, E.-S. Kwak, and T. W. Odom, "Local photocurrent mapping as a probe of contact effects and charge carrier transport in semiconductor nanowire devices," J. Vac. Sci. Technol. B **24**, 1071–1023 (2006).

[94] T. Müller, V. Xia, M. Freitag, J. Tsang, and P. Avouris, "Role of contacts in graphene transistors: a scanning photocurrent study," Phys. Rev. B **79**, 245430 (2009).

[95] Y. Liu, S. Lu, and B. Panchapakesan, "Alignment enhanced photoconductivity in single wall carbon nanotube films," Nanotechnology **20**, 035203 (2009).

[96] M. Engel, M. Steiner, R. S. Sundaram, R. Krupke, A. A. Green, M. C. Hersam, and P. Avouris, "Spatially resolved electrostatic potential and photocurrent generation in carbon nanotube array devices," ACS Nano **6**, 7303–7310 (2012).

[97] J. U. Lee, P. J. Codella, and M. Pietrzykowski, "Direct probe of excitonic and continuum transitions in the photocurrent spectroscopy of individual carbon nanotube p-n diodes," Appl. Phys. Lett. **90**, 053103 (2007).

[98] V. Perebeinos and P. Avouris, "Exciton Ionization, Franz-Keldysh, and Stark effects in carbon nanotubes," Nano Letters **7**, 609–613 (2007). PMID: 17261074.

[99] Y. Kumamoto, M. Yoshida, A. Ishii, A. Yokoyama, T. Shimada, and Y. K. Kato, "Spontaneous exciton dissociation in carbon nanotubes," Phys. Rev. Lett. **112**, 117401 (2014).

[100] S. Konabe, T. Yamamoto, and K. Watanabe, "Auger-recombination induced photocurrents in single-walled carbon nanotubes," Appl. Phys. Expr. **2**, 092202 (2009).

[101] B. C. St-Antoine, D. Ménard, and R. Martel, "Position sensitive photothermoelectric effect in suspended single-walled carbon nanotube films," Nano Letters **9**, 3503–3508 (2009).

[102] T. DeBorde, L. Aspitarte, T. Sharf, J. W. Kevek, and E. D. Minot, "Photothermoelectric effect in suspended semiconducting carbon nanotubes," ACS Nano **8**, 216–221 (2014).

[103] X. Xu, N. M. Gabor, J. S. Alden, A. M. van der Zande, and P. L. McEuen, "Photothermoelectric effect at a graphene interface junction," Nano Letters **10**, 562–566 (2010). PMID: 20038087.

[104] N. M. Gabor, J. C. W. Song, Q. Ma, N. L. Nair, T. Taychatanapat, K. Watanabe, T. Taniguchi, L. S. Levitov, and P. Jarillo-Herrero, "Hot carrier-assisted intrinsic photoresponse in graphene," Science **334**, 648–652 (2011).

[105] J. C. W. Song, M. S. Rudner, C. M. Marcus, and L. S. Levitov, "Hot carrier transport and photocurrent response in graphene," Nano Letters **11**, 4688–4692 (2011).

[106] D. Sun, G. Aivazian, A. M. Jones, J. S. Ross, W. Yao, D. Cobden, and X. Xu, "Ultrafast hot-carrier-dominated photocurrent in graphene," Nat. Nanotechnol. **7**, 114–118 (2012).

[107] M. Freitag, T. Low, F. Xia, and P. Avouris, "Photoconductivity of biased graphene," Nat. Photon. **7**, 53–59 (2013).

[108] J. A. Misewich, R. Martel, P. Avouris, J. C. Tsang, S. Heinze, and J. Tersoff, "Electrically induced optical emission from a carbon nanotube FET," Science **300**, 783–786 (2003).

[109] M. Freitag, V. Perebeinos, J. Chen, A. Stein, J. C. Tsang, J. A. Misewich, R. Martel, and P. Avouris, "Hot carrier electroluminescence from a single carbon nanotube," Nano Letters **4**, 1063–1066 (2004).

[110] M. Freitag, J. Chen, J. Tersoff, J. C. Tsang, Q. Fu, J. Liu, and P. Avouris, "Mobile ambipolar domain in carbon-nanotube infrared emitters," Phys. Rev. Lett.. **93**, 076803 (2004).

[111] T. Müller, M. Kinoshita, M. Steiner, V. Perebeinos, A. A. Bol, D. B. Farmer, and P. Avouris, "Efficient narrow-band light emission from a single carbon nanotube p-n diode," Nat. Nanotechnol. **5**, 27–31 (2009).

[112] S. Wang, Q. Zeng, L. Yang, Z. Zhang, Z. Wang, T. Pei, L. Ding, X. Liang, M. Gao, Y. Li, and L.-M. Peng, "High-performance carbon nanotube light-emitting diodes with asymmetric contacts," Nano Letters **11**, 23–29 (2011).

[113] V. Perebeinos and P. Avouris, "Impact excitation by hot carriers in carbon nanotubes," Phys. Rev. B **74**, 121410(R) (2006).

[114] M. Freitag, J. C. Tsang, J. Kirtley, A. Carlsen, J. Chen, A. Troeman, H. Hilgenkamp, and P. Avouris, "Electrically excited, localized infrared emission from single carbon nanotubes," Nano Letters **6**, 1425–1433 (2006).

[115] M. Pfeiffer, N. Stürzl, C. W. Marquardt, M. Engel, S. Dehm, F. Hennrich, M. M. Kappes, U. Lemmer, and R. Krupke, "Electroluminescence from chirality-sorted (9,7)-semiconducting carbon nanotube devices," Opt. Express **19**, A1184–A1189 (2011).

[116] D. Mann, Y. K. Kato, A. Kinkhabwala, E. Pop, J. Cao, X. Wang, L. Zhang, Q. Wang, J. Guo, and H. Dai, "Electrically driven thermal light emission from individual single-walled carbon nanotubes," Nat. Nanotechnol. **2**, 33–38 (2007).

[117] X. Wang, L. Zhang, Y. Lu, H. Dai, Y. K. Kato, and E. Pop, "Electrically driven light emission from hot single-walled carbon nanotubes at various temperatures and ambient pressures," Appl. Phys. Lett. **91**, 261102 (2007).

[118] Z. Liu, A. Bushmaker, M. Aykol, and S. B. Cronin, "Thermal emission spectra from individual suspended carbon nanotubes," ACS Nano **5**, 4634–4640 (2011).

[119] S. Essig, C. W. Marquardt, A. Vijayaraghavan, M. Ganzhorn, S. Dehm, F. Hennrich, F. Ou, A. A. Green, C. Sciascia, F. Bonaccorso, K.-P. Bohnen, H. v. Löhneysen, M. M. Kappes, P. M. Ajayan, M. C. Hersam, A. C. Ferrari, and R. Krupke, "Phonon-assisted electroluminescence from metallic carbon nanotubes and graphene," Nano Letters **10**, 1589–1594 (2010).

[120] N. Mauser and A. Hartschuh, "Tip-enhanced near-field optical microscopy," Chem. Soc. Rev. **43**, 1248–1262 (2014).

[121] W. Heisenberg, "Über den anschaulichen inhalt der quantentheoretischen kinematik und mechanik." Zeitschrift für Physik **43**, 172–198 (1927).

[122] Novotny, L. and Hecht, B., *Principles of nano-optics* (Cambridge University Press, Cambridge, 2006).

[123] T. H. Taminiau, F. D. Stefani, and N. F. van Hulst, "Single emitters coupled to plasmonic nano-antennas: angular emission and collection efficiency," New J. Phys. **10**, 105005 (2008).

[124] P. Bharadwaj, B. Deutsch, and L. Novotny, "Optical antennas," Adv. Opt. Photon. **1**, 438–483 (2009).

[125] L. Novotny and N. van Hulst, "Antennas for light," Nat. Photon. **5**, 83–90 (2011).

[126] M. S. Hofmann, J. T. Glückert, J. Noé, C. Bourjau, R. Dehmel, and A. Högele, "Bright, long-lived and coherent excitons in carbon nanotube quantum dots," Nat. Nanotechnol. **8**, 502–505 (2013).

[127] N. Naredi-Rainer, J. Prescher, A. Hartschuh, and D. C. Lamb, *Fluorescence microscopy: from principles to biological applications* (Wiley-VCH, 2013), chap. Confocal Microscopy.

[128] F. Xia, T. Mueller, R. Golizadeh-Mojarad, M. Freitag, Y. Lin, J. Tsang, V. Perebeinos, and P. Avouris, "Photocurrent imaging and efficient photon detection in a graphene transistor," Nano Letters **9**, 1039–1044 (2009).

[129] Y. Gu, E. S. Kwak, J. L. Lensch, J. E. Allen, T. W. Odom, and L. J. Lauhon, "Near-field scanning photocurrent microscopy of a nanowire photodetector," Appl. Phys. Lett. **87**, 043111 (2005).

[130] F. Schöppler, C. Mann, T. C. Hain, F. M. Neubauer, G. Privitera, F. Bonaccorso, D. Chu, A. C. Ferrari, and T. Hertel, "Molar extinction coefficient of single-wall carbon nanotubes," J. Phys. Chem. C. **115**, 14682–14686 (2011).

[131] M. Kinoshita, M. Steiner, M. Engel, J. P. Small, A. A. Green, M. C. Hersam, R. Krupke, E. E. Mendez, and P. Avouris, "The polarized carbon nanotube thin film LED," Opt. Express **28**, 25738–25745 (2010).

[132] X. Xie, A. E. Islam, M. A. Wahab, L. Ye, X. Ho, M. A. Alam, and J. A. Rogers, "Electroluminescence in aligned arrays of single-wall carbon nanotubes with asymmetric contacts," ACS Nano **6**, 7981–7988 (2012).

[133] T. Mori, Y. Yamauchi, S. Honda, and H. Maki, "An electrically driven, ultrahigh-speed, on-chip light emitter based on carbon nanotubes," Nano Lett. **14**, 3277–3283 (2014).

[134] C. Liu, V. Kamaev, and Z. V. Vardenya, "Efficiency enhancement of an organic light-emitting diode with a cathode forming two-dimensional periodic hole array," Appl. Phys. Lett. **86**, 143501 (2005).

[135] S. Pillai, K. R. Catchpole, T. Trupke, G. Zhang, J. Zhao, and M. A. Green, "Enhanced emission from Si-based light emitting diodes using surface plasmons," Appl. Phys. Lett. **88**, 161102 (2006).

[136] J. Sun, J. Khurgin, and R. Soref, "Plasmonic light-emission enhancement with isolated metal nanoparticles and their coupled arrays," J. Opt. Soc. Am. B **25**, 1748–1755 (2008).

[137] M. Freitag, M. Steiner, A. Naumov, J. P. Small, A. A. Bol, V. Perebeinos, and P. Avouris, "Carbon nanotube photo- and electroluminescence in longitudinal electric fields," ACS Nano **3**, 3744–3748 (2009).

[138] M. S. Fuhrer, J. Nygard, L. Shih, M. Forero, Y.-G. Yoon, M. S. C. Mazzoni, H. J. Choi, J. Ihm, S. G. Louie, A. Zettl, and P. L. McEuen, "Crossed nanotube junctions," Science **288**, 494–497 (2000).

[139] N. Mauser and A. Hartschuh, "Tip-enhanced near-field optical microscopy," Chem. Soc. Rev. **43**, 1248–1262 (2014).

[140] N. Anderson, P. Anger, A. Hartschuh, and L. Novotny, "Subsurface Raman imaging with nanoscale resolution," Nano Lett. **6**, 744 (2006).

[141] D. Zhang, U. Heinemeyer, C. Stanciu, M. Sackrow, K. Braun, L. E. Hennemann, X. Wang, R. Scholz, F. Schreiber, and A. J. Meixner, "Nanoscale Spectroscopic Imaging of Organic Semiconductor Films by Plasmon-Polariton Coupling," Phys. Rev. Lett. **104**, 056601 (2010).

[142] N. Rauhut, M. Engel, M. Steiner, R. Krupke, P. Avouris, and A. Hartschuh, "Antenna-enhanced photocurrent microscopy on single-walled carbon nanotubes at 30 nm resolution," ACS Nano **6**, 6416–6421 (2012).

[143] E. J. Sánchez, L. Novotny, and X. S. Xie, "Near-field fluorescence microscopy based on two-photon excitation with metal tips," Phys. Rev. Lett. **82**, 4014–4017 (1999).

[144] R. Zhang, Y. Zhang, Z. C. Dong, S. Jiang, C. Zhang, L. G. Chen, L. Zhang, Y. Liao, J. Aizpurua, Y. Luo, J. L. Yang, and J. G. Hou, "Chemical mapping of a single molecule by plasmon-enhanced Raman scattering," Nature **498**, 82–86 (2013).

[145] C. Georgi, M. Böhmler, H. Qian, L. Novotny, and A. Hartschuh, "Probing exciton propagation and quenching in carbon nanotubes with near-field optical microscopy," Phys. Stat. Sol. B **246**, 2683 (2009).

[146] R. Kumar, M. Nyk, T. Y. Ohulchanskyy, C. A. Flask, and P. N. Prasad, "Combined optical and MR bioimaging using rare earth ion doped $NaYF_4$ nanocrystals," Adv. Funct. Mater. **19**, 853–859 (2009).

[147] Q. Liu, Y. Sun, C. Li, J. Zhou, C. Li, T. Yang, X. Zhang, T. Yi, D. Wu, and F. Li, "18f-labeled magnetic-upconversion nanophosphors via rare-earth cation-assisted ligand assembly," ACS Nano **5**, 3146–3157 (2011).

[148] W. G. v. Sark, J. d. Wild, J. K. Rath, A. Meijerink, and R. E. Schropp, "Upconversion in solar cells," Nanoscale Res. Lett. **8**, 1–10 (2013).

[149] L. R. P. Kassab, C. B. de Araújo, R. Kobayashi, R. de Almeida Pinto, and D. M. da Silva, "Influence of silver nanoparticles in the luminescence efficiency of Pr^{3+}-doped tellurite glasses," J. Appl. Phys. **102**, 103515 (2007).

[150] L. R. P. Kassab, S. D. da Silva, R. de Almeida Pinto, and C. B. de Araújo, "Photoluminescence enhancement by gold nanoparticles in Eu^{3+} doped GeO_2-Bi_2O_3 glasses," Appl. Phys. Lett. **94**, 101912 (2009).

[151] V. Rai, L. Menezes, C. de Araújo, L. Kassab, D. da Silva, and R. Kobayashi, "Surface-plasmon-enhanced frequency upconversion in Pr^{3+} doped tellurium-oxide glasses containing silver nanoparticles," J. Appl. Phys. **103**, 093526 (2008).

[152] Q. C. Sun, H. Mundoor, J. C. Ribot, V. Singh, I. I. Smalyukh, and P. Nagpal, "Plasmon-enhanced energy transfer for improved upconversion of infrared radiation in doped-lanthanide nanocrystals," Nano Lett. **14**, 101–106 (2014).

[153] D. Lu, S. K. Cho, S. Ahn, L. Brun, C. J. Summers, and W. Park, "Plasmon enhancement mechanism for the upconversion processes in $nayf_4$:yb^{3+}, er^{3+} nanoparticles: Maxwell *versus* förster," ACS Nano (2014).

[154] S. Schietinger, T. Aichele, H.-Q. Wang, T. Nann, and O. Benson, "Plasmon-enhanced upconversion in single $NaYF_4$:Yb^{3+}/Er^{3+} codoped nanocrystals," Nano Lett. **10**, 134–138 (2010).

[155] M. Nyk, R. Kumar, T. Y. Ohulchanskyy, E. J. Bergey, and P. N. Prasad, "High contrast in vitro and in vivo photoluminescence bioimaging using near infrared to near infrared up-conversion in Tm^{3+} and Yb^{3+} doped fluoride nanophosphors," Nano Lett. **8**, 3834–3838 (2008).

[156] N. Hartmann, D. Piatkowski, R. Ciesielski, S. Mackowski, and A. Hartschuh, "Radiation channels close to a plasmonic nanowire visualized by back focal plane imaging," ACS Nano **7**, 10257–10262 (2013).

[157] L. Novotny, E. J. Sánchez, and X. S. Xie, "Near-field optical imaging using metal tips by higher-order hermite-gaussian beams," Ultramicroscopy **71**, 21 (1998).

[158] R. Esteban, M. Laroche, and J. J. Greffet, "Influence of metallic nanoparticles on upconversion processes," J. Appl. Phys. **105**, 033107 (2009).

[159] C. Strohhöfer and A. Polman, "Relationship between gain and Yb^{3+} concentration in Er^{3+}- Yb^{3+} doped waveguide amplifiers," J. Appl. Phys. **90**, 4314–4320 (2001).

[160] D. Piatkowski and S. Mackowski, "Excited state absorption in glasses activated with rare earth ions: Experiment and modeling," Optical Mat. **34**, 2055–2060 (2012).

[161] C. Blum, N. Zijlstra, A. Lagendijk, M. Wubs, A. P. Mosk, V. Subramaniam, and W. L. Vos, "Nanophotonic control of the Förster resonance energy transfer efficiency," Phys. Rev. Lett. **109**, 203601 (2012).

[162] "We estimated the quantum efficiency η_{20} of the green emission dividing the experimentally measured life time $\tau_{exp} = 36\,\mu s$ by a theoretical value of $\tau_{calc} = 550\,\mu s$ calculated by the judd-ofelt theory considering only radiative decay. η_{10} is estimated in the same way using a value for the experimental life time of $\tau_{exp} = 3000\,\mu s$ for the ${}^4i_{11/2}$ state taken from [171] and $\tau_{calc} = 9000\,\mu s$." .

[163] F. Auzel, "Upconversion and anti-Stokes processes with f and d ions in solids," Chem. Rev. **104**, 139–173 (2004).

[164] J. M. Ward, D. G. O'Shea, B. J. Shortt, and S. N. Chormaic, "Optical bistability in Er-Yb codoped phosphate glass microspheres at room temperature," J. Appl. Phys. **102**, 023104 (2007).

[165] Y. Yan, A. J. Faber, and H. de Waal, "Luminescence quenching by OH groups in highly Er-doped phosphate glasses," J. of Non-Cryst. Solids **181**, 283–290 (1995).

[166] A. Miguel, M. Al-Saleh, J. Azkargorta, R. Morea, J. Gonzalo, M. A. Arriandiaga, J. Fernandez, and R. Balda, "Spectroscopic properties of Er^{3+}-doped fluorotellurite glasses," Opt. Mater. **35**, 2039–2044 (2013).

[167] N. Jaba, H. BenMansour, A. Kanoun, A. Brenier, and B. Champagnon, "Spectral broadening and luminescence quenching of 1.53 µm emission in Er^{3+}-doped zinc tellurite glass," J. Lumin. **129**, 270–276 (2009).

[168] M. S. Anderson and S. D. Gaimari, "Raman-atomic force microscopy of the ommatidial surfaces of dipteran compound eyes," J. Struct. Biol. **142**, 364–368 (2003).

[169] Z. Wang, F. Tao, L. Yao, W. Cai, and X. Li, "Selected synthesis of cubic and hexagonal $NaYF_4$ crystals via a complex-assisted hydrothermal route," J. Cryst. Growth **290**, 296–300 (2006).

[170] J. Suyver, J. Grimm, M. van Veen, D. Biner, K. Krämer, and H. Güdel, "Upconversion spectroscopy and properties of $nayf_4$ doped with er^{3+}, tm^{3+} and/or yb^{3+}," J. Lumin. **117**, 1–12 (2006).

[171] M. Pokhrel, G. A. Kumar, and D. K. Sardar, "Highly efficient NIR to NIR and VIS upconversion in Er^{3+} and Yb^{3+} doped in M_2O_2S (M =Gd, La, Y)," J. Mater. Chem. A **1**, 11595 (2013).

List of Abbreviations

0D	...	zero-dimensional
1D	...	one-dimensional
3D	...	three-dimensional
AFM	...	atomic force microscopy
APD	...	avalanche photodiode
CCD	...	charge coupled device
CNT	...	carbon nanotube
CNTFET	...	carbon nanotube based field-effect transistor
CVD	...	chemical vapor deposition
DOS	...	density of states
EBL	...	electron beam lithography
EL	...	electroluminescence
FET	...	field-effect transistor
FWHM	...	full width at half maximum
IFM	...	intermediate frequency mode
JFET	...	junction field-effect transistor
KPFM	...	Kelvin probe force microscopy
LED	...	light-emitting device
MIBK	...	methyl isobutyl ketone
MIGS	...	metal-induced gap states
MOSFET	...	metall-oxide semiconductor field-effect transistor
PALM	...	photoactivated localization microscopy
PLL	...	phase-locked loop
PMMA	...	polymethylmethacrylate
PSF	...	point-spread function
RBM	...	radial breathing mode
RRS	...	resonance raman scattering
SEM	...	scanning electron microscope
SGM	...	scanning gate microscopy
SNOM	...	scanning near-field optical microscopy
SPCM	...	scanning photocurrent microscopy
SPM	...	surface probe microscopy
STED	...	stimulated emission depletion microscopy
STM	...	scanning tunneling microscopy

STORM	...	stochastic optical reconstruction microscopy
SWCNT	...	single-walled carbon nanotube
TENOM	...	tip-enhanced near-field optical microscopy
TERS	...	tip-enhanced Raman scattering
vHS	...	van Hove singularity

List of Figures

List of Publications

Publications in the course of this work

N. Rauhut, M. Engel, M. Steiner, R. Krupke, Ph. Avouris, A. Hartschuh, "Antenna-enhanced Photocurrent Microscopy on Single-Walled Carbon Nanotubes", *ACS Nano*, **6**, 6416-6421 (2012)

N. Mauser, A. Hartschuh, "Tip-enhanced Near-field Optical Microscopy", *Chem. Soc. Rev.*, **43**, 1248-1262 (2014)

N. Mauser, N. Hartmann, M. S. Hofmann, J. Janik, A. Högele, A. Hartschuh, "Antenna-enhanced Optoelectronic Probing of Carbon Nanotubes", *Nano Letters*, **14**, 3773-3778 (2014)

N. Mauser, A. Hartschuh, "TERS - Applications to Carbon Nanomaterials", book chapter in *Handbook of Enhanced Spectroscopy*, Pan Stanford Publishing, *submitted* (2014)

N. Mauser, D. Piatkowski, T. Mancabelli, M. Nyk, S. Mackowski, A. Hartschuh, "Tip-enhancement of upconversion photoluminescence in rare-earth ion doped crystals", *submitted* (2014)

Other publications

H. L. Xu, M. Nilsson, S. Ohser, N. Rauhut, S. Kröll, M. Aguiló, F. Díaz, "Hyperfine structure and homogeneous broadening in Pr^{3+}:$KY(WO_4)_2$", *Phys. Rev. B*, **70**, 214115 (2004)

K. Ladouceur, B. G. Klappauf, J. van Dongen, N. Rauhut, B. Schuster, A. K. Mills, D. J. Jones, K. W. Madison. "Compact laser cooling apparatus for simultaneous cooling of lithium and rubidium", *JOSA B*, **26**, 210-217 (2009)

List of Conferences

Tip Enhanced Raman Spectroscopy (TERS II)
Teddington (UK), July 5-6, 2011
Poster presentation: *"Near-Field Optical Investigations of single-walled Carbon Nanotubes"*

Advanced DPG Physics School: Nanoantennas and Hybrid Quantum Systems
Bad Honnef (Germany), September 25 - 30, 2011
Poster presentation: *"Near-Field Optical Investigations of single-walled Carbon Nanotubes"*

Workshop on Nano Carbon Optics
Herrsching (Germany), October 6 - 9, 2011
Poster presentation: *"Scanning Photocurrent Microscopy on single-walled Carbon Nanotubes"*

DPG Frühjahrstagung 2012
Berlin (Germany), March, 25 - 30, 2012
Oral presentation: *"Antenna-enhanced Photocurrent Microscopy on Single-Walled Carbon Nanotubes"*

Materials Research Society (MRS) Spring Meeting 2012
San Francisco (USA), April 9-13, 2012
Oral presentation: *"Tip-enhanced Photocurrent Microscopy of Single-Walled Carbon Nanotubes"*

International Conference on Hole Burning, Single Molecule and Related Spectroscopies (HSBM) 2012
Tübingen (Germany), August 27-30, 2012
Oral presentation: *"Antenna-enhanced Photocurrent Microscopy on Single-Walled Carbon Nanotubes"*

Materials Science & Technology (MS&T) 2013
Montreal (Canada), October 27-31, 2013
Oral presentation: *"Antenna-enhanced Optoelectronics of Carbon Nanotubes"*

Materials Research Society (MRS) Fall Meeting 2013
Boston (USA), December 1-6, 2013
Oral presentation: *"Antenna-enhanced Optoelectronics of Carbon Nanotubes"*

Science Rocks!
Munich (Germany), January 9, 2014
Oral presentation: *"Deceiving Diffraction - A Door to the Nanoworld"*

Acknowledgments

First of all, I want to thank my doctoral advisor **Prof. Dr. Achim Hartschuh** for giving me the opportunity to work on this project. He always was ready to help and support me with his theoretical and experimental expertise.

I also want to thank **Prof. Dr. Ralph Krupke** for his coorporation and the support as my second reviewer.

A very warm thanks goes to the former group members **Miriam Böhmler** and **Carsten Georgi** for introducing me to the near-field setup during the first months and for their friendship during the following years.

I am very grateful to **Philipp Altpeter** for the great support in the clean room and **Steffen Schmidt** for the time he spent with me at the SEM, investigating hundreds of gold tips.

Thanks to **Dawid Piatkowski**, for the joint project on the rare-earth ion doped crystals and **Michael Engel** for introducing me to the electrical measurements.

Thanks to my Bachelor students **Nitin Saxena** and **Tobias Hermann** for the support regarding the sample preparation techniques.

I am very grateful to **Prof. Dr. Alexander Högele**, **Matthias Hofmann** and **Jonathan Noé** for the coorporation and for providing me with the CVD grown carbon nanotubes. Without them the EL measurements would not have been possible.

I want to thank all former and current group members **Rita, Tobias, Giovanni, Harald, Richard, Amit, Sabrina, Tobia, Alberto, Xian, Nicolas, Kathrin,** and **Irene** for the great atmosphere and the fun that we had. Especially, I want to thank **Julia Janik**, **Matthias Handloser** and **Nicolai Hartmann** for their friendship, and **Kevin Donkers** for his advices concerning the English language.

Finally, I want to thank my whole family, especially my parents **Ulrich** and **Helga**. Thank you so much, for always supporting and helping me during the years of my studies. Without your trust, your understanding and your babysitting activities things would have been much more difficult.

Thank you **Hanna**, for bringing so much joy to my life.

Most of all, I am deeply grateful to my husband **Christian** for his never-ending support and understanding.